Cell

ErbB family receptor dimerization dynamics and dysregulation via long-term single-molecule imaging

Graphical abstract

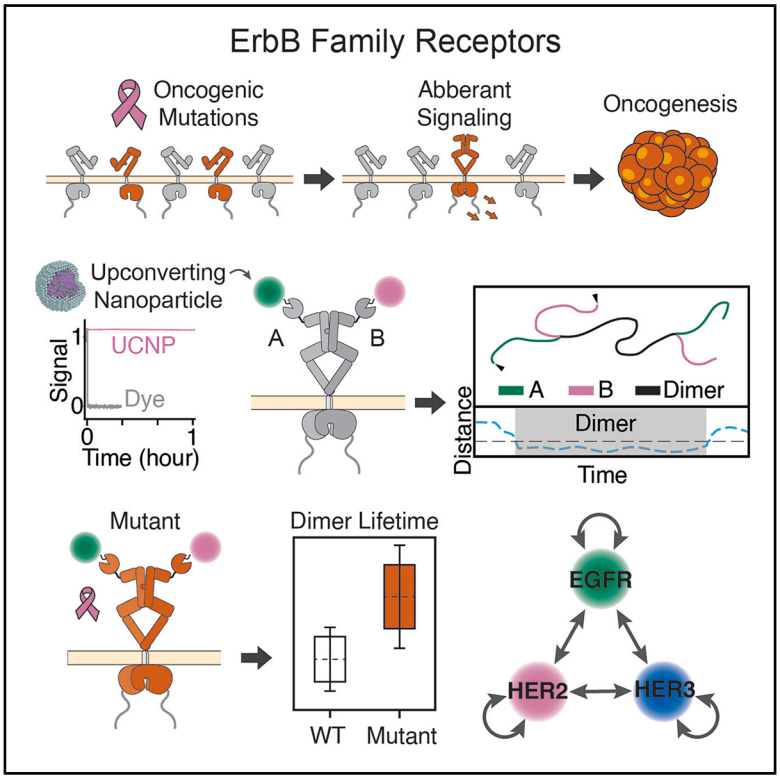

Highlights

- Multicolor UCNPs enable specific ErbB labeling for long-term tracking (UCNP-SPT)
- Bayesian diffusion analysis and dimer lifetimes quantify ErbB receptor mutant dynamics
- UCNP-SPT shows HER2/HER3 homodimerization and how mutations affect dimer stability
- UCNP-SPT reveals EGFR/HER2/HER3 heterodimers and ligand effects on dimer stability

Authors

Kaibo Ma, Xiaojie Ma, João F. Shida, ..., Heidi Greulich, Matthew Meyerson, Chunte Sam Peng

Correspondence

sampeng@mit.edu

In brief

Ma et al. developed long-term single-particle tracking of ErbB family receptors in living cells using upconverting nanoparticles. They discovered constitutive HER2 and HER3 homodimerization and showed how oncogenic mutations and ligand stimulation affect dimerization dynamics, offering new insights into the mechanisms of oncogenic signaling and the ErbB receptor interaction network.

Ma et al., 2026, Cell *189*, 3413–3431
May 28, 2026
https://doi.org/10.1016/j.cell.2026.04.010

CellPress

Cell

CellPress
OPEN ACCESS

Article

ErbB family receptor dimerization dynamics and dysregulation via long-term single-molecule imaging

Kaibo Ma,[1,2,3,10] Xiaojie Ma,[1,2,10] João F. Shida,[1,2,10] Zijian Niu,[1,4] Yuzhu Karlie Lin,[1,2] Saptarshi Mandal,[1,2] Alexandra Dobbins,[5] Lior Golomb,[5] Michael J. Eck,[6,7] Heidi Greulich,[5,8] Matthew Meyerson,[5,8,9] and Chunte Sam Peng[1,2,11,*]

[1]Broad Institute of MIT and Harvard, Cambridge, MA, USA
[2]Department of Chemistry, Massachusetts Institute of Technology, Cambridge, MA, USA
[3]Department of Chemistry and Chemical Biology, Harvard University, Cambridge, MA, USA
[4]Computational and Systems Biology Program, Massachusetts Institute of Technology, Cambridge, MA, USA
[5]Department of Medical Oncology, Dana-Farber Cancer Institute, Boston, MA, USA
[6]Department of Cancer Biology, Dana-Farber Cancer Institute, Boston, MA, USA
[7]Department of Biological Chemistry and Molecular Pharmacology, Harvard Medical School, Boston, MA, USA
[8]Cancer Program, Broad Institute of Harvard and MIT, Cambridge, MA, USA
[9]Department of Genetics, Harvard Medical School, Boston, MA, USA
[10]These authors contributed equally
[11]Lead contact
*Correspondence: sampeng@mit.edu
https://doi.org/10.1016/j.cell.2026.04.010

SUMMARY

Dimerization is crucial for the activation of ErbB family receptors, yet the real-time dynamics and effects of oncogenic mutations remain unclear. Here, we performed long-term, multicolor single-particle tracking (SPT) of EGFR, HER2, and HER3 in living cells using upconverting nanoparticles (UCNPs), which do not photobleach. Our technique enables continuous observation of receptor interactions, revealing details of their dimerization dynamics. Oncogenic EGFR mutations promote stable, ligand-independent dimerization. Unexpectedly, both HER2 and HER3 exhibit constitutive homodimerization, prompting a revised model for their activation mechanisms. HER2 mutations modestly enhance homodimer stability compared with EGFR mutations, while HER3 mutations destabilize homodimers, suggesting that HER3 homodimerization sequesters HER3 and limits heterodimerization with other receptors. We also identified stable, ligand-independent heterodimers among all three receptors, further stabilized by ligand stimulation. These insights offer a comprehensive ErbB interaction network, elucidating diverse dimerization mechanisms and implications for oncogenic signaling.

INTRODUCTION

The ErbB family of receptors plays a pivotal role in regulating key cellular processes, including proliferation, differentiation, and survival.[1,2] Dysregulation of ErbB signaling is frequently associated with oncogenesis, driving uncontrolled cell growth and cancer progression.[3,4] This receptor family comprises four closely related receptor tyrosine kinases (RTKs): epidermal growth factor receptor (EGFR), HER2 (ErbB2), HER3 (ErbB3), and HER4 (ErbB4).[2,4,5] Among these, EGFR, HER2, and HER3 are more abundantly expressed in human cancer cell lines compared with HER4.[6] Overexpression and mutations of EGFR, HER2, and HER3 have been discovered and investigated in human cancers, notably in lung cancer, breast cancer, and glioma.[7–15] Despite their significance, our understanding of the real-time dynamics of ErbB receptor interactions and functional consequences of oncogenic mutations in living cells remains incomplete.

Dimerization is an essential step in the activation of ErbB receptors. In the absence of ligand, the extracellular domain (ECD) of EGFR adopts a tethered conformation that inhibits dimerization by blocking its dimerization arm (Figures 1A and 1B). Upon binding to epidermal growth factor (EGF) or other high-affinity ligands, the ECD undergoes a conformational change that relieves this autoinhibition, enabling dimerization.[16–19] The intracellular tyrosine kinase domain (TKD) forms an asymmetric dimer that trans-phosphorylates a series of tyrosine residues in the C-terminal tail, triggering downstream RAS/MAPK and/or PI3K/AKT signaling pathways.[20–25] While much of this understanding is derived from structural studies, the

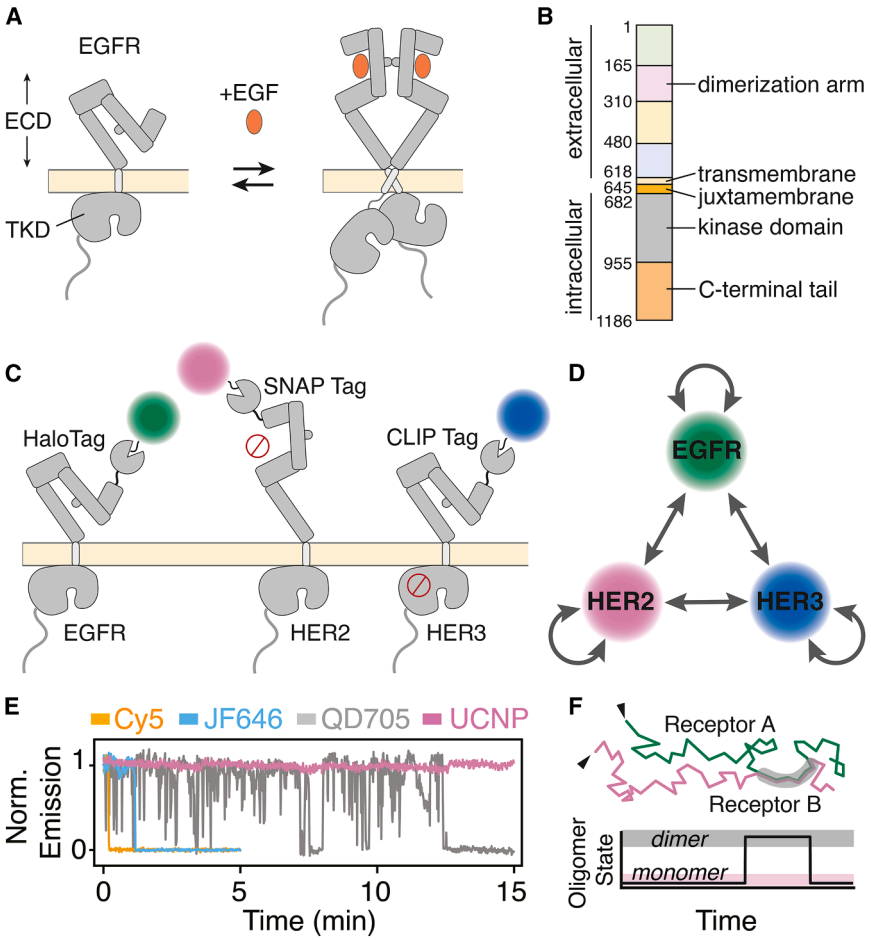

Figure 1. Single-particle tracking of ErbB family of receptors dimerization dynamics

(A) A schematic illustration of EGF-induced conformational changes and dimerization of EGFR.

(B) Domain architecture of EGFR.

(C) Different conformations of unliganded EGFR, HER2, and HER3, and schematic representation of multicolor labeling for tracking receptor dynamics. Red prohibited symbols highlight the lack of HER2 ligand binding and the HER3 catalytic kinase domain.

(D) Homo- and heterodimerization network among EGFR, HER2, and HER3.

(E) Fluorescence time traces of single UCNP (Er10Yb90), Qdot™ 705, JF646 dye, and Cy5 dye.

(F) Illustration of dual-color SPT trajectories of a dimerization event.

See also Figure S1.

real-time dynamics and stability of ErbB receptor dimerization remain less well characterized.

EGFR, HER2, and HER3 share conserved structural motifs: an ECD containing four structural domains (I through IV), with the dimerization arm in domain II, a single-pass transmembrane helix, a short juxtamembrane domain, a TKD, and a C-terminal tail (Figures 1B and 1C).[2] Notably, no ligand has been identified for HER2 so far, which uniquely adopts an extended conformation (Figure 1C).[26] In contrast, the ECD of ligand-free HER3 remains in the tethered form and can bind activating ligands such as neuregulin 1 (NRG1).[27] However, the HER3 TKD is catalytically impaired due to the lack of key residues.[28,29] These distinct structural and functional characteristics suggest divergent activation mechanisms among ErbB receptors, which are still not fully understood. Current consensus holds that HER2 and HER3 primarily function as obligate heterodimerization partners for other ErbB receptors.[30–33] Although homodimerization of HER2 and HER3 has been suggested based on electron microscopy imaging of HER2[34] and *in vitro* oligomerization assays of HER3,[35,36] little is known about the interaction behavior of full-length, membrane-anchored HER2 and HER3 in living cells. Here, we investigate the network and dynamics of the homo- and heterodimerization between these receptors (Figure 1D), which may serve as the molecular basis for initiating downstream signaling and functional outputs.

Single-molecule fluorescence microscopy enables real-time visualization of molecular interactions in living cells, offering insights into molecular heterogeneity and detecting rare, transient events.[37–44] This technique has been utilized to reveal distinct dynamics of full-length EGFR on the live-cell membrane.[45–50] However, early studies using fluorescent proteins or fluorescent dyes such as Cy5 suffered from rapid photobleaching within tens of seconds (Figure 1E), which hinders the ability to observe full EGFR dynamics and dimerization interactions.[48] Methods have been developed to suppress the photobleaching/photoblinking of organic fluorophores, such as using an oxygen scavenger[51] and triplet-state quencher,[52] changing O_2 levels in the imaging buffer,[53] and incorporating deuterium,[54] but inevitably, organic fluorophores still bleach over time. Alternatively, quantum dots can extend imaging beyond 1 min, and experiments using them have revealed important EGFR behaviors: wild-type (WT) EGFR can form transient ligand-independent dimers; EGF stimulation stabilizes EGFR dimerization; and certain EGFR kinase domain mutations can promote long ligand-independent dimerization.[45,46] Nevertheless, quantum dots, such as Qdot705, blink and eventually photobleach (Figure 1E), making single-particle tracking (SPT) challenging and still limiting the observation to short timescales.

Recent developments, including a highly stable dye[55] and exchangeable HaloTag ligands that replenished photobleached dyes, have extended tracking of EGFR dynamics in live cells.[56] Despite these improvements, key challenges remain in reliably measuring true molecular interactions. First, detecting dimerization requires both fluorescent probes on the two receptors to remain photostable, which is unlikely given the stochastic nature

of photobleaching. Secondly, dual-color SPT provides more reliable dimer detection, but this requires photostable probes of different colors. Given that EGFR dimerization can span longer than tens of seconds,[46] an ideal imaging probe must offer photostability lasting several minutes to capture not only the dimerization event itself, but also the pre-association and post-dissociation periods, while preserving molecular identity throughout.

To overcome these limitations, we have developed a class of nanoprobes, rare-earth ion-doped upconverting nanoparticles (UCNPs). UCNPs exhibit exceptional photostability, showing no blinking or photobleaching even over several hours (Figure 1E). UCNPs are doped with sensitizer ytterbium (Yb^{3+}) ions, which absorb near-infrared (NIR) light at 976 nm and transfer the energy to emitter ions such as erbium (Er^{3+}) or thulium (Tm^{3+}) that emit visible light.[57–64] This upconversion process works by converting multiple low-energy photons to a single high-energy photon emitted, resulting in nearly background-free imaging by eliminating autofluorescence. Moreover, the emission color of UCNPs can be tuned by varying the type and concentration of doped rare-earth ions.[57,65] Previously, we used UCNPs to perform long-term tracking of single cargoes in live neurons, revealing the number of active motors and resolving dynein steps.[64] We further engineered 10 nm UCNPs with distinct emission spectra, enabling simultaneous three-color and long-term SPT in live cells.[57]

In this work, we used UCNPs to perform multicolor and long-term single-particle imaging to systematically investigate the homo- and heterodimerization dynamics of EGFR, HER2, and HER3 (Figure 1F), as well as mutant-induced dysregulation. We orthogonally labeled each receptor using multicolor UCNPs and self-labeling protein tags (Figure 1C).[66] The exceptional photostability of UCNPs enabled SPT for more than 15 min, revealing exquisite details of ErbB receptor dynamics in living cells. We provided direct observation of HER2 and HER3 homodimerization at the single-molecule level and revealed ligand-independent homodimerization dynamics of EGFR, HER2, and HER3 driven by oncogenic mutations. We proposed a previously uncharacterized model in which HER3 homodimers represent a non-signaling reservoir that prevents HER3 from heterodimerizing with other ErbB family receptors. Finally, we resolved a complex and heterogeneous network of homo- and heterodimeric interactions among EGFR, HER2, and HER3, offering new insights into the dynamic regulation of ErbB family receptor signaling at the single-molecule level.

RESULTS

Engineering three orthogonal UCNPs for specific targeting of EGFR, HER2, and HER3

To enable single-molecule imaging of EGFR, HER2, and HER3, we first need to engineer three orthogonal UCNPs. We previously optimized three small UCNPs with distinct emission spectra, enabling simultaneous three-color SPT using only one excitation laser at 976 nm.[57] These UCNPs consist of an ~8 nm core containing sensitizer and emitter ions ($NaY_xYb_yRE_zF_4$, where RE stands for Er^{3+} or Tm^{3+}) and a ~1–2 nm optically inactive shell ($NaY_{0.8}Gd_{0.2}F_4$) that suppresses non-radiative energy loss to enhance UCNP brightness. Recently, we identified a brighter NIR-emitting core-shell UCNP consisting of a 10 nm $NaYb_{0.8}Y_{0.1}Tm_{0.1}F_4$ core and a 1.5 nm inert $NaY_{0.8}Gd_{0.2}F_4$ shell (denoted as Tm10Yb80 in this paper). Therefore, for three-color imaging in this work, we selected $NaYb_{0.3}Y_{0.78}Tm_{0.02}F_4$@$NaY_{0.8}Gd_{0.2}F_4$ (Tm02Yb30) as the blue-emitting UCNP, $NaYb_{0.9}Er_{0.1}F_4$@$NaY_{0.8}Gd_{0.2}F_4$ (Er10Yb90) as the red-emitting UCNP, and Tm10Yb80 as the NIR-emitting UCNP. However, in two-color imaging experiments, we used $NaYb_{0.94}Tm_{0.06}F_4$@$NaY_{0.8}Gd_{0.2}F_4$ (Tm06Yb94) as the NIR-emitting UCNP alongside Er10Yb90 because the stronger blue emission from Tm06Yb94 makes it a suboptimal NIR probe in three-color imaging. The single-particle brightness and stability of all the UCNPs under live-cell imaging conditions are shown in Figures S1A and S1B, along with the absorption and emission spectra under 976 nm laser excitation (Figure S1C).

All UCNP cores were shelled with an inert shell to a sub-13 nm size.[67] Transmission electron microscopy (TEM) images (Figure S1D) confirmed the small size and monodispersity in both core and core-shell UCNPs. To enable bio-imaging, we coated as-synthesized UCNPs with poly(maleic anhydride-alt-1-octadecene) (PMAO) and transferred them to aqueous solutions (Figure 2A).[68,69] Subsequently, 1-ethyl-3-(3-dimethylaminopropyl)carbodiimide (EDC) conjugation was performed to PEGylate the surface of PMAO-coated UCNPs. Additionally, we added 1.5% of amine-PEG conjugated to different ligands for specific labeling of target proteins. The representative TEM image of the functionalized UCNPs (Figure 2B) demonstrated that mono-dispersity is preserved after functionalization and purification, with all functionalized UCNPs shown in Figure S1E. The zeta potentials of ligand-conjugated UCNPs were measured in water to be ~14 mV (Figure S1F). The mono-dispersity was also confirmed by dynamic light scattering (DLS) measurements of functionalized UCNPs in 1× PBS (Figure S1G).

To achieve orthogonal labeling of single EGFR, HER2, and HER3 on the membrane of live cells, we used self-labeling protein tags (SLP) HaloTag7,[70] SNAP-tag2,[71] and CLIP-tag2.[72] These SLPs form covalent bonds with their respective ligands (Figure 2A). We refer to the ligands as HTL, STL, and CTL for HaloTag7, SNAP-tag2, and CLIP-tag2, respectively. The protein tags were fused to the N-terminus of receptors with a 13-amino acid flexible linker, and HaloTag7-EGFR (Halo-EGFR), SNAP-tag2-HER2 (SNAP-HER2), and CLIP-tag2-HER3 (CLIP-HER3) were expressed in U2OS cells. Expression of these fusion receptors was shown by staining U2OS cells transfected with Halo-EGFR, SNAP-HER2, and CLIP-HER3, respectively, with their specific fluorescent ligands (Figure 2C). The number of HTL on the UCNPs was quantified by saturating the HTL-UCNPs with purified HaloTag-mOrange and analyzing the stepwise bleaching of the mOrange signal. This near-monovalency indicates that HTL-UCNPs are unlikely to crosslink receptors (Figure S1H–S1J).

To validate the specificity of our UCNPs, we labeled Halo-EGFR with Er10Yb90-HTL, SNAP-HER2 with Tm06Yb94-STL, and CLIP-HER3 with Tm02Yb30-CTL. Single-particle imaging (Figures 2D and S2A–S2E) demonstrated at least a 75:1 specific-to-nonspecific ratio for the labeling of three different SLP-fused receptors and also confirmed the monodispersity and lack of interactions between the three ligand-conjugated

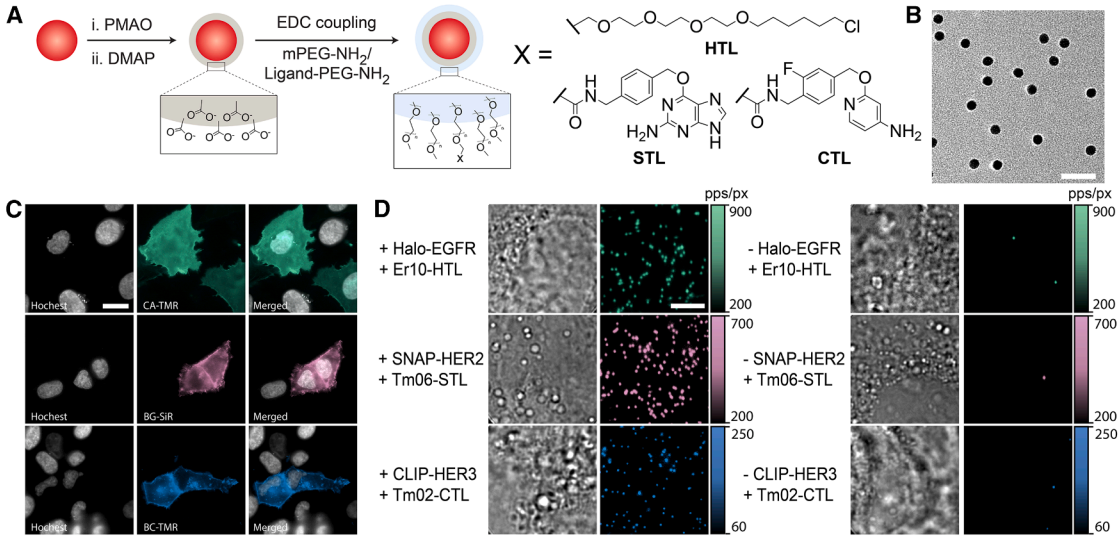

Figure 2. UCNP engineering and cell labeling

(A) A schematic illustration of the surface functionalization of UCNP.

(B) A representative TEM image of UCNPs conjugated to the HaloTag ligand (Tm06Yb94-HTL), showing monodispersed nanoparticles. Scale bars, 50 nm.

(C) U2OS cells expressing SLP-labeled receptors (Halo-EGFR, SNAP-HER2, and CLIP-HER3) were stained with fluorescent dyes conjugated to ligands specific for HaloTag, SNAP tag, and CLIP tag, CA-TMR, BG-SiR647, and BC-TMR, respectively. Images were taken under epifluorescence microscopy. Positive cells represent successful expression of the fusion receptors. Scale bars, 20 μm.

(D) Specific labeling and nonspecific binding of ligand-conjugated UCNPs. Er10, Tm06, and Tm02 are abbreviations for Er10Yb90, Tm06Yb94, and Tm02Yb30, respectively. For each condition, the bright field image of the cell is shown on the left, and the UCNP image is shown on the right. Scale bars, 5 μm.

See also Figures S1, S2, and S3.

UCNPs. These single-particle images were recorded in four separate color channels on a single electron multiplying charge-coupled device (EMCCD) camera using our home-built microscope setup, with total internal reflection illumination and a combination of dichroic mirrors to separate the emission into four different wavelength channels (details are described in STAR Methods). Notably, the CLIP-tag2 and CTL used here were newly developed by the Johnsson lab, which possess enhanced labeling kinetics and specificity.[72] Importantly, we confirmed that the fusion of HaloTag7 at the N-terminus did not perturb the function of the original receptor by testing the gefitinib resistance of engineered PC9 cells expressing Halo-EGFR-L858R/T790M mutation (Figure S3A). T790M is an EGFR secondary mutation that confers resistance to gefitinib and co-occurs with other EGFR primary mutations.[73,74] Figure S3A showed that Halo-EGFR-L858R/T790M expression in PC9 cells induced resistance, whereas parental PC9 cells were sensitive to gefitinib treatment. Additionally, we validated that the UCNP-HTL labeling of Halo-EGFR did not interfere with the EGF-induced downstream signaling of both RAS/MAPK and PI3K/AKT pathways (Figure S3B). And the expression level of Halo-EGFR in U2OS cells that we probed in our tracking experiments remained comparable with a number of EGFR high-expression cancer cell lines (Figure S3C).[6]

Ultralong-term tracking of EGFR revealed distinct diffusional dynamics and dimer behaviors

To investigate EGFR dimerization dynamics in live cells, we performed dual-color long-term SPT by labeling Halo-EGFR in U2OS cells with Er10Yb90-HTL and Tm06Yb94-HTL probes, which can be simultaneously imaged in the red and NIR color channels, respectively. The presence of individual receptors was confirmed by comparing the brightness of point spread functions (PSFs) with the single UCNP brightness (Figure S1B). Leveraging the extreme photostability of UCNPs and their high signal-to-noise ratio, we were able to continuously capture the motion of single and the *same* EGFRs for more than 15 min with 100 ms time resolution, longer than previously reported SPT trajectories, which were shorter than 80 s.[45–50,55] Figure 3A and Video S1 show the trajectory of one EGFR molecule over the entire 16 min and 40 s video (10,000 frames), displaying more complex behavior than a simple one-state Brownian motion on the plasma membrane.

To characterize the heterogeneous motions of EGFRs, we used a hidden Markov model (HMM)-Bayes approach[75] to uncover different diffusion states in the ultralong trajectories (Figures S4A–S4D). Of note, the accuracy of the HMM-Bayes method has been shown to increase with trajectory length.[75] Here, we leverage the unprecedented length of the trajectories obtained through UCNP-SPT to extract a detailed and accurate picture of the dynamics of each receptor. Details on the algorithm, input, output data, and control experiments to verify the accuracy of the method can be found in the STAR Methods section and Figures S4A–S4L. Of the nine different models tested, a model with two diffusion states best described the trajectory shown in Figure 3A. The best-fit model comprised a fast diffusion state with a diffusion coefficient of $D_1 = 0.019\ \mu m^2/s$ and a slow diffusion state with $D_2 = 0.006\ \mu m^2/s$ (Figure S4D). Data S1

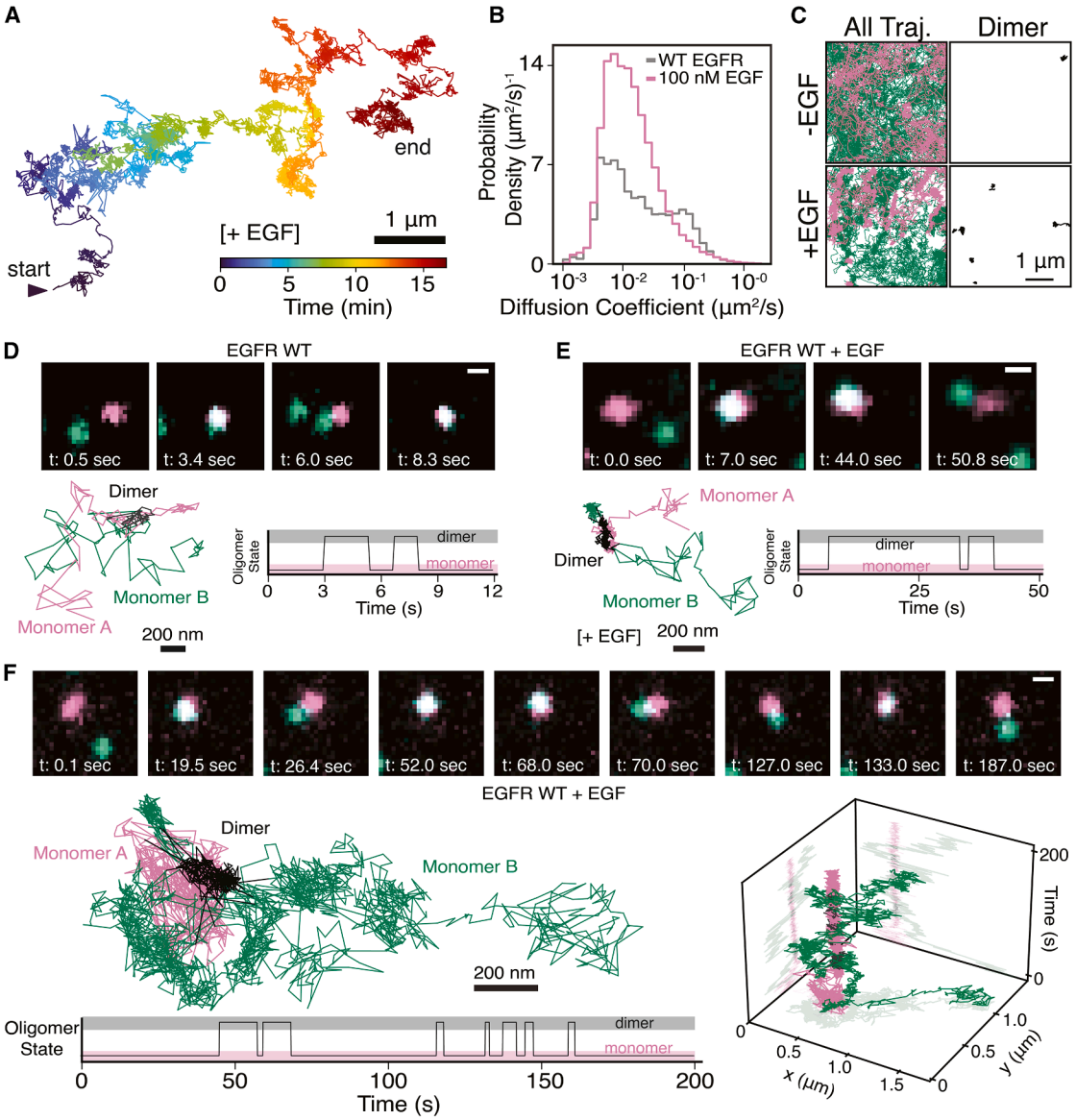

Figure 3. Long-term UCNP tracking of EGFR

(A) 16.7-min continuous tracking of one Halo-EGFR with Er10Yb90-HTL at the bottom membrane of a U2OS cell, incubated with 100 nM EGF. For this specific case, labeling density was adjusted to achieve ~100 labeled receptors per cell within one field of view. Details about this specific cell and trace can be found in Figures S4C and S4D.

(B) Histogram of the diffusion coefficients of EGFR with and without stimulation by 100 nM EGF, obtained through an HMM-Bayes inference algorithm. Unstimulated EGFR exhibits separate slow and fast modes of diffusion, whereas stimulated EGFR exhibits a significant fraction of receptors diffusing in a slow mode. Details about the diffusion coefficient analysis can be found in STAR Methods.

(C) Comparison of the EGFR trajectories measured on the same cell for 3.3 min before and after stimulation with 100 nM EGF (top and bottom, respectively). While the post-EGF video was 16 min long, only a 3.3-min segment, 5 min after the EGF addition, was analyzed for a pair comparison to the pre-EGF video. The left images show all trajectories measured, and the right images highlight only trajectories of dimers above 3 s. Scale bars, 2 µm.

(D) Example dimer trajectory and snapshots of non-stimulated EGFR. The top images show snapshots of the recorded video. Scale bars, 200 nm. The bottom image shows the trajectories of monomers A and B, with the portions of the trajectories in which the two receptors are closer than 125 nm labeled as "dimer." The dimerization state graph is shown on the right. Total dimerization event durations were 2.5 and 1.3 s.

(E) Representative example dimer trajectories and snapshots of EGFR stimulated with 100 nM EGF in the same format as (D). This dimer lifetime is longer than the one shown in (D), persisting for over 20 s. Scale bars, 200 nm.

(F) Example of two EGFR molecules interacting over 3 min. The 3D kymograph is shown on the right. These receptors dimerize very often, and for varying periods of time. The receptor labeled with the NIR particle (magenta receptor) begins by diffusing but soon becomes immobile on the membrane. The receptor labeled by the green particle (green receptor) finds the magenta receptor and begins to diffuse around it. Often, the green receptor becomes immobile together with the magenta receptor, but then diffuses away and returns. A diffusion mode analysis for this trajectory can be found in Figure S5C. Scale bars, 200 nm.

See also Figures S3, S4, and S5.

(page 4) shows the distribution of predicted models for EGFR, with one diffusion mode and two diffusion modes being the most common.

We analyzed trajectories of EGFR with and without 100 nM EGF stimulation using HMM-Bayes and obtained the distribution of the diffusion coefficients from all the diffusion states (Figures 3B and S4J). In both conditions, EGFR diffusion exhibited a broad range from 0.001 to 1 $\mu m^2/s$. For unstimulated EGFRs, the diffusion distribution displays two peaks at around 0.1 and 0.01 $\mu m^2/s$. However, following EGF stimulation, the faster diffusion modes centered around 0.1 $\mu m^2/s$ are shifted toward slower diffusion coefficients. These findings are consistent with previous reports of EGF-induced slowdown of EGFR obtained through mean square displacement (MSD) analysis.[46,76] However, we note that directly applying MSD analysis to long trajectories with mixed motional states may fail to capture the heterogeneity of molecular motions, leading to inaccurate diffusion coefficients. To illustrate this, we simulated 10,000 molecules diffusing with two diffusion modes (Figures S4H and S4I). Applying MSD analysis to these molecules yielded only one diffusion mode, whereas HMM-Bayes accurately and precisely extracted the diffusion coefficients of both diffusional modes. We also verified that the diffusion coefficients obtained from SPT using UCNP-HTL or JF646-HTL dyes are consistent with each other (Figure S4K). By binning receptor localizations, we can obtain a heatmap of permanence for each cell, where we notice local hotspots from confined receptors as well as regions of free diffusion (Figure S4M). Comparing the maps between the EGF-unstimulated and EGF-stimulated conditions, we find more local hotspots in cells stimulated with EGF, reflecting the receptor slowdown seen through diffusion coefficients.

While receptor slowdown upon EGF stimulation may suggest EGFR dimerization and has been used in previous studies to infer EGFR dimerization, we directly visualized dimer formation using dual-color SPT (Figure 3C). EGFR can form ligand-independent dimers with very short lifetimes,[46,77] while EGF stimulation stabilizes these dimers, promoting kinase domain trans-phosphorylation and initiating downstream signaling.[46,78] Since our UCNPs are photostable, we imaged the same U2OS cell before and after 100 nM EGF treatment to directly observe EGF-induced dimerization (Figure 3C). We used a proximity threshold of 125 nm between the two receptors to determine dimerization based on the structure of the EGFR dimer and the UCNP labeling strategy (Figures S4N–S4Q; more details in the STAR Methods section). Co-diffusing trajectories from both Er10-HTL and Tm06-HTL lasting longer than 3 s were plotted in the right panels of Figure 3C. For the cell shown in Figure 3C, one EGFR homodimer was detected before EGF treatment, but several long-lasting dimers emerged post-stimulation, diffusing at various locations on the plasma membrane. Although rare, transient EGFR homodimers were observed in other unstimulated cells (Figure 3D; Data S2, pages 1, 3, and 7); these transient dimers typically lasted for only a few seconds. In contrast, EGF-induced homodimers were significantly more stable (Figures 3E and 3F; Data S2, pages 1, 3, and 8).

The EGFR dimer in Figure 3E persisted for nearly 25 s, with two brief separations at the end (Video S2). The photostability of UCNPs enabled us to clearly visualize both the association and dissociation of these dimers. Moreover, we could observe endocytosis of these receptors, manifested by defocusing and subsequent disappearance of the PSF, as exemplified by the magenta EGFR molecule immediately following dimer dissociation. Furthermore, we can repeatedly measure reversible dimerization events for the same EGFR molecule. In Figure 3F, the EGFR molecules transitioned between monomer and dimer states with prolonged periods of separation. Notably, the magenta trajectory marks an EGFR molecule that remained relatively immobile and confined in a local hotspot, whereas the EGFR molecule marked by the green trajectory diffused around this hotspot, repeatedly interacting with the immobile EGFR for an extended period. These results underscore the advantage and necessity of multicolor UCNP tracking for capturing long-term dimerization dynamics with unprecedented detail. Single-color tracking would have merged both point-spread functions, making it challenging to resolve the distance between molecules. Additionally, short-term tracking would have missed the prolonged and repeated interactions observed in Figure 3F.

While receptor slowdown has been used in previous studies to infer EGFR dimerization,[45] here we test this hypothesis by characterizing dimer behavior. We reconstructed the dimer trajectories by averaging the trajectories of two monomers within a dimer, as validated by our simulations (Figures S4R–S4T), and then applied the HMM analysis. We observed a correlation between dimer formation and receptor slowdown (Figures S5A–S5F). Often, the diffusion coefficients found for the dimer segments were within the slower peak of Figure 3B (<0.01 $\mu m^2/s$). However, behavior before and after dimerization is heterogeneous. In some cases, monomers moved rapidly before dimerization and slowed down when dimerized (Figures S5B, S5E, and S5F). In others, receptors transitioned into fast diffusion after dimer dissociation (Figures S5A and S5B), consistent with the proposed model. In other instances, receptors remained slow both before and after dimerization (Figure S5F). Not all changes between monomer and dimer states corresponded to changes in diffusion coefficient either. These findings indicate that receptor dimerization and oligomerization do not follow a simple model in which diffusion slows proportionally with increasing oligomer size, as previously suggested.[45] Instead, the dynamics of dimerized receptors appear to be strongly influenced by the local membrane microenvironment and interactions with other unlabeled molecules. Therefore, diffusion-based analysis alone is insufficient to fully resolve receptor oligomerization. In contrast, our direct dimer detection using UCNP-SPT provides a more definitive assessment of EGFR dimerization dynamics.

EGFR dimer lifetimes follow a power-law distribution

To quantify the EGFR dimer stability and the impact of EGF stimulation, we plotted histograms of measured dimer lifetimes with and without EGF treatment in Figure 4A. The histogram shows that EGF-activated dimers persist significantly longer than untreated dimers. To differentiate real dimers from random receptor crossings, we simulated Brownian motion of receptors using experimentally measured EGFR diffusion coefficients. As no interactions between receptors were incorporated in the simulation, transient colocalization events occurred by random encounters. The simulation showed that 99.5% of these

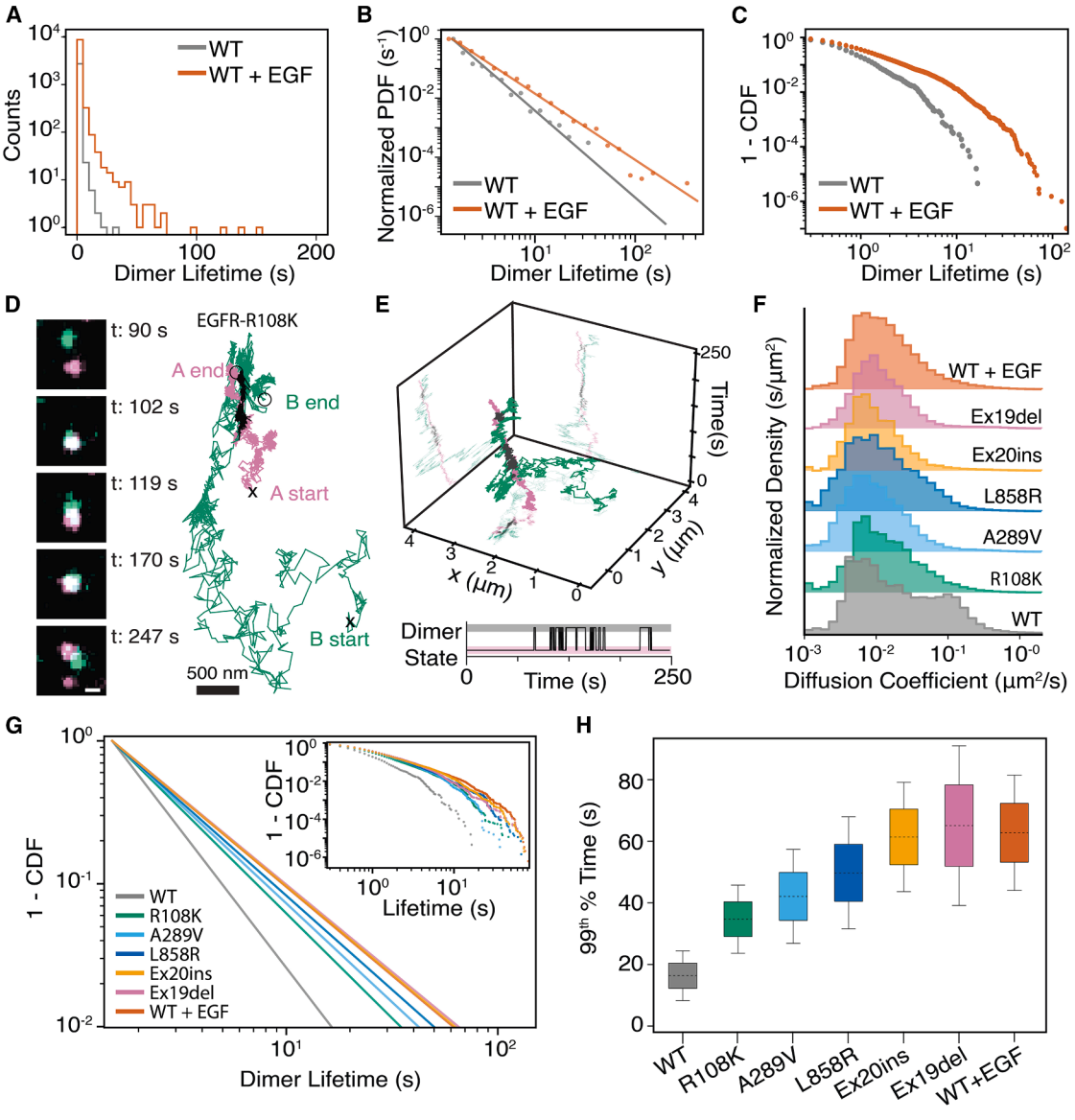

Figure 4. Dimerization lifetime analysis of EGFR, EGF-stimulated EGFR, and EGFR mutants

(A) Histograms of dimer lifetimes measured across multiple cells, before and after stimulation with EGF. We have observed one dimer above 10 min that is not included in this graph.

(B) Normalized probability density function corresponding to the histograms in (A). Each condition was fit to a power law, and both data and fit are shown in the log-log plot. The stimulated EGFR dimers fit a power law with a heavier tail than the unstimulated EGFR dimers.

(C) The $1 - CDF$ curve for both stimulated and unstimulated EGFR, on a log-log scale. The tails of these curves are not straight lines, as power-law $1 - CDF$ curves usually are, because the dataset is finite and reaches zero at the last data point (a detailed explanation can be found in STAR Methods).

(D and E) Dimerization trajectories of a pair of EGFR-R108K receptors. This dimer illustrates an example of the longer dimers found in the mutant conditions when compared with unstimulated EGFR-WT. Scale bars, 500 nm.

(F) Diffusion coefficient comparison between EGFR-WT, EGFR-WT+EGF, and EGFR mutants. All mutants show a larger population of slow-diffusing receptors, but the difference between mutants is not significant.

(G) The $1 - CDF$ curves for each mutant and WT condition. The curves were obtained from fitting the PDFs of each condition to a power law and using the parameters to calculate the $1 - CDF$ function. The x intersection of each $1 - CDF$ function is defined as the 99th% percentile time ($\tau_{99\%}$). This is the time at which 99% of dimers have already dissociated and is obtained directly from the power-law fit parameter. The original $1 - CDF$ data is plotted in the inset. The dimer histograms and power law fits for each condition can be found in STAR Methods.

(H) The $\tau_{99\%}$ for each condition. The top and bottom edges of the boxes represent ±1 standard error from the mean, and the ends of the whiskers represent the 95% confidence interval. More details about the analysis of the dimer lifetime data can be found in STAR Methods.

See also Figures S3, S4, and S5.

Table 1. Summary information of UCNP single particle tracking data used for dimerization analysis and resulting parameters

Experimental condition	No. of videos	No. of dimers	No. of dimers > 1.5 s	α	$\delta\alpha$	$\tau_{99\%}$ (s)	$\delta\tau_{99\%}$ (s)	ρ (%)	$\delta\rho$ (%)	R^2	Bootstrap $\tau_{99\%}$ (s)	Bootstrap $\delta\tau_{99\%}$ (s)
EGFR, wild-type, no stimulation	11	2,752	254	2.93	0.20	16.3	4.1	1.2	0.4	0.923	16.4	1.1
EGFR, wild-type, EGF stimulation	20	9,241	2,063	2.23	0.05	62.8	9.6	7.9	1.8	0.979	63.0	3.3
EGFR, R108K, no stimulation	19	9,948	1,793	2.47	0.08	34.7	5.6	6.3	0.6	0.986	34.8	1.9
EGFR, A289V, no stimulation	9	4,882	1,063	2.38	0.08	42.1	7.8	6.0	0.9	0.967	42.3	3.0
EGFR, L858R, no stimulation	15	8,006	1,805	2.32	0.07	49.8	9.3	6.6	0.9	0.989	49.9	3.0
EGFR, 19del, no stimulation	10	5,523	1303	2.22	0.07	65.1	13.2	7.6	1.3	0.964	65.4	5.4
EGFR, insSVD, no stimulation	22	18,105	4,135	2.24	0.05	61.4	9.1	7.6	0.9	0.992	61.5	2.8
HER2, Wild-type, no stimulation	17	5,437	958	2.46	0.09	34.9	6.5	4.1	0.6	0.975	35.0	2.5
HER2, S310F, no stimulation	14	10,835	2,359	2.31	0.05	50.3	7.1	12.1	3.3	0.975	34.9	1.9
HER2, insYVMA, no stimulation	9	14,058	2,969	2.47	0.06	34.8	4.5	7.6	1.2	0.987	50.4	2.6
HER2, Wild-type, EGF stimulation	19	37,512	6,217	2.54	0.06	29.6	3.5	5.9	0.7	0.997	29.7	1.0
HER3, Wild-type, no stimulation	20	3,541	750	2.21	0.09	67.7	19.5	4.2	0.8	0.948	68.3	7.8
HER3, V104L, no stimulation	10	6,719	1,526	2.31	0.07	50.7	9.2	9.0	1.3	0.971	50.8	2.9
HER3, E928G, no stimulation	13	8,147	1,473	2.47	0.07	34.3	5.3	6.4	1.1	0.988	34.4	1.8
HER3, Wild-type, NRG1β stimulation	13	11,363	2,624	2.41	0.06	39.1	5.4	6.4	1.0	0.988	39.2	2.1
EGFR-HER2, no stimulation	13	6,428	1,227	2.37	0.07	40.9	7.3	5.3	1.0	0.979	41.0	2.2
EGFR-HER2, EGF stimulation	9	3,166	675	2.25	0.08	59.9	14.4	4.4	0.6	0.936	60.3	5.8
EGFR-HER3, no stimulation	13	5,549	1,087	2.39	0.07	40.9	6.9	4.8	0.6	0.968	41.0	2.8
EGFR-HER3, EGF stimulation	5	2,333	484	2.34	0.09	46.5	10.5	6.1	2.0	0.928	46.9	4.7
EGFR-HER3, NRG1β stimulation	15	18,730	4,046	2.33	0.05	47.3	6.2	5.6	0.7	0.993	47.4	2.2
HER2-HER3, no stimulation	27	12,897	2,082	2.48	0.07	33.6	5.0	3.1	0.4	0.991	33.7	1.7
HER2-HER3, NRG1β stimulation	18	7,777	1,730	2.29	0.07	53.5	10.0	6.1	1.0	0.986	53.6	3.3

α is the power law exponent parameter from fitting the dimer lifetime histogram to a power law. $\delta\alpha$ is the error in the fit. ρ is the average percentage of receptors dimerized, and $\delta\rho$ is the standard error in the mean. R2 is the fit quality parameter for the power law fits. Data S2, pages 3 to 6, show the fitted data for the alpha parameters.

stochastic events lasted less than 1.5 s (Figures S5G–S5I), and therefore, we used 1.5 s as the minimum duration for a dimer when fitting the lifetime distribution to a functional form, even though colocalization events shorter than 1.5 s can still represent a real dimer. Without EGF stimulation, 92% of transient dimers had lifetimes shorter than 1.5 s. With EGF stimulation, 78% of dimers had lifetimes shorter than 1.5 s, and we observed a substantial increase in stable dimers longer than any recorded for unstimulated EGFR, including one dimer lasting over 10 min (Figure 4A; example dimers can be found in Data S2, page 8).

While some previous studies have suggested that dimer lifetimes follow a single-exponential decay,[45,46] the normalized probability density distribution (PDF) on a log-log scale clearly shows a departure from a single exponential decay. Instead, it is well-described by a power-law distribution (Figures 4B and S5J), $PDF(\tau) \propto \tau^{-\alpha}$, where τ is the dimer lifetime and α is the exponent of the power law (Table 1; Figure S5K). A key distinction between a single exponential and a power-law distribution is that the latter has a heavier tail, meaning long-lived dimers occur more frequently than expected under an exponential decay. To reliably determine a power-law distribution, data should exhibit linear behavior on a log-log plot across at least two orders of magnitude in both axes.[79] This would require the measurement of dimer lifetimes for more than several minutes, which was infeasible previously. The exceptional photostability of UCNPs now enables the detection of these rare, long-lived populations that were often missed in previous experiments.

The observed power-law behavior suggests a model with a continuum of EGFR dimer affinities rather than a single, fixed affinity.[80,81] This is consistent with the structural flexibility of EGFR, which adopts multiple conformational states.[82–84] Dimerization of full-length EGFR involves several distinct interaction interfaces, such as the dimerization arm, the juxtamembrane domain latch, and asymmetric kinase domain dimerization, not all of which are necessarily engaged simultaneously for a given dimer. Additionally, the heterogeneous cellular membrane likely modulates local dimerization affinities, further contributing to the observed power-law behavior.

Since the PDF for a power-law distribution can be noisy in the tail region, we also plotted the $1 - CDF$ (cumulative distribution function) to better illustrate the impact of EGF on dimer lifetime (Figure 4C). On a log-log plot, $1 - CDF$ also appears linear for a power-law distribution. Note that since we only have a finite dataset, $1 - CDF$ eventually goes to zero. To quantitatively compare dimer stability across conditions, we defined a key metric $\tau_{99\%}$, the time at which 99% of dimers have dissociated

(Figure 4G). The $\tau_{99\%}$ values of 16.3 and 62.8 s in the absence and presence of EGF, respectively, highlight the significant stabilization of EGFR dimers upon EGF binding.

EGFR mutants show different levels of ligand-independent dimerization

We next investigated how dimerization dynamics are impacted by five oncogenic EGFR mutations: R108K, A289V, E746-A750del (Ex19del), D770_N771insSVD (Ex20ins), and L858R. R108K and A289V are two point mutations in the EGFR extracellular ligand-binding and dimerization arm frequently found in glioblastoma multiforme.[8,14,85,86] Recently, an X-ray crystallography study revealed that both R108K and A289V stabilize EGFR dimers activated by epiregulin, a weaker ligand compared with EGF, thus preventing EGFR from discriminating between the two ligands.[85] Additionally, SPT experiments showed that both R108K and A289V treated by either EGF or epiregulin were slowed down to a similar extent.[76] However, their ligand-free dimerization dynamics remain poorly understood. To address this, we transiently expressed Halo-EGFR-R108K or A289V in U2OS cells and performed dual-color SPT using Er10Yb90-HTL and Tm06Yb94-HTL. Similar expression levels of these two mutants were confirmed by western blot (Figure S3D).

Even in the absence of EGF stimulation, we directly observed ligand-independent dimerization events for both R108K (Figures 4D and 4E; Data S2, page 9) and A289V mutants (Data S2, page 10). HMM-Bayes analysis revealed a significant slowdown for both mutants without ligand stimulation (Figure 4F), which is different from previous results showing similar diffusion coefficients between wild-type, R108K, and A289V mutants with MSD analysis on Qdot-SPT trajectories.[76] Furthermore, both mutants exhibited increased dimer lifetimes compared with wild-type EGFR without ligands (Figures 4G, 4H, and S5K). The $\tau_{99\%}$ values of 34.7 s for R108K and 42.1 s for A289V showed their enhanced dimerization, which is correlated with their increased basal phosphorylation (Figure S3D).[14,87] We hypothesize that in these mutants, the tethered ECD conformation is destabilized, leading to an increased population of EGFR in the extended ECD form, which in turn facilitates dimerization. The slight difference in dimer stability may be attributed to variations in dimer structures,[85] although structures of ligand-free dimers have yet to be reported.

In non-small cell lung cancer (NSCLC), the three most frequent EGFR tyrosine-kinase mutations are Exon 19 deletions, Exon 20 insertions, and Exon 21 L858R mutation.[11,15,88,89] Here, we investigated the most common variant from each class: the Exon 19 deletion E745-A750del, the Exon 20 insertion D770_N771insSVD, and the Exon 21 L858R mutation. At similar expression levels (Figure S3D), all three mutations displayed even stronger ligand-independent dimerization compared with the ECD domain mutants (Figures 4G and 4H; Data S2, pages 10–12). Among them, Ex19del exhibited the longest $\tau_{99\%}$ of 65.1 s, indicating it forms the most stable dimers without ligand stimulation. Over the past decades, extensive studies have shown that these TKD mutations enhance basal EGFR phosphorylation in biochemical assays,[88,90] and we also confirmed the enhanced ligand-independent phosphorylation of these TKD mutants in U2OS cells (Figure S3D). Our SPT results demonstrate that these TKD mutants lead to significantly prolonged dimer lifetimes, suggesting that increased dimer stability without EGF stabilization directly contributes to elevated basal phosphorylation.

We propose that the enhanced dimerization of these TKD mutants arises from strong TKD-TKD interactions. Enhanced dimerization of lung cancer mutants with WT EGFR has been observed in cells, resulting in trans-phosphorylation of the WT receptor.[91] Previous biochemical studies reported a 20-fold lower dimer dissociation constant K_D for the L858R mutant compared with wild-type EGFR,[92] and crystal structures suggest that the L858R mutation destabilizes the inactive kinase conformation, thereby promoting dimerization.[93] Structures of an Exon 19 deletion[94] and Exon 20 insertions[95,96] also reveal an active conformation of the TKD, and our results indicated that these mutations enhance TKD dimerization to an even greater extent than L858R. Normally, without ligand activation, the tethered ECD conformation inhibits EGFR dimerization, preventing basal trans-phosphorylation of TKD. However, in TKD mutants, the affinity between the kinase domains may be strong enough to overcome this ECD inhibition, allowing ligand-independent dimerization and signaling.

Comparing ECD and TKD mutants, we find that TKD mutations exhibit even longer dimerization lifetimes, likely contributing to stronger ligand-independent signaling. Notably, all five EGFR mutants analyzed displayed similarly reduced diffusion rates, comparable with ligand-stimulated wild-type EGFR. The distributions of diffusion coefficients were indistinguishable across all mutants (Figure 4F), whereas $\tau_{99\%}$ values revealed distinct differences in dimer stability. Together, these results reinforce the canonical model in which EGFR signals through dimerization[25] and further suggest that TKD mutations are particularly effective in stabilizing EGFR dimers, thereby promoting ligand-independent signaling.

HER2 forms stable homodimers in live cells

HER2 and HER3 are unique members of the ErbB family receptors. Unlike the other three family members, no specific ligand has been identified for HER2. Structural studies have revealed that HER2's ECD adopts an open conformation.[26] Many studies have suggested that HER2 activation relies on heterodimerization with other ligand-bound ErbB family receptors,[5,31] and HER2 itself does not homodimerize.[97] However, *in vitro* studies of isolated HER2 TMD and TKD domains have suggested an intrinsic dimerization propensity.[92,98] Moreover, HER2 overexpression is frequently found in breast and lung cancers, where it also plays a strong oncogenic role. Ligand-independent activation of HER2 in NIH 3T3 cells further suggests the possibility of HER2 homodimerization.[12,99,100] Novel HER2 ECD mutants have also been found to promote HER2 homodimerization.[7,101] Nevertheless, it remains an open question how HER2 alone mediates its function and whether wild-type HER2 exhibits distinct dimerization dynamics compared with HER2 mutants.

To directly assess HER2 homodimerization, we performed SPT using UCNPs in U2OS cells expressing SNAP-tagged HER2, labeled with Tm06Yb94-STL and Er10Yb90-STL. We observed that HER2 can constitutively form homodimers, even in the absence of ErbB family ligand stimulation (Figure 5A; Data S2, page 14; Video S3). Moreover, many HER2

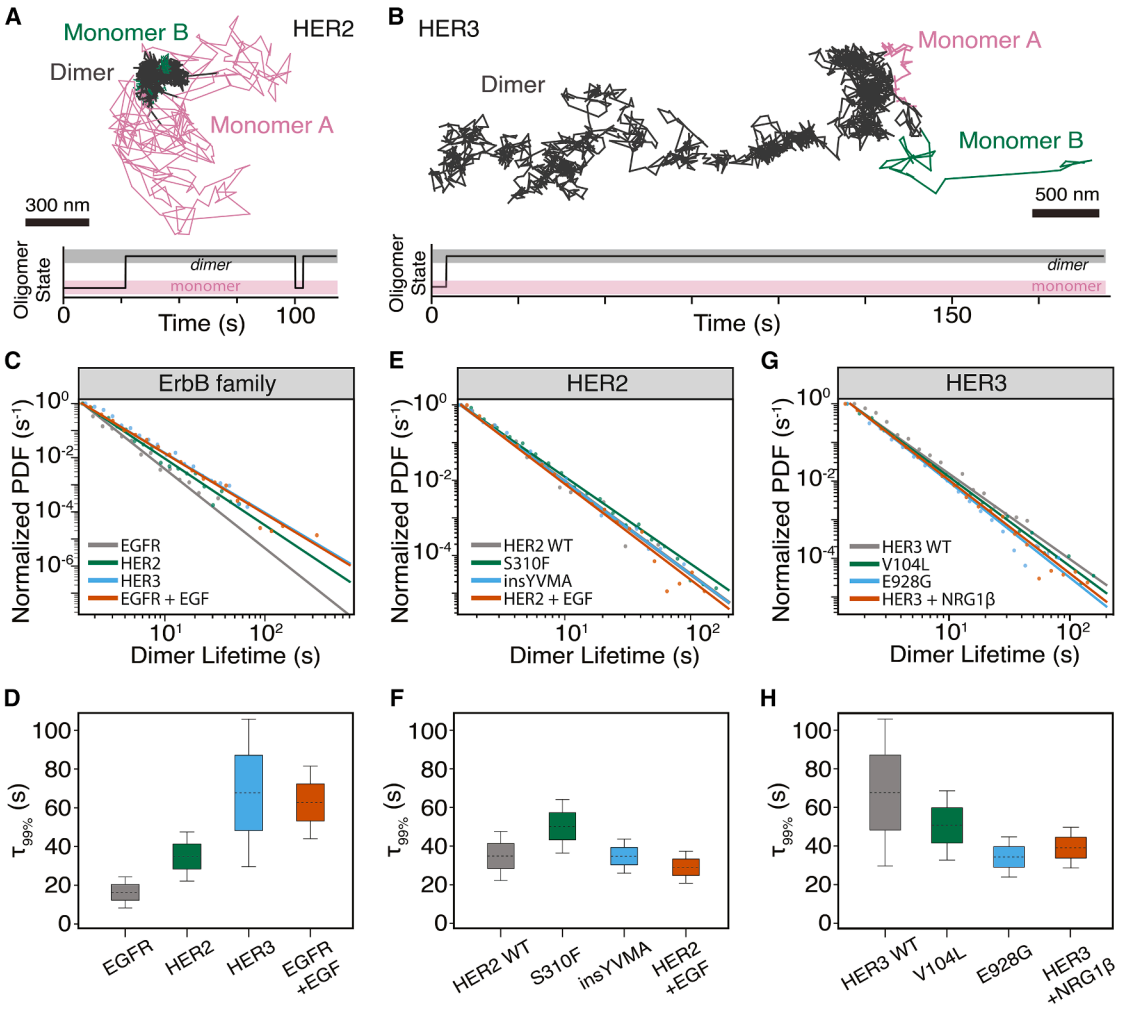

Figure 5. HER2 and HER3 homodimerization dynamics

(A) Trajectories of a long homodimer of HER2 in a U2OS cell. This dimer lasted about 75 s, then briefly separated and redimerized until the end of the recorded video, so the exact dimerization time afterward is unknown.

(B) Trajectories of a long (>3 min) homodimer of HER3 in a U2OS cell.

(C) Normalized probability distribution and fitted power law functions for the homodimer lifetimes of wild-type EGFR, HER2, and HER3. Notably, no dimers above 35 s were found for EGFR without EGF stimulation.

(D) $\tau_{99\%}$ for the ErbB family receptors. EGFR shows the smallest homodimerization lifetimes when compared with the other receptors in the family, but stimulation with EGF increases dimer lifetimes to levels similar to those of HER3. The colored box indicates the standard error, and the whiskers indicate the 95% confidence interval.

(E) Normalized PDFs and power-law fits for HER2, HER2 mutants, and EGF-stimulated HER2.

(F) $\tau_{99\%}$ for the HER2, HER2 mutants, and EGF-stimulated HER2.

(G) Normalized PDFs and power-law fits for HER3, HER3 mutants, and HER3 stimulated with NRG1β. (H) $\tau_{99\%}$ for HER3, HER3 mutants and HER3 stimulated with NRG1β.

The top and bottom edges of the boxes represent ±1 standard error from the mean, and the ends of the whiskers represent the 95% confidence interval.

See also Figures S3, S4, and S5.

homodimers exhibited lifetimes longer than those of unstimulated wild-type EGFR dimers (Figure 5C). Quantitative analysis of the dimer lifetime distribution revealed a $\tau_{99\%}$ of 34.9 s for HER2, which is more than double that of unstimulated EGFR, $\tau_{99\%}$ = 16.3 s (Figures 5D and S5K). We note that HER2 diffusion is slower than EGFR without ligand stimulation (Data S1, page 5). Our results are consistent with previous MD simulations that showed the lack of intrinsic disorder in the HER2 TKD domain, suggesting the kinase to dimerize more readily, similar to the EGFR TKD mutants.[92] Our direct observation of HER2 homodimers provides mechanistic insights into the oncogenic transformation of 3T3 cells by HER2 overexpression.[99,100] We also detected strong basal phosphorylation of HER2 transiently expressed in U2OS cells (Figure S3E). Notably, the endogenous EGFR, HER2, and HER3 remain hardly detectable by western blot (Figures S3D–S3F), compared with transiently transfected

HER2. These results suggest that HER2 homodimerization can lead to transphosphorylation of the HER2 TKD, resulting in activation of downstream signaling. Additionally, we treated U2OS cells expressing SNAP-HER2 with EGF, the specific ligand for EGFR (Figures 5E and 5F). The difference between the measured $\tau_{99\%}$ of 29.6 s and that of basal HER2 homodimerization was insignificant (Figure S5K), indicating that HER2 homodimerization was not modulated by EGF.

Oncogenic mutations enhance HER2 homodimer stability

We next investigated the effects of activating HER2 mutations commonly identified in lung and breast cancer—S310F and A775_G776insYVMA (insYVMA). Both mutants are known to be potently oncogenic and to promote downstream signaling via elevated C-terminal tail phosphorylation.[7] We expressed these HER2 mutants separately in U2OS cells at similar expression levels (Figure S3E). Western blotting showed that S310F and insYVMA mutants lead to stronger phosphorylation than HER2-WT (Figure S3E). Dual-color SPT revealed that S310F exhibited the longest $\tau_{99\%}$ (Figures 5E, 5F, and S5K). A recent structural study of a complete HER2-S310F ECD homodimer revealed that S310F stabilizes the dimer through a π-π interaction between S310F and Y274 of the dimerization partner.[102] Our SPT results directly show enhanced homodimerization of S310F, which explains the stronger phosphorylation. The HER2 insYVMA mutant, despite its increased kinase activity *in vitro*,[7,103] did not show a significant increase in dimer lifetimes. To further understand this, we calculated dimer fractions, which were calculated by averaging the ratio of observed dimer to monomer through each frame of tracking, under various conditions (Figure S5L; Table 1). For EGFR, there is a strong correlation between dimer fraction and dimer lifetime. A similar correlation was observed for HER2 wild-type and mutants, with S310F exhibiting the largest dimer fraction and the longest $\tau_{99\%}$. However, the insYVMA mutant, while having a $\tau_{99\%}$ similar to that of the wild-type, exhibited increased dimer fraction and phosphorylation. This suggests that the structural changes resulting from the insertion of residues 776–779 promote dimer formation and kinase activity but keep the dimer off-rate similar to wild-type. The enhanced phosphorylation in this case likely arises from a higher proportion of dimers or from intrinsic hyperactivation of the kinase domain. This pattern contrasts with EGFR kinase domain mutants, which tend to directly stabilize ligand-independent dimers. These results highlighted the advantage of our SPT method in capturing real-time dimer dynamics in their native environment, offering insights beyond those attainable through structural and biochemical analysis alone.

HER3 unexpectedly forms homodimers, which are destabilized by oncogenic mutations

Unlike HER2, the ECD domain of HER3 adopts a tethered conformation, similar to the structure of EGFR.[27] HER3 binds to ligands such as NRG1 with high affinity,[28] but its intracellular kinase domain is catalytically impaired,[104] which has long supported the assumption that HER3 cannot signal through homodimerization. Instead, HER3 is thought to function primarily as an allosteric activator by heterodimerizing with other ErbB family receptors, contributing to activation of downstream signaling.[25,29,32,98] However, *in vitro* studies have demonstrated that purified HER3 ECD can self-associate and even form higher-order oligomers.[35,36]

To determine whether full-length HER3 can homodimerize in the native cellular environment, we performed dual-color SPT in U2OS cells expressing Halo-HER3. Remarkably, we observed that HER3 can form stable and diffusing homodimers (Figure 5B; Data S2, page 18; Video S4), with dimer lifetimes even exceeding those of HER2 dimers (Figures 5C and 5D). The fitted $\tau_{99\%}$ of 67.7 s indicated robust dimer formation for HER3 without ligand stimulation. To verify that observed HER3 dimerization is not an artifact introduced by the fusion tag, we also expressed SNAP-HER3 and performed dual-color SPT. Similar distributions of dimer lifetimes and diffusion coefficients were obtained (Figures S4L and S5M), confirming the intrinsic nature of HER3 homodimerization. A recent study using fluorescence cross-correlation spectroscopy also detected HER3 homodimerization.[105]

Across the ErbB family, wild-type EGFR, HER2, and HER3 all demonstrate ligand-independent homodimerization, although to varying degrees (Figures 5C and 5D). Despite high sequence homology among ErbB family receptors,[5] their biophysical behaviors differ substantially, which may help explain the diverse signaling outcomes and functional roles triggered by each ErbB family receptor. In addition to dimers, we also detected higher-order oligomers from the tracking experiments, although our analysis here focused specifically on dimerization.

The unexpected homodimerization behavior of HER3 raises the possibility of a novel auto-inhibition mechanism in which HER3 homodimers represent a non-signaling reservoir that prevents HER3 from heterodimerizing with other ErbB family receptors. To further explore this hypothesis, we examined the live-cell dynamics of two common somatic HER3 mutations—E928G and V104L, which frequently occurred in breast cancer co-harboring HER2 and HER3 mutations.[106] In contrast to EGFR and HER2 mutants that typically stabilize homodimers, we found that both HER3 mutants destabilized the HER3 homodimer, with lower $\tau_{99\%}$ than that of wild-type HER3 (Figures 5G, 5H, and S5K). Notably, HER3 E928G, the most frequently observed of these mutants, exhibited the greatest destabilization of HER3 homodimers with the lowest $\tau_{99\%}$ of 34.3 s. Furthermore, we examined HER3 homodimerization under NRG1β stimulation (Figures 5G and 5H; Data S2, page 21). The $\tau_{99\%}$ decreased from 67.7 s under ligand-independent conditions to 39.1 s with NRG1β, indicating destabilization of HER3 homodimer by ligand binding (Figure S5K). Our live-cell results are consistent with previous *in vitro* observations.[35,36] These findings support the hypothesis that gain-of-function HER3 mutants and NRG1β binding disrupt HER3 homodimerization, increasing the availability of HER3 monomers to heterodimerize with other ErbB family receptors. The enhanced heterodimerization and downstream signaling thus contribute to oncogenic transformation.

Heterodimers are stabilized by EGF and NRG1β

In addition to homodimerization, we aimed at capturing the heterodimeric interactions among the ErbB family receptors. To this end, we first demonstrated our capability for three-color SPT of wild-type EGFR, HER2, and HER3 simultaneously in living cells using a single excitation laser. As shown in Figure 6A, the three

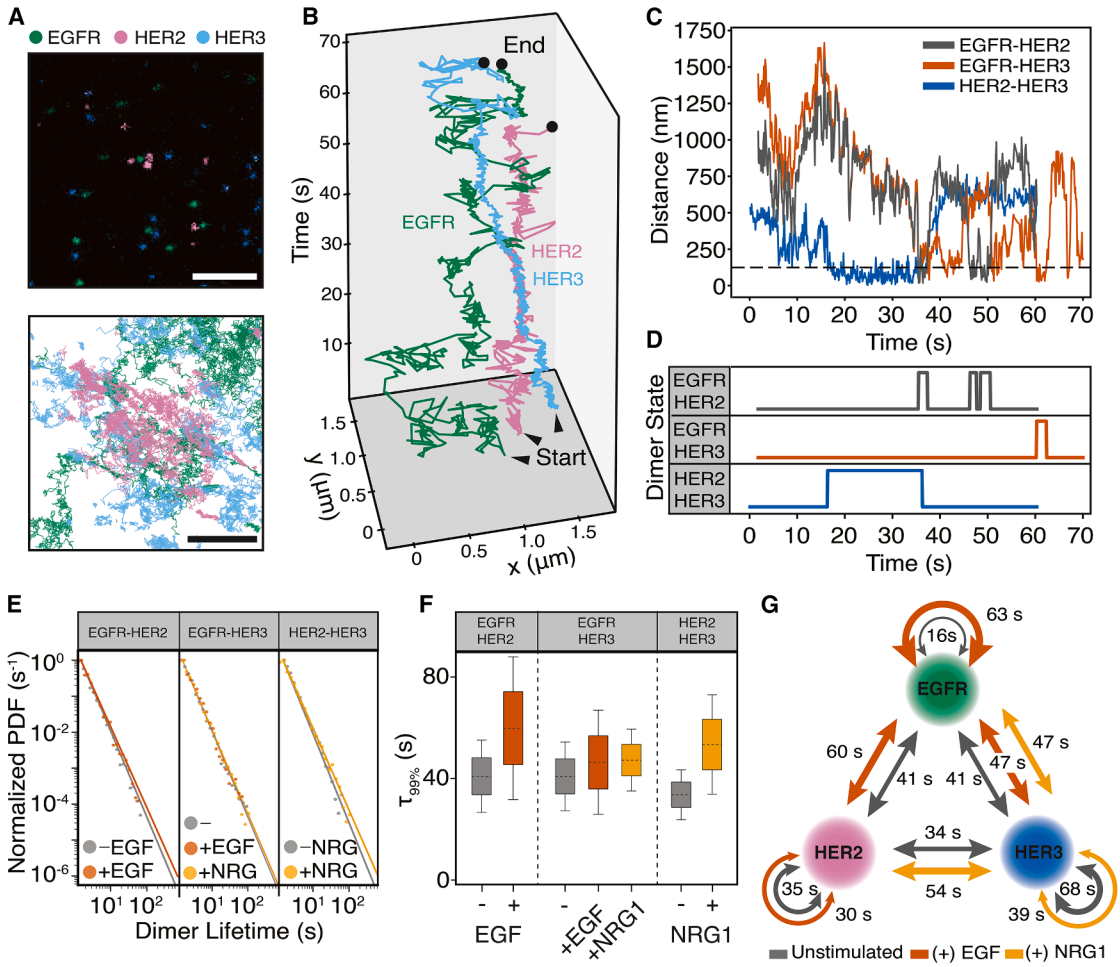

Figure 6. ErbB family receptors heterodimerization dynamics

(A) Top: Snapshot of a 10-min-long video of a U2OS cell expressing Halo-EGFR, SNAP-HER2, and CLIP-HER3. The receptors were specifically labeled with Er10Yb90-HTL, Tm10Yb80-STL, and Tm02Yb30-CTL, respectively (EGFR-Green, HER2-Red, HER3-Blue). Scale bars, 4 μm. Bottom: Trajectories reconstructed for all the tracked receptors in the video, with the same color scheme.

(B) Trajectories of a three-receptor interaction (one EGFR, one HER2, and one HER3) reconstructed from the video shown in (A).

(C) Receptor-receptor distances for EGFR-HER2, HER2-HER3, and EGFR-HER3, respectively. Dashed line indicates the dimerization threshold set at 125 nm.

(D) Dimer-state plots for EGFR-HER2, EGFR-HER3, and HER2-HER3.

(E) Normalized probability distributions and power law fits for the heterodimer lifetimes between ErbB Family receptors, as well as heterodimer lifetimes with ligand stimulation.

(F) $\tau_{99\%}$ for the heterodimers shown in (E). The top and bottom edges of the boxes represent ±1 standard error from the mean, and the ends of the whiskers represent the 95% confidence interval.

(G) Interaction network between EGFR, HER2, and HER3, characterized by $\tau_{99\%}$. The thickness of each arrow represents dimer stability. Stabilization of dimers by different ligands is also shown.

See also Figure S5.

co-expressed receptors were labeled with orthogonal self-labeling tags and imaged with UCNPs emitting in spectrally distinct channels (Halo-EGFR by Er10-HTL, SNAP-HER2 by Tm10-STL, HER3 by Tm02-CTL), achieving high signal-to-noise ratios and, to our knowledge, the first long-term SPT of three specific proteins over 10 min. Even in the absence of ligand stimulation, we observed ligand-independent heterodimer formation between the three ErbB family receptors (Figure 6B; Video S5). Figures 6B–6D and Video S5 show one representative example with multiple heterodimer partner exchanges. HER2 first formed a heterodimer with HER3, lasting for 20 s. 10 s after the dissociation of the HER2-HER3 heterodimer, HER2 switched to dimerize with an EGFR, though this heterodimer persisted for only 1.7 s. Lastly, the EGFR dissociated from HER2 and formed a heterodimer with HER3 for 2.1 s. We note that the photostability of UCNPs allows us to follow the same receptor and visualize its dimerization events separated further in time and space than the example shown here.

We next quantitatively analyzed the dynamics of heterodimerization across all three receptor pairs: EGFR-HER2, EGFR-HER3,

and HER2-HER3. To do this, we separately co-expressed the three combinations Halo-EGFR + SNAP-HER2, Halo-EGFR + SNAP-HER3, and Halo-HER3 + SNAP-HER2 in U2OS cells and performed dual-color SPT (Data S2, pages 22–24). Unexpectedly, under ligand-free conditions, all three heterodimer pairs exhibited $\tau_{99\%}$ comparable with that of HER2 homodimers and significantly longer than the unstimulated EGFR homodimer (Figures 6E and 6F; Table 1).

To assess the impact of ligand binding on heterodimer stability, we added EGF to cells expressing the EGFR-HER2 and EGFR-HER3 pairs. In both cases, we observed a notable increase in $\tau_{99\%}$, indicating EGF stabilizes EGFR-HER2 and EGFR-HER3 heterodimers, although not as stable compared with EGF-activated EGFR homodimers (Figures 6E–6G and S5K; Data S2, pages 25 and 26). These results are consistent with previous structural studies showing ligand-induced stabilization of the ECD of EGFR-HER2 heterodimer.[33] The increase in $\tau_{99\%}$ for EGFR-HER2 and EGFR-HER3 pairs after ligand stimulation is likely correlated with enhanced phosphorylation and downstream signaling.[33,107] We also evaluated the effect of NRG1β on HER2-HER3 and EGFR-HER3 heterodimerization (Figures 6E–6G and S5K; Data S2, pages 27 and 28). Addition of NRG1β stabilized HER2-HER3 heterodimerization, in agreement with the known structure of the stable HER2/HER3/NRG1β complex.[30] Ligand effect on EGFR-HER3 heterodimers varied, with EGF exerting a stronger stabilization than NRG1β. Comparing the $\tau_{99\%}$ across HER3 homodimers, HER2-HER3 heterodimers, and EGFR-HER3 heterodimers under NRG1β stimulation revealed that NRG1β promotes HER3 heterodimerization with other ErbB family receptors while destabilizing HER3 homodimers. This contrasts with EGF, which stabilizes both EGFR-HER3 heterodimers and EGFR homodimers. These observations underscore the distinct and context-dependent effects of ligand binding on ErbB receptor dimerization dynamics at the single-molecule level.

Taken together, our live-cell SPT results reveal a previously unrecognized population of stable, ligand-independent heterodimers of EGFR-HER2, EGFR-HER3, and HER2-HER3. These interactions, undetectable by traditional structural biology approaches, suggest a broader model of ErbB receptor signaling regulation, in which pre-formed heterodimers may allow for rapid ligand response or signal diversification.

DISCUSSION

ErbB family receptors engage in highly dynamic and heterogeneous interactions, forming a complex signaling network.[4] Dimerization acts as the fundamental unit of functional input, while C-terminal tail phosphorylation serves as the primary functional output. Ligand stimulation differentially stabilizes receptor dimers, leading to distinct downstream signaling outcomes.[108,109] Our results revealed that ligand-independent homodimerization and heterodimerization occur among EGFR, HER2, and HER3. Notably, the lifetimes of these homodimers vary significantly, potentially encoding different activity levels and diverse functions.

While the structural basis of EGFR activation and the role of EGF have been extensively studied, the biophysical dynamics of EGFR, including the effects of various activating mutations on the live cell membrane, remain incompletely understood. The technique developed here, employing photostable UCNPs to track individual receptors over extended periods, offers a unique tool to study real-time receptor-receptor interactions in their native cellular context. These long-time-scale observations are critical for understanding dynamic processes such as dimerization.

Our results comparing wild-type EGFR, ECD mutants, and TKD mutants suggest distinct roles for the tethered ECD and disordered TKD domains in dimer stability. Wild-type EGFR and ECD mutants share the same TKD, which intrinsically contributes to ligand-independent homodimerization. ECD mutants such as R108K and A289V potentially destabilize the tethered ECD conformation, enhancing ECD-ECD interactions and promoting more stable ligand-free dimers. In contrast, EGFR TKD mutations, including Ex19del, Ex20ins, and L858R, are expected to enhance dimerization because they promote the active conformation of the TKD that is induced upon dimerization, though their ECD conformations remain unclear. In effect, EGFR TKD mutations lower the energy barrier for dimerization by promoting the dimerization-competent conformation of the TKD. Collectively, our findings indicate that enhanced TKD-TKD interactions play a more dominant role in stabilizing ligand-free EGFR dimers than ECD mutations. Overall, the ligand-independent activation observed across mutant EGFRs supports a conserved mechanism of ErbB family receptor activation: the formation of an asymmetric TKD dimer that enables trans-phosphorylation and initiates downstream signaling.

HER2 is structurally and functionally distinct within the ErbB family of receptors. Although MD simulations have suggested that HER2 ECD dimers are inherently unstable,[110] we have directly observed HER2 homodimers in living cells. The difference in dimer lifetimes between wild-type HER2 and its activation mutants is smaller than that observed for EGFR, which may be attributed to HER2's inherently high TKD dimerization affinity and its relatively rigid ECD, lacking the ligand-induced conformational changes seen in other family members. The ability of HER2 and its mutants to homodimerize supports the broader model of ErbB family receptor activation via dimerization. Notably, the differences in dimer stabilization by EGFR and HER2 mutants are consistent with a distinct pattern: whereas EGFR-driven cancers are typically mutation-dependent, and HER2-driven cancers are frequently associated with receptor overexpression.[111–113]

Our findings suggest that HER3 may undergo a unique form of autoinhibition, leading to its distinct activation dynamics compared with those of EGFR and HER2. We directly observed ligand-independent HER3 homodimerization on the live-cell membrane. Given that HER3 exhibits the most stable ligand-independent homodimers among EGFR, HER2, and HER3, it is plausible that the equilibrium of HER3 ECD is shifted toward the open configuration compared with the tethered form, which can be locked by antibodies.[114] Because the HER3 kinase domain is catalytically impaired,[104] HER3 is traditionally studied in the context of heterodimers with other ErbB family receptors. However, our results reveal an additional regulatory mechanism in which HER3 homodimers may sequester the

receptor, reducing its availability for heterodimer formation. Furthermore, our analysis of HER3 mutants indicates that certain gain-of-function variants may enhance oncogenic signaling by destabilizing HER3 homodimers and shifting the balance from autoinhibitory homodimers to signaling-competent heterodimers. We propose a model in which resting HER3 predominantly exists in homodimers or higher-order oligomers,[35] acting as an autoinhibitory reservoir. Upon stimulation or engagement with EGFR or HER2, a dimer "partner exchange" may occur, converting the homodimer into an active heterodimer.

Heterodimerization among ErbB family receptors has been rarely explored in the context of single-molecule imaging. Our observation of unexpectedly long lifetimes for all three ligand-independent heterodimers suggests a combinatorial effect involving interactions between distinct ECD and TKD domains, resulting in enhanced dimer stability. These findings highlight that receptor-receptor interactions within the ErbB family are more complex than interactions within isolated domain types. We have observed unliganded homo- and heterodimers in this study. Notably, the EGFR kinase domain has been crystallized in a symmetric, inactive dimer conformation.[25] However, it remains unclear how the intracellular TKDs interact in the unliganded dimers we detect and whether these dimers are signaling competent. Elucidating the structural and functional roles of these unliganded dimers is an important direction for future study.

Ligand stimulation further stabilizes all heterodimers, consistent with previous MD simulations showing that single-ligand-bound ECDs within heterodimers exhibit increased interaction stability.[110] However, the unexpected stability of ligand-free heterodimers cannot be explained solely by ECD interactions, suggesting additional structural contributions. Future structural studies will be needed to elucidate the mechanisms. This overall pattern supports the canonical model of ErbB receptor activation, in which dimerization serves as the fundamental unit initiating downstream signaling.

With the advancement of ultralong-term SPT, we are now able to uncover unprecedented details of molecular interactions among ErbB family receptors. A wide range of ligands has been identified for these receptors,[9] and numerous antibodies and small-molecule inhibitors have been developed to target them.[115,116] We anticipate that the UCNP-SPT method will enable the investigation of how different ligands and therapeutics influence receptor dynamics at a level of detail that is not accessible by other existing techniques.

Limitations of the study

While the SPT software SLIMfast2 and Piscis[117] provide accurate and efficient tracking, certain limitations remain. The most common issue is trajectory truncation, which can occur when different PSFs come within diffraction-limited distances or briefly move out of the focal plane. We manually stitched many trajectories, but the missed events may modestly underestimate long dimer lifetimes. To assess the potential impact of this effect, we simulated dimerization events with different lifetime distributions and truncated the dimers at random intervals. We verified that the $\tau_{99\%}$ trends we observed were preserved and not biased by random truncation. Nevertheless, particle misidentification during close encounters remains a challenge, emphasizing the opportunity for future improvements in tracking algorithms optimized for high-density labeling.

Our current labeling strategy using fusion tags and UCNPs enables extended tracking while preserving receptor function, as verified by diffusion and signaling analyses. However, when labeling other molecular targets in future studies, potential perturbations may arise. To mitigate this, we are working to further reduce probe size without compromising spatiotemporal resolution.

The sparse labeling required to ensure robust SPT results in our calculated dimer fractions being a lower bound, which complicates the correlation of measured diffusion coefficients with receptor oligomeric state, particularly for apparent monomers that may interact with unlabeled partners. Computational methods such as FISIK[118,119] have been developed to infer accurate oligomerization kinetics by accounting for unlabeled populations, and we plan to incorporate these methods in future studies to deconvolute these effects.

Finally, although our approach provides robust insights into dimerization dynamics, it does not distinguish structural configurations such as symmetric versus asymmetric TKD dimers. Integrating our platform with complementary techniques, such as single-molecule FRET,[120] could help resolve these structural details.

RESOURCE AVAILABILITY

Lead contact

Requests for further information and resources should be directed to and will be fulfilled by the lead contact, Chunte Sam Peng (sampeng@mit.edu).

Materials availability

All plasmids and cell lines used in this study are available upon request.

Data and code availability

Public DepMap data (DepMep[6]) were referenced in this study. The integrated codes for single-particle tracking analysis and dimer analysis are available upon request and will be deposited on GitHub. All other codes and raw data are available upon request.

ACKNOWLEDGMENTS

We thank Kai Johnsson, Veselin Nasufovic, and Richard Wombacher for kindly providing the ligand and plasmid of SNAP-tag2 and CLIP-tag2; Kristyna Kotynkova and Gizem Karsli Uzunbas for valuable discussions; James Richardson for the code for image alignment; Zixin Chen and Qingji Lyu for assistance on western blot experiments; Dangliang Liu for validation of ligand-PEG conjugation; and Greg Schuette for assistance on the scaling and parallelization of the HMM-Bayes algorithm. TEM was carried out in part through the use of MIT.nano's facilities. We acknowledge the MIT SuperCloud and Lincoln Laboratory Supercomputing Center for providing HPC resources that have contributed to the HMM-Bayes analysis. This work was supported by the startup fund from the Broad Institute of MIT and Harvard, the MIT Charles E. Reed Faculty Initiatives Fund, the National Institutes of Health (5R00AG065516-04), the Alfred P. Sloan Foundation Matter-to-Life Award (G-2024-22448), and the G. Harold and Leila Y. Mathers Charitable Foundation. Z.N. is supported by the Fannie and John Hertz Foundation Fellowship; Paul & Daisy Soros Fellowships for New Americans; the US Department of Energy, Office of Science, Office of Advanced Scientific Computing Research; and the Department of Energy Computational Science Graduate Fellowship under award no. DE-SC0025528. C.S.P. thanks the Pfizer Gerald D. Laubach Career Development Professorship.

AUTHOR CONTRIBUTIONS

Conceptualization, H.G., M.M., and C.S.P.; methodology, K.M., X.M., J.F.S., Z.N. (computation), Y.K.L., S.M., A.D., L.G., H.G., M.M., and C.S.P.; investigation, K.M., X.M., J.F.S., Z.N. (computation), Y.K.L., S.M., A.D., and C.S.P.; visualization, K.M., J.F.S., and C.S.P.; funding acquisition, C.S.P.; supervision, M.J.E., H.G., M.M., and C.S.P.; writing—original draft, K.M., J.F.S., and C.S.P.; writing—review & editing, K.M., X.M., J.F.S., Y.K.L., M.J.E., H.G., M.M., and C.S.P.

DECLARATION OF INTERESTS

M.M. receives research support from Bayer. M.M. holds equity in Bayer, Delve Bio, and Isabl. M.M. is a consultant for Delve Bio. M.M. receives patent licensing payments from Bayer and LabCorp. H.G. receives research support from Bayer. H.G. receives licensing fee distributions from patents co-owned by Bayer, Broad Institute, and Dana-Farber Cancer Institute. M.J.E. is a consultant for Syndax Pharmaceuticals.

STAR★METHODS

Detailed methods are provided in the online version of this paper and include the following:

- KEY RESOURCES TABLE
- METHOD DETAILS
  - Nanoparticle synthesis and functionalization
  - Nanoparticle Size Analysis
  - Dynamic light scattering measurement
  - Zeta potential measurement
  - Microscope Setup
  - Single-UCNP brightness measurement
  - Measurement of number of ligands on UCNP-HTL
  - Confirmation of lack of interactions between the three ligand-conjugated UCNPs
  - Experimental Model and Study Participant Details
  - Plasmid construction and lentivirus preparation
  - Validation of non-perturbing effect of HaloTag7 fusion on EGFR
  - Western blotting
  - Live-cell imaging
  - Single-particle tracking analysis
  - Diffusion modes and coefficients analysis
  - MSD analysis
  - Motion blur error analysis
  - Image registration and error analysis
  - Dimer lifetime analysis
- QUANTIFICATION AND STATISTICAL ANALYSIS

SUPPLEMENTAL INFORMATION

Supplemental information can be found online at https://doi.org/10.1016/j.cell.2026.04.010.

Received: June 23, 2025
Revised: December 23, 2025
Accepted: April 3, 2026
Published: April 28, 2026

REFERENCES

1. Avraham, R., and Yarden, Y. (2011). Feedback regulation of EGFR signalling: decision making by early and delayed loops. Nat. Rev. Mol. Cell Biol. *12*, 104–117. https://doi.org/10.1038/nrm3048.

2. Lemmon, M.A., Schlessinger, J., and Ferguson, K.M. (2014). The EGFR Family: Not So Prototypical Receptor Tyrosine Kinases. Cold Spring Harb. Perspect. Biol. *6*, a020768. https://doi.org/10.1101/cshperspect.a020768.

3. Marmor, M.D., Skaria, K.B., and Yarden, Y. (2004). Signal transduction and oncogenesis by ErbB/HER receptors. Int. J. Radiat. Oncol. Biol. Phys. *58*, 903–913. https://doi.org/10.1016/j.ijrobp.2003.06.002.

4. Yarden, Y., and Sliwkowski, M.X. (2001). Untangling the ErbB signalling network. Nat. Rev. Mol. Cell Biol. *2*, 127–137. https://doi.org/10.1038/35052073.

5. Kovacs, E., Zorn, J.A., Huang, Y., Barros, T., and Kuriyan, J. (2015). A Structural Perspective on the Regulation of the Epidermal Growth Factor Receptor. Annu. Rev. Biochem. *84*, 739–764. https://doi.org/10.1146/annurev-biochem-060614-034402.

6. DepMap B (2024). DepMap 24Q4 Public. https://doi.org/10.25452/figshare.plus.27993248.v1.

7. Greulich, H., Kaplan, B., Mertins, P., Chen, T.-H., Tanaka, K.E., Yun, C.-H., Zhang, X., Lee, S.-H., Cho, J., Ambrogio, L., et al. (2012). Functional analysis of receptor tyrosine kinase mutations in lung cancer identifies oncogenic extracellular domain mutations of ERBB2. Proc. Natl. Acad. Sci. USA *109*, 14476–14481. https://doi.org/10.1073/pnas.1203201109.

8. Huang, P.H., Xu, A.M., and White, F.M. (2009). Oncogenic EGFR Signaling Networks in Glioma. Sci. Signal. *2*, re6. https://doi.org/10.1126/scisignal.287re6.

9. Yarden, Y. (2001). The EGFR family and its ligands in human cancer: signalling mechanisms and therapeutic opportunities. Eur. J. Cancer *37*, S3–S8. https://doi.org/10.1016/S0959-8049(01)00230-1.

10. Bièche, I., Onody, P., Tozlu, S., Driouch, K., Vidaud, M., and Lidereau, R. (2003). Prognostic value of ERBB family mRNA expression in breast carcinomas. Int. J. Cancer *106*, 758–765. https://doi.org/10.1002/ijc.11273.

11. da Cunha Santos, G., Shepherd, F.A., and Tsao, M.S. (2011). EGFR Mutations and Lung Cancer. Annu. Rev. Pathol. *6*, 49–69. https://doi.org/10.1146/annurev-pathol-011110-130206.

12. van de Vijver, M.J., Peterse, J.L., Mooi, W.J., Wisman, P., Lomans, J., Dalesio, O., and Nusse, R. (1988). Neu-Protein Overexpression in Breast Cancer. Association with Comedo-Type Ductal Carcinoma In Situ and Limited Prognostic Value in Stage II Breast Cancer. N. Engl. J. Med. *319*, 1239–1245. https://doi.org/10.1056/NEJM198811103191902.

13. Mendelsohn, J., and Baselga, J. (2000). The EGF receptor family as targets for cancer therapy. Oncogene *19*, 6550–6565. https://doi.org/10.1038/sj.onc.1204082.

14. Lee, J.C., Vivanco, I., Beroukhim, R., Huang, J.H.Y., Feng, W.L., DeBiasi, R.M., Yoshimoto, K., King, J.C., Nghiemphu, P., Yuza, Y., et al. (2006). Epidermal Growth Factor Receptor Activation in Glioblastoma through Novel Missense Mutations in the Extracellular Domain. PLOS Med. *3*, e485. https://doi.org/10.1371/journal.pmed.0030485.

15. Paez, J.G., Jänne, P.A., Lee, J.C., Tracy, S., Greulich, H., Gabriel, S., Herman, P., Kaye, F.J., Lindeman, N., Boggon, T.J., et al. (2004). EGFR Mutations in Lung Cancer: Correlation with Clinical Response to Gefitinib Therapy. Science *304*, 1497–1500. https://doi.org/10.1126/science.1099314.

16. Ogiso, H., Ishitani, R., Nureki, O., Fukai, S., Yamanaka, M., Kim, J.-H., Saito, K., Sakamoto, A., Inoue, M., Shirouzu, M., et al. (2002). Crystal Structure of the Complex of Human Epidermal Growth Factor and Receptor Extracellular Domains. Cell *110*, 775–787. https://doi.org/10.1016/S0092-8674(02)00963-7.

17. Schlessinger, J. (2002). Ligand-Induced, Receptor-Mediated Dimerization and Activation of EGF Receptor. Cell *110*, 669–672. https://doi.org/10.1016/S0092-8674(02)00966-2.

18. Garrett, T.P.J., McKern, N.M., Lou, M., Elleman, T.C., Adams, T.E., Lovrecz, G.O., Zhu, H.-J., Walker, F., Frenkel, M.J., Hoyne, P.A., et al. (2002). Crystal Structure of a Truncated Epidermal Growth Factor Receptor Extracellular Domain Bound to Transforming Growth Factor α. Cell *110*, 763–773. https://doi.org/10.1016/S0092-8674(02)00940-6.

19. Ferguson, K.M., Berger, M.B., Mendrola, J.M., Cho, H.S., Leahy, D.J., and Lemmon, M.A. (2003). EGF Activates Its Receptor by Removing Interactions that Autoinhibit Ectodomain Dimerization. Mol. Cell *11*, 507–517. https://doi.org/10.1016/S1097-2765(03)00047-9.

20. Molina, J.R., and Adjei, A.A. (2006). The Ras/Raf/MAPK pathway. J. Thorac. Oncol. *1*, 7–9. https://doi.org/10.1016/S1556-0864(15)31506-9.

21. Martinelli, E., Morgillo, F., Troiani, T., and Ciardiello, F. (2017). Cancer resistance to therapies against the EGFR-RAS-RAF pathway: The role of MEK. Cancer Treat. Rev. *53*, 61–69. https://doi.org/10.1016/j.ctrv.2016.12.001.

22. Downward, J. (2003). Targeting RAS signalling pathways in cancer therapy. Nat. Rev. Cancer *3*, 11–22. https://doi.org/10.1038/nrc969.

23. Cully, M., You, H., Levine, A.J., and Mak, T.W. (2006). Beyond PTEN mutations: the PI3K pathway as an integrator of multiple inputs during tumorigenesis. Nat. Rev. Cancer *6*, 184–192. https://doi.org/10.1038/nrc1819.

24. Chang, K.-Y., Tsai, S.-Y., Chen, S.-H., Tsou, H.-H., Yen, C.-J., Liu, K.-J., Fang, H.-L., Wu, H.-C., Chuang, B.-F., Chou, S.-W., et al. (2013). Dissecting the EGFR-PI3K-AKT pathway in oral cancer highlights the role of the EGFR variant III and its clinical relevance. J. Biomed. Sci. *20*, 43. https://doi.org/10.1186/1423-0127-20-43.

25. Zhang, X., Gureasko, J., Shen, K., Cole, P.A., and Kuriyan, J. (2006). An Allosteric Mechanism for Activation of the Kinase Domain of Epidermal Growth Factor Receptor. Cell *125*, 1137–1149. https://doi.org/10.1016/j.cell.2006.05.013.

26. Cho, H.-S., Mason, K., Ramyar, K.X., Stanley, A.M., Gabelli, S.B., Denney, D.W., and Leahy, D.J. (2003). Structure of the extracellular region of HER2 alone and in complex with the Herceptin Fab. Nature *421*, 756–760. https://doi.org/10.1038/nature01392.

27. Cho, H.-S., and Leahy, D.J. (2002). Structure of the Extracellular Region of HER3 Reveals an Interdomain Tether. Science *297*, 1330–1333. https://doi.org/10.1126/science.1074611.

28. Carraway, K.L., Sliwkowski, M.X., Akita, R., Platko, J.V., Guy, P.M., Nuijens, A., Diamonti, A.J., Vandlen, R.L., Cantley, L.C., and Cerione, R.A. (1994). The erbB3 gene product is a receptor for heregulin. J. Biol. Chem. *269*, 14303–14306. https://doi.org/10.1016/S0021-9258(17)36789-3.

29. Jura, N., Shan, Y., Cao, X., Shaw, D.E., and Kuriyan, J. (2009). Structural analysis of the catalytically inactive kinase domain of the human EGF receptor 3. Proc. Natl. Acad. Sci. USA *106*, 21608–21613. https://doi.org/10.1073/pnas.0912101106.

30. Diwanji, D., Trenker, R., Thaker, T.M., Wang, F., Agard, D.A., Verba, K.A., and Jura, N. (2021). Structures of the HER2–HER3–NRG1β complex reveal a dynamic dimer interface. Nature *600*, 339–343. https://doi.org/10.1038/s41586-021-04084-z.

31. Graus-Porta, D., Beerli, R.R., Daly, J.M., and Hynes, N.E. (1997). ErbB-2, the preferred heterodimerization partner of all ErbB receptors, is a mediator of lateral signaling. EMBO J. *16*, 1647–1655. https://doi.org/10.1093/emboj/16.7.1647.

32. Littlefield, P., Liu, L., Mysore, V., Shan, Y., Shaw, D.E., and Jura, N. (2014). Structural analysis of the EGFR/HER3 heterodimer reveals the molecular basis for activating HER3 mutations. Sci. Signal. *7*, ra114. https://doi.org/10.1126/scisignal.2005786.

33. Bai, X., Sun, P., Wang, X., Long, C., Liao, S., Dang, S., Zhuang, S., Du, Y., Zhang, X., Li, N., et al. (2023). Structure and dynamics of the EGFR/HER2 heterodimer. Cell Discov. *9*, 18. https://doi.org/10.1038/s41421-023-00523-5.

34. Peckys, D.B., Korf, U., and de Jonge, N. (2015). Local variations of HER2 dimerization in breast cancer cells discovered by correlative fluorescence and liquid electron microscopy. Sci. Adv. *1*, e1500165. https://doi.org/10.1126/sciadv.1500165.

35. Kani, K., Warren, C.M., Kaddis, C.S., Loo, J.A., and Landgraf, R. (2005). Oligomers of ERBB3 Have Two Distinct Interfaces That Differ in Their Sensitivity to Disruption by Heregulin. J. Biol. Chem. *280*, 8238–8247. https://doi.org/10.1074/jbc.M410944200.

36. Landgraf, R., and Eisenberg, D. (2000). Heregulin Reverses the Oligomerization of HER3. Biochemistry *39*, 8503–8511. https://doi.org/10.1021/bi000953+.

37. Kasai, R.S., Suzuki, K.G.N., Prossnitz, E.R., Koyama-Honda, I., Nakada, C., Fujiwara, T.K., and Kusumi, A. (2011). Full characterization of GPCR monomer–dimer dynamic equilibrium by single molecule imaging. J. Cell Biol. *192*, 463–480. https://doi.org/10.1083/jcb.201009128.

38. Zhou, P., Tsunoyama, T.A., Kasai, R.S., Hirosawa, K.M., Kalay, Z., Aladag, A., Fujiwara, T.K., Yokoyama, T., Sakamoto, M., Kise, R., et al. (2025). Single-molecule methods for characterizing receptor dimers reveal metastable opioid receptor homodimers that induce functional modulation. Nat. Commun. *16*, 9858. https://doi.org/10.1038/s41467-025-64694-3.

39. Nguyen, T.D., Chen, Y.-I., Chen, L.H., and Yeh, H.-C. (2023). Recent Advances in Single-Molecule Tracking and Imaging Techniques. Annu. Rev. Anal. Chem. (Palo Alto. Calif) *16*, 253–284. https://doi.org/10.1146/annurev-anchem-091922-073057.

40. Ha, T., Rasnik, I., Cheng, W., Babcock, H.P., Gauss, G.H., Lohman, T.M., and Chu, S. (2002). Initiation and re-initiation of DNA unwinding by the Escherichia coli Rep helicase. Nature *419*, 638–641. https://doi.org/10.1038/nature01083.

41. Gregorio, G.G., Masureel, M., Hilger, D., Terry, D.S., Juette, M., Zhao, H., Zhou, Z., Perez-Aguilar, J.M., Hauge, M., Mathiasen, S., et al. (2017). Single-molecule analysis of ligand efficacy in β_2AR-G-protein activation. Nature *547*, 68–73. https://doi.org/10.1038/nature22354.

42. Asher, W.B., Geggier, P., Holsey, M.D., Gilmore, G.T., Pati, A.K., Meszaros, J., Terry, D.S., Mathiasen, S., Kaliszewski, M.J., McCauley, M.D., et al. (2021). Single-molecule FRET imaging of GPCR dimers in living cells. Nat. Methods *18*, 397–405. https://doi.org/10.1038/s41592-021-01081-y.

43. Zhuang, X., Kim, H., Pereira, M.J.B., Babcock, H.P., Walter, N.G., and Chu, S. (2002). Correlating structural dynamics and function in single ribozyme molecules. Science *296*, 1473–1476. https://doi.org/10.1126/science.1069013.

44. Wilmes, S., Hafer, M., Vuorio, J., Tucker, J.A., Winkelmann, H., Löchte, S., Stanly, T.A., Pulgar Prieto, K.D., Poojari, C., Sharma, V., et al. (2020). Mechanism of homodimeric cytokine receptor activation and dysregulation by oncogenic mutations. Science *367*, 643–652. https://doi.org/10.1126/science.aaw3242.

45. Chung, I., Akita, R., Vandlen, R., Toomre, D., Schlessinger, J., and Mellman, I. (2010). Spatial control of EGF receptor activation by reversible dimerization on living cells. Nature *464*, 783–787. https://doi.org/10.1038/nature08827.

46. Low-Nam, S.T., Lidke, K.A., Cutler, P.J., Roovers, R.C., van Bergen en Henegouwen, P.M.P., Wilson, B.S., and Lidke, D.S. (2011). ErbB1 dimerization is promoted by domain co-confinement and stabilized by ligand binding. Nat. Struct. Mol. Biol. *18*, 1244–1249. https://doi.org/10.1038/nsmb.2135.

47. Liu, Y.-L., Perillo, E.P., Liu, C., Yu, P., Chou, C.-K., Hung, M.-C., Dunn, A.K., and Yeh, H.-C. (2016). Segmentation of 3D Trajectories Acquired by TSUNAMI Microscope: An Application to EGFR Trafficking. Biophys. J. *111*, 2214–2227. https://doi.org/10.1016/j.bpj.2016.09.041.

48. Sako, Y., Minoghchi, S., and Yanagida, T. (2000). Single-molecule imaging of EGFR signalling on the surface of living cells. Nat. Cell Biol. *2*, 168–172. https://doi.org/10.1038/35004044.

49. Ibach, J., Radon, Y., Gelléri, M., Sonntag, M.H., Brunsveld, L., Bastiaens, P.I.H., and Verveer, P.J. (2015). Single Particle Tracking Reveals that EGFR Signaling Activity Is Amplified in Clathrin-Coated Pits. PLOS One *10*, e0143162. https://doi.org/10.1371/journal.pone.0143162.

50. Kim, D.-H., Park, S., Kim, D.-K., Jeong, M.G., Noh, J., Kwon, Y., Zhou, K., Lee, N.K., and Ryu, S.H. (2018). Direct visualization of single-molecule membrane protein interactions in living cells. PLOS Biol. *16*, e2006660. https://doi.org/10.1371/journal.pbio.2006660.

51. Rasnik, I., McKinney, S.A., and Ha, T. (2006). Nonblinking and long-lasting single-molecule fluorescence imaging. Nat. Methods *3*, 891–893. https://doi.org/10.1038/nmeth934.

52. Altman, R.B., Terry, D.S., Zhou, Z., Zheng, Q., Geggier, P., Kolster, R.A., Zhao, Y., Javitch, J.A., Warren, J.D., and Blanchard, S.C. (2011). Cyanine fluorophore derivatives with enhanced photostability. Nat. Methods *9*, 68–71. https://doi.org/10.1038/nmeth.1774.

53. Tsunoyama, T.A., Watanabe, Y., Goto, J., Naito, K., Kasai, R.S., Suzuki, K.G.N., Fujiwara, T.K., and Kusumi, A. (2018). Super-long single-molecule tracking reveals dynamic-anchorage-induced integrin function. Nat. Chem. Biol. *14*, 497–506. https://doi.org/10.1038/s41589-018-0032-5.

54. Grimm, J.B., Xie, L., Casler, J.C., Patel, R., Tkachuk, A.N., Falco, N., Choi, H., Lippincott-Schwartz, J., Brown, T.A., Glick, B.S., et al. (2021). A General Method to Improve Fluorophores Using Deuterated Auxochromes. JACS Au *1*, 690–696. https://doi.org/10.1021/jacsau.1c00006.

55. Kim, D.-H., Triet, H.M., Lee, S.H., Jazani, S., Jang, S., Abedi, S.A.A., Liu, X., Seo, J., Ha, T., Chang, Y.-T., et al. (2025). Super-photostable organic dye for long-term live-cell single-protein imaging. Nat. Methods *22*, 550–558. https://doi.org/10.1038/s41592-024-02584-0.

56. Catapano, C., Dietz, M.S., Kompa, J., Jang, S., Freund, P., Johnsson, K., and Heilemann, M. (2025). Long-Term Single-Molecule Tracking in Living Cells using Weak-Affinity Protein Labeling. Angew. Chem. Int. Ed. Engl. *64*, e202413117. https://doi.org/10.1002/anie.202413117.

57. F Shida, J., Ma, K., Toll, H.W., Salinas, O., Ma, X., and Peng, C.S. (2024). Multicolor Long-Term Single-Particle Tracking Using 10 nm Upconverting Nanoparticles. Nano Lett. *24*, 4194–4201. https://doi.org/10.1021/acs.nanolett.4c00207.

58. Wu, S., Han, G., Milliron, D.J., Aloni, S., Altoe, V., Talapin, D.V., Cohen, B.E., and Schuck, P.J. (2009). Non-blinking and photostable upconverted luminescence from single lanthanide-doped nanocrystals. Proc. Natl. Acad. Sci. USA *106*, 10917–10921. https://doi.org/10.1073/pnas.0904792106.

59. Gargas, D.J., Chan, E.M., Ostrowski, A.D., Aloni, S., Altoe, M.V.P., Barnard, E.S., Sanii, B., Urban, J.J., Milliron, D.J., Cohen, B.E., et al. (2014). Engineering bright sub-10-nm upconverting nanocrystals for single-molecule imaging. Nat. Nanotechnol. *9*, 300–305. https://doi.org/10.1038/nnano.2014.29.

60. Liu, Y., Lu, Y., Yang, X., Zheng, X., Wen, S., Wang, F., Vidal, X., Zhao, J., Liu, D., Zhou, Z., et al. (2017). Amplified stimulated emission in upconversion nanoparticles for super-resolution nanoscopy. Nature *543*, 229–233. https://doi.org/10.1038/nature21366.

61. Tian, B., Fernandez-Bravo, A., Najafiaghdam, H., Torquato, N.A., Altoe, M.V.P., Teitelboim, A., Tajon, C.A., Tian, Y., Borys, N.J., Barnard, E.S., et al. (2018). Low irradiance multiphoton imaging with alloyed lanthanide nanocrystals. Nat. Commun. *9*, 3082. https://doi.org/10.1038/s41467-018-05577-8.

62. Liu, Q., Zhang, Y., Peng, C.S., Yang, T., Joubert, L.-M., and Chu, S. (2018). Single upconversion nanoparticle imaging at sub-10 W cm2 irradiance. Nat. Photonics *12*, 548–553. https://doi.org/10.1038/s41566-018-0217-1.

63. Nam, S.H., Bae, Y.M., Park, Y.I., Kim, J.H., Kim, H.M., Choi, J.S., Lee, K.T., Hyeon, T., and Suh, Y.D. (2011). Long-term real-time tracking of lanthanide ion doped upconverting nanoparticles in living cells. Angew. Chem. Int. Ed. Engl. *50*, 6093–6097. https://doi.org/10.1002/anie.201007979.

64. Peng, C.S., Zhang, Y., Liu, Q., Marti, G.E., Huang, Y.A., Südhof, T.C., Cui, B., and Chu, S. (2024). Nanometer-resolution tracking of single cargo reveals dynein motor mechanisms. Nat. Chem. Biol. *21*, 648–656. https://doi.org/10.1038/s41589-024-01694-2.

65. Chan, E.M., Gargas, D.J., Schuck, P.J., and Milliron, D.J. (2012). Concentrating and recycling energy in lanthanide codopants for efficient and spectrally pure emission: the case of NaYF4:Er3+/Tm3+ upconverting nanocrystals. J. Phys. Chem. B *116*, 10561–10570. https://doi.org/10.1021/jp302401j.

66. Wilhelm, J., Kühn, S., Tarnawski, M., Gotthard, G., Tünnermann, J., Tänzer, T., Karpenko, J., Mertes, N., Xue, L., Uhrig, U., et al. (2021). Kinetic and Structural Characterization of the Self-Labeling Protein Tags HaloTag7, SNAP-tag, and CLIP-tag. Biochemistry *60*, 2560–2575. https://doi.org/10.1021/acs.biochem.1c00258.

67. Siefe, C., Mehlenbacher, R.D., Peng, C.S., Zhang, Y., Fischer, S., Lay, A., McLellan, C.A., Alivisatos, A.P., Chu, S., and Dionne, J.A. (2019). Sub-20 nm Core-Shell-Shell Nanoparticles for Bright Upconversion and Enhanced Forster Resonant Energy Transfer. J. Am. Chem. Soc. *141*, 16997–17005. https://doi.org/10.1021/jacs.9b09571.

68. Zhong, Y., Ma, Z., Zhu, S., Yue, J., Zhang, M., Antaris, A.L., Yuan, J., Cui, R., Wan, H., Zhou, Y., et al. (2017). Boosting the down-shifting luminescence of rare-earth nanocrystals for biological imaging beyond 1500 nm. Nat. Commun. *8*, 737. https://doi.org/10.1038/s41467-017-00917-6.

69. Di Corato, R.D., Quarta, A., Piacenza, P., Ragusa, A., Figuerola, A., Buonsanti, R., Cingolani, R., Manna, L., and Pellegrino, T. (2008). Water solubilization of hydrophobic nanocrystals by means of poly(maleic anhydride-alt-1-octadecene). J. Mater. Chem. *18*, 1991–1996. https://doi.org/10.1039/B717801H.

70. Ohana, R.F., Encell, L.P., Zhao, K., Simpson, D., Slater, M.R., Urh, M., and Wood, K.V. (2009). HaloTag7: A genetically engineered tag that enhances bacterial expression of soluble proteins and improves protein purification. Protein Expr. Purif. *68*, 110–120. https://doi.org/10.1016/j.pep.2009.05.010.

71. Kühn, S., Nasufovic, V., Wilhelm, J., Kompa, J., de Lange, E.M.F., Lin, Y.-H., Egoldt, C., Fischer, J., Lennoi, A., Tarnawski, M., et al. (2025). SNAP-tag2 for faster and brighter protein labeling. Nat. Chem. Biol. *21*, 1754–1761. https://doi.org/10.1038/s41589-025-01942-z.

72. Nasufovic, V., Pišpek, A., Kühn, S., Bibrowski, M., Fischer, J., Wilhelm, J., Koch, B., Kompa, J., Mao, R., Tarnawski, M., et al. (2026). Fast and Luminous: CLIP-tag2. bioRxiv. https://doi.org/10.64898/2026.03.05.709795.

73. Kobayashi, S., Boggon, T.J., Dayaram, T., Jänne, P.A., Kocher, O., Meyerson, M., Johnson, B.E., Eck, M.J., Tenen, D.G., and Halmos, B. (2005). EGFR Mutation and Resistance of Non–Small-Cell Lung Cancer to Gefitinib. N. Engl. J. Med. *352*, 786–792. https://doi.org/10.1056/NEJMoa044238.

74. Park, M.-Y., Jung, M.H., Eo, E.Y., Kim, S., Lee, S.H., Lee, Y.J., Park, J.S., Cho, Y.J., Chung, J.H., Kim, C.H., et al. (2017). Generation of lung cancer cell lines harboring EGFR T790M mutation by CRISPR/Cas9-mediated genome editing. Oncotarget *8*, 36331–36338. https://doi.org/10.18632/oncotarget.16752.

75. Monnier, N., Barry, Z., Park, H.Y., Su, K.-C., Katz, Z., English, B.P., Dey, A., Pan, K., Cheeseman, I.M., Singer, R.H., et al. (2015). Inferring transient particle transport dynamics in live cells. Nat. Methods *12*, 838–840. https://doi.org/10.1038/nmeth.3483.

76. Mudumbi, K.C., Burns, E.A., Schodt, D.J., Petrova, Z.O., Kiyatkin, A., Kim, L.W., Mangiacapre, E.M., Ortiz-Caraveo, I., Rivera Ortiz, H., Hu, C., et al. (2024). Distinct interactions stabilize EGFR dimers and higher-

order oligomers in cell membranes. Cell Rep. *43*, 113603. https://doi.org/10.1016/j.celrep.2023.113603.

77. Yu, X., Sharma, K.D., Takahashi, T., Iwamoto, R., and Mekada, E. (2002). Ligand-independent Dimer Formation of Epidermal Growth Factor Receptor (EGFR) Is a Step Separable from Ligand-induced EGFR Signaling. Mol. Biol. Cell *13*, 2547–2557. https://doi.org/10.1091/mbc.01-08-0411.

78. Lemmon, M.A., Bu, Z., Ladbury, J.E., Zhou, M., Pinchasi, D., Lax, I., Engelman, D.M., and Schlessinger, J. (1997). Two EGF molecules contribute additively to stabilization of the EGFR dimer. EMBO J. *16*, 281–294. https://doi.org/10.1093/emboj/16.2.281.

79. Stumpf, M.P.H., and Porter, M.A. (2012). Mathematics. Critical Truths About Power Laws. Science *335*, 665–666. https://doi.org/10.1126/science.1216142.

80. Normanno, D., Boudarène, L., Dugast-Darzacq, C., Chen, J., Richter, C., Proux, F., Bénichou, O., Voituriez, R., Darzacq, X., and Dahan, M. (2015). Probing the target search of DNA-binding proteins in mammalian cells using TetR as model searcher. Nat. Commun. *6*, 7357. https://doi.org/10.1038/ncomms8357.

81. Cao, J. (2001). Single molecule waiting time distribution functions in quantum processes. J. Chem. Phys. *114*, 5137–5140. https://doi.org/10.1063/1.1342217.

82. Arkhipov, A., Shan, Y., Das, R., Endres, N.F., Eastwood, M.P., Wemmer, D.E., Kuriyan, J., and Shaw, D.E. (2013). Architecture and membrane interactions of the EGF receptor. Cell *152*, 557–569. https://doi.org/10.1016/j.cell.2012.12.030.

83. Srinivasan, S., Regmi, R., Lin, X., Dreyer, C.A., Chen, X., Quinn, S.D., He, W., Coleman, M.A., Carraway, K.L., Zhang, B., et al. (2022). Ligand-induced transmembrane conformational coupling in monomeric EGFR. Nat. Commun. *13*, 3709. https://doi.org/10.1038/s41467-022-31299-z.

84. Kaplan, M., Narasimhan, S., de Heus, C., Mance, D., van Doorn, S., Houben, K., Popov-Čeleketić, D., Damman, R., Katrukha, E.A., Jain, P., et al. (2016). EGFR Dynamics Change during Activation in Native Membranes as Revealed by NMR. Cell *167*, 1241–1251.e11. https://doi.org/10.1016/j.cell.2016.10.038.

85. Hu, C., Leche, C.A., Kiyatkin, A., Yu, Z., Stayrook, S.E., Ferguson, K.M., and Lemmon, M.A. (2022). Glioblastoma mutations alter EGFR dimer structure to prevent ligand bias. Nature *602*, 518–522. https://doi.org/10.1038/s41586-021-04393-3.

86. Brennan, C.W., Verhaak, R.G.W., McKenna, A., Campos, B., Noushmehr, H., Salama, S.R., Zheng, S., Chakravarty, D., Sanborn, J.Z., Berman, S.H., et al. (2013). The Somatic Genomic Landscape of Glioblastoma. Cell *155*, 462–477. https://doi.org/10.1016/j.cell.2013.09.034.

87. Orellana, L., Thorne, A.H., Lema, R., Gustavsson, J., Parisian, A.D., Hospital, A., Cordeiro, T.N., Bernadó, P., Scott, A.M., Brun-Heath, I., et al. (2019). Oncogenic mutations at the EGFR ectodomain structurally converge to remove a steric hindrance on a kinase-coupled cryptic epitope. Proc. Natl. Acad. Sci. USA *116*, 10009–10018. https://doi.org/10.1073/pnas.1821442116.

88. Greulich, H., Chen, T.-H., Feng, W., Jänne, P.A., Alvarez, J.V., Zappaterra, M., Bulmer, S.E., Frank, D.A., Hahn, W.C., Sellers, W.R., et al. (2005). Oncogenic Transformation by Inhibitor-Sensitive and -Resistant EGFR Mutants. PLOS Med. *2*, e313. https://doi.org/10.1371/journal.pmed.0020313.

89. Sharma, S.V., Bell, D.W., Settleman, J., and Haber, D.A. (2007). Epidermal growth factor receptor mutations in lung cancer. Nat. Rev. Cancer *7*, 169–181. https://doi.org/10.1038/nrc2088.

90. Du, Z., Brown, B.P., Kim, S., Ferguson, D., Pavlick, D.C., Jayakumaran, G., Benayed, R., Gallant, J.-N., Zhang, Y.-K., Yan, Y., et al. (2021). Structure–function analysis of oncogenic EGFR Kinase Domain Duplication reveals insights into activation and a potential approach for therapeutic targeting. Nat. Commun. *12*, 1382. https://doi.org/10.1038/s41467-021-21613-6.

91. Red Brewer, M., Yun, C.-H., Lai, D., Lemmon, M.A., Eck, M.J., and Pao, W. (2013). Mechanism for activation of mutated epidermal growth factor receptors in lung cancer. Proc. Natl. Acad. Sci. USA *110*, E3595–E3604. https://doi.org/10.1073/pnas.1220050110.

92. Shan, Y., Eastwood, M.P., Zhang, X., Kim, E.T., Arkhipov, A., Dror, R.O., Jumper, J., Kuriyan, J., and Shaw, D.E. (2012). Oncogenic Mutations Counteract Intrinsic Disorder in the EGFR Kinase and Promote Receptor Dimerization. Cell *149*, 860–870. https://doi.org/10.1016/j.cell.2012.02.063.

93. Yun, C.-H., Boggon, T.J., Li, Y., Woo, M.S., Greulich, H., Meyerson, M., and Eck, M.J. (2007). Structures of Lung Cancer-Derived EGFR Mutants and Inhibitor Complexes: Mechanism of Activation and Insights into Differential Inhibitor Sensitivity. Cancer Cell *11*, 217–227. https://doi.org/10.1016/j.ccr.2006.12.017.

94. van Alderwerelt van Rosenburgh, I.K., Lu, D.M., Grant, M.J., Stayrook, S.E., Phadke, M., Walther, Z., Goldberg, S.B., Politi, K., Lemmon, M.A., Ashtekar, K.D., et al. (2022). Biochemical and structural basis for differential inhibitor sensitivity of EGFR with distinct exon 19 mutations. Nat. Commun. *13*, 6791. https://doi.org/10.1038/s41467-022-34398-z.

95. Yasuda, H., Park, E., Yun, C.-H., Sng, N.J., Lucena-Araujo, A.R., Yeo, W.-L., Huberman, M.S., Cohen, D.W., Nakayama, S., Ishioka, K., et al. (2013). Structural, Biochemical, and Clinical Characterization of Epidermal Growth Factor Receptor (EGFR) Exon 20 Insertion Mutations in Lung Cancer. Sci. Transl. Med. *5*, 216ra177. https://doi.org/10.1126/scitranslmed.3007205.

96. Pagliarini, R.A., Henderson, J.A., Milgram, B.C., Borrelli, D.R., Brooijmans, N., Hilbert, B.J., Huff, M.R., Ito, T., Kryukov, G.V., Ladd, B., et al. (2025). STX-721, a Covalent EGFR/HER2 Exon 20 Inhibitor, Utilizes Exon 20–Mutant Dynamic Protein States and Achieves Unique Mutant Selectivity Across Human Cancer Models. Clin. Cancer Res. *31*, 3002–3018. https://doi.org/10.1158/1078-0432.CCR-24-3833.

97. Klapper, L.N., Glathe, S., Vaisman, N., Hynes, N.E., Andrews, G.C., Sela, M., and Yarden, Y. (1999). The ErbB-2/HER2 oncoprotein of human carcinomas may function solely as a shared coreceptor for multiple stroma-derived growth factors. Proc. Natl. Acad. Sci. USA *96*, 4995–5000. https://doi.org/10.1073/pnas.96.9.4995.

98. Monsey, J., Shen, W., Schlesinger, P., and Bose, R. (2010). Her4 and Her2/neu Tyrosine Kinase Domains Dimerize and Activate in a Reconstituted *in Vitro* System. J. Biol. Chem. *285*, 7035–7044. https://doi.org/10.1074/jbc.M109.096032.

99. Hudziak, R.M., Schlessinger, J., and Ullrich, A. (1987). Increased expression of the putative growth factor receptor p185HER2 causes transformation and tumorigenesis of NIH 3T3 cells. Proc. Natl. Acad. Sci. USA *84*, 7159–7163. https://doi.org/10.1073/pnas.84.20.7159.

100. Di Fiore, P.P., Pierce, J.H., Kraus, M.H., Segatto, O., King, C.R., and Aaronson, S.A. (1987). erbB-2 Is a Potent Oncogene When Overexpressed in NIH/3T3 Cells. Science *237*, 178–182. https://doi.org/10.1126/science.2885917.

101. Ishiyama, N., O'Connor, M., Salomatov, A., Romashko, D., Thakur, S., Mentes, A., Hopkins, J.F., Frampton, G.M., Albacker, L.A., Kohlmann, A., et al. (2023). Computational and Functional Analyses of HER2 Mutations Reveal Allosteric Activation Mechanisms and Altered Pharmacologic Effects. Cancer Res. *83*, 1531–1542. https://doi.org/10.1158/0008-5472.CAN-21-0940.

102. Bang, I., Hattori, T., Leloup, N., Corrado, A., Nyamaa, A., Koide, A., Geles, K., Buck, E., and Koide, S. (2025). Selective targeting of oncogenic hotspot mutations of the HER2 extracellular domain. Nat. Chem. Biol. *21*, 706–715. https://doi.org/10.1038/s41589-024-01751-w.

103. Wang, S.E., Narasanna, A., Perez-Torres, M., Xiang, B., Wu, F.Y., Yang, S., Carpenter, G., Gazdar, A.F., Muthuswamy, S.K., and Arteaga, C.L. (2006). HER2 kinase domain mutation results in constitutive phosphorylation and activation of HER2 and EGFR and resistance to EGFR tyrosine kinase inhibitors. Cancer Cell *10*, 25–38. https://doi.org/10.1016/j.ccr.2006.05.023.

104. Guy, P.M., Platko, J.V., Cantley, L.C., Cerione, R.A., and Carraway, K.L. (1994). Insect cell-expressed p180erbB3 possesses an impaired tyrosine kinase activity. Proc. Natl. Acad. Sci. USA *91*, 8132–8136. https://doi.org/10.1073/pnas.91.17.8132.

105. Singh, P.K., Kim, S., and Smith, A.W. (2024). HER4 is a high-affinity dimerization partner for all EGFR/HER/ErbB family proteins. Protein Sci. *33*, e5171. https://doi.org/10.1002/pro.5171.

106. Hanker, A.B., Brown, B.P., Meiler, J., Marín, A., Jayanthan, H.S., Ye, D., Lin, C.-C., Akamatsu, H., Lee, K.-M., Chatterjee, S., et al. (2021). Co-occurring gain-of-function mutations in *HER2* and *HER3* modulate HER2/HER3 activation, oncogenesis, and HER2 inhibitor sensitivity. Cancer Cell *39*, 1099–1114.e8. https://doi.org/10.1016/j.ccell.2021.06.001.

107. van Lengerich, B., Agnew, C., Puchner, E.M., Huang, B., and Jura, N. (2017). EGF and NRG induce phosphorylation of HER3/ERBB3 by EGFR using distinct oligomeric mechanisms. Proc. Natl. Acad. Sci. USA *114*, E2836–E2845. https://doi.org/10.1073/pnas.1617994114.

108. Freed, D.M., Bessman, N.J., Kiyatkin, A., Salazar-Cavazos, E., Byrne, P.O., Moore, J.O., Valley, C.C., Ferguson, K.M., Leahy, D.J., Lidke, D.S., et al. (2017). EGFR Ligands Differentially Stabilize Receptor Dimers to Specify Signaling Kinetics. Cell *171*, 683–695.e18. https://doi.org/10.1016/j.cell.2017.09.017.

109. Parres-Gold, J., Levine, M., Emert, B., Stuart, A., and Elowitz, M.B. (2025). Contextual computation by competitive protein dimerization networks. Cell *188*, 1984–2002.e17. https://doi.org/10.1016/j.cell.2025.01.036.

110. Arkhipov, A., Shan, Y., Kim, E.T., Dror, R.O., and Shaw, D.E. (2013). Her2 activation mechanism reflects evolutionary preservation of asymmetric ectodomain dimers in the human EGFR family. eLife *2*, e00708. https://doi.org/10.7554/eLife.00708.

111. Campbell, J.D., Alexandrov, A., Kim, J., Wala, J., Berger, A.H., Pedamallu, C.S., Shukla, S.A., Guo, G., Brooks, A.N., Murray, B.A., et al. (2016). Distinct patterns of somatic genome alterations in lung adenocarcinomas and squamous cell carcinomas. Nat. Genet. *48*, 607–616. https://doi.org/10.1038/ng.3564.

112. Collisson, E.A., Campbell, J.D., Brooks, A.N., Berger, A.H., Lee, W., Chmielecki, J., Beer, D.G., Cope, L., Creighton, C.J., and Danilova, L. (2014). Comprehensive molecular profiling of lung adenocarcinoma. Nature *511*, 543–550. https://doi.org/10.1038/nature13385.

113. Koboldt, D.C., Fulton, R.S., McLellan, M.D., Schmidt, H., Kalicki-Veizer, J., McMichael, J.F., Fulton, L.L., Dooling, D.J., Ding, L., and Mardis, E.R. (2012). Comprehensive molecular portraits of human breast tumours. Nature *490*, 61–70. https://doi.org/10.1038/nature11412.

114. Garner, A.P., Bialucha, C.U., Sprague, E.R., Garrett, J.T., Sheng, Q., Li, S., Sineshchekova, O., Saxena, P., Sutton, C.R., Chen, D., et al. (2013). An antibody that locks HER3 in the inactive conformation inhibits tumor growth driven by HER2 or neuregulin. Cancer Res. *73*, 6024–6035. https://doi.org/10.1158/0008-5472.CAN-13-1198.

115. Jia, Y., Yun, C.-H., Park, E., Ercan, D., Manuia, M., Juarez, J., Xu, C., Rhee, K., Chen, T., Zhang, H., et al. (2016). Overcoming EGFR(T790M) and EGFR(C797S) resistance with mutant-selective allosteric inhibitors. Nature *534*, 129–132. https://doi.org/10.1038/nature17960.

116. To, C., Beyett, T.S., Jang, J., Feng, W.W., Bahcall, M., Haikala, H.M., Shin, B.H., Heppner, D.E., Rana, J.K., Leeper, B.A., et al. (2022). An allosteric inhibitor against the therapy-resistant mutant forms of EGFR in non-small cell lung cancer. Nat. Cancer *3*, 402–417. https://doi.org/10.1038/s43018-022-00351-8.

117. Niu, Z., O'Farrell, A., Li, J., Reffsin, S., Jain, N., Dardani, I., Goyal, Y., and Raj, A. (2025). Piscis: A loss estimator of the F1 score enables accurate spot detection in fluorescence microscopy images via deep learning. Cell Syst. *16*, 101448. https://doi.org/10.1016/j.cels.2025.101448.

118. de Oliveira, L.R., and Jaqaman, K. (2019). FISIK: Framework for the Inference of In Situ Interaction Kinetics from Single-Molecule Imaging Data. Biophys. J. *117*, 1012–1028. https://doi.org/10.1016/j.bpj.2019.07.050.

119. Guerrero, J., Malik, Z., Bilal, F.N.U., Jana, S., Dasgupta, A., and Jaqaman, K. (2025). Inference of VEGFR2 dimerization kinetics on the cell surface by integrating single-molecule imaging and mathematical modeling. bioRxiv. 2025.06.03.657760. https://doi.org/10.1101/2025.06.03.657760.

120. Sakon, J.J., and Weninger, K.R. (2010). Detecting the conformation of individual proteins in live cells. Nat. Methods *7*, 203–205. https://doi.org/10.1038/nmeth.1421.

121. Sergé, A., Bertaux, N., Rigneault, H., and Marguet, D. (2008). Dynamic multiple-target tracing to probe spatiotemporal cartography of cell membranes. Nat. Methods *5*, 687–694. https://doi.org/10.1038/nmeth.1233.

122. Zhang, Y., Sun, P., Jiang, Y., Yu, D., Weng, F., Yuan, Z., Luo, P., Liu, W., and Wang, X. (2022). ByteTrack: Multi-object Tracking by Associating Every Detection Box. In Computer Vision – ECCV 2022, S. Avidan, G. Brostow, M. Cissé, G.M. Farinella, and T. Hassner, eds. (Springer Nature), pp. 1–21. https://doi.org/10.1007/978-3-031-20047-2_1.

123. Niu, Z., Bruyère, T., Manthey, D., Li, J., O'Farrell, A., and Raj, A. (2026). NimbusImage: a cloud-computing platform for image analysis. Nat. Methods *23*, 6–8. https://doi.org/10.1038/s41592-025-02942-6.

124. Michalet, X. (2010). Mean square displacement analysis of single-particle trajectories with localization error: Brownian motion in an isotropic medium. Phys. Rev. E Stat. Nonlin. Soft Matter Phys. *82*, 041914. https://doi.org/10.1103/PhysRevE.82.041914.

125. Jin, S., Haggie, P.M., and Verkman, A.S. (2007). Single-Particle Tracking of Membrane Protein Diffusion in a Potential: Simulation, Detection, and Application to Confined Diffusion of CFTR Cl− Channels. Biophys. J. *93*, 1079–1088. https://doi.org/10.1529/biophysj.106.102244.

126. Daumas, F., Destainville, N., Millot, C., Lopez, A., Dean, D., and Salomé, L. (2003). Confined Diffusion Without Fences of a G-Protein-Coupled Receptor as Revealed by Single Particle Tracking. Biophys. J. *84*, 356–366. https://doi.org/10.1016/S0006-3495(03)74856-5.

127. Kuno, M., Fromm, D.P., Hamann, H.F., Gallagher, A., and Nesbitt, D.J. (2001). "On"/"off" fluorescence intermittency of single semiconductor quantum dots. J. Chem. Phys. *115*, 1028–1040. https://doi.org/10.1063/1.1377883.

128. Wiesholler, L.M., Frenzel, F., Grauel, B., Würth, C., Resch-Genger, U., and Hirsch, T. (2019). Yb,Nd,Er-doped upconversion nanoparticles: 980 nm versus 808 nm excitation. Nanoscale *11*, 13440–13449. https://doi.org/10.1039/C9NR03127H.

129. Tuyen, V.T., Huy, B.Q.V., Tong, N.B., Ngoc Lam, T.T., Ferrari, M., My Dung, C.T., Dieu Thuy, U.T., and Van, T.T.T. (2023). Controllable structural and optical properties of NaYF4:Tm, Yb microparticles by Yb3+ doping for anti-counterfeiting. RSC Adv. *13*, 19317–19324. https://doi.org/10.1039/D3RA02841K.

130. Xiang, L., Chen, K., Yan, R., Li, W., and Xu, K. (2020). Single-molecule displacement mapping unveils nanoscale heterogeneities in intracellular diffusivity. Nat. Methods *17*, 524–530. https://doi.org/10.1038/s41592-020-0793-0.

131. Li, W., and Xu, K. (2025). Super-Resolution Mapping and Quantification of Molecular Diffusion via Single-Molecule Displacement/Diffusivity Mapping (SMdM). Acc. Chem. Res. *58*, 1224–1235. https://doi.org/10.1021/acs.accounts.4c00850.

STAR★METHODS

KEY RESOURCES TABLE

REAGENT or RESOURCE	SOURCE	IDENTIFIER
Antibodies		
Phospho-EGF Receptor (Tyr1068) Antibody	Cell Signaling Technology	Cat#: 2234; RRID: AB_331701
EGF Receptor (1F4) Mouse Monoclonal Antibody	Cell Signaling Technology	Cat#: 2239; RRID: AB_331373
Phospho-HER2/ErbB2 (Tyr1221/1222) (6B12) Monoclonal Antibody	Cell Signaling Technology	Cat#: 2243; RRID: AB_490899
HER2/ErbB2 (29D8) Rabbit Monoclonal Antibody	Cell Signaling Technology	Cat#: 2165; RRID: AB_10692490
HER3/ErbB3 (1B2E) Rabbit Monoclonal Antibody	Cell Signaling Technology	Cat#: 4754; RRID: AB_10691324
Phospho-MEK1/2 (Ser217/221) (41G9) Rabbit Monoclonal Antibody	Cell Signaling Technology	Cat#: 9154; RRID: AB_2138017
MEK1/2 (D1A5) Rabbit Monoclonal Antibody	Cell Signaling Technology	Cat#: 8727; RRID: AB_10829473
Phospho-p44/42 MAPK (Erk1/2) (Thr202/Tyr204) Mouse Monoclonal Antibody	Cell Signaling Technology	Cat#: 9106; RRID: AB_331768
p44/42 MAPK (Erk1/2) (137F5) Rabbit Monoclonal Antibody	Cell Signaling Technology	Cat#: 4695; RRID: AB_390779
Phospho-Akt (Ser473) (D9E) Rabbit Monoclonal Antibody	Cell Signaling Technology	Cat#: 4060; RRID: AB_2315049
Phospho-Akt (Thr308) (244F9) Rabbit Monoclonal Antibody	Cell Signaling Technology	Cat#: 4056; RRID: AB_331163
Akt (pan) (40D4) Mouse Monoclonal Antibody	Cell Signaling Technology	Cat#: 2920; RRID: AB_1147620
β-Actin (8H10D10) Mouse mAb	Cell Signaling Technology	Cat#: 3700; RRID: AB_2242334
Goat anti-Rabbit IgG (H+L) Secondary antibody, HRP	Invitrogen	Cat#: 32460; RRID: AB_1185567
Goat anti-Mouse IgG (H+L) Secondary antibody, HRP	Invitrogen	Cat#: 31430; RRID: AB_228307
EGFR Recombinant Rabbit Monoclonal Antibody (30H45L48)	Invitrogen	Cat#: 700308; RRID: AB_2532314
ErbB2 (HER-2) Monoclonal Antibody (3B5), Biotin	Invitrogen	Cat#: MA513672; RRID: AB_10982527
Phospho-ErbB3 (Tyr1197) Monoclonal Antibody (J.996.0)	Invitrogen	Cat#: MA514864; RRID: AB_10985249
Beta-Actin Antibody (HRP)	Novus	Cat#: NB600-532H; RRID: AB_1659873
Bacterial and virus strains		
DH5α	New England BioLabs	Cat#: C2987H
BL21(DE3) Competent *E. coli*	New England BioLabs	Cat#: C2521H
Chemicals, peptides, and recombinant proteins		
BG-Maleimide	New England BioLabs	Cat#: S9153S
MA(PEG)24 Methyl-PEG-Amine Compound	Thermo Scientific™	Cat#: 26114
Pierce™ SMCC	Thermo Scientific™	Cat#: 22360
IPTG	Invitrogen™	Cat#: 15529019
SH-PEG-NH_2.HCl	Biopharma PEG	Cat#: HE003005-1K
DMEM	Gibco™	Cat#: 11965092
RPMI 1640	Gibco™	Cat#: 11875093
Poly(maleic anhydride-alt-1-octadecene); M.W. ~ 30,000-50,000	VladaChem	Cat#: VL171000
Triethylamine	Sigma-Aldrich	Cat#: 471283
DMAP	Sigma-Aldrich	Cat#: 8510550100
N-(3-Dimethylaminopropyl)-N′-ethylcarbodiimide hydrochloride	Sigma-Aldrich	Cat#: 8009070001
N,*N*-Diisopropylethylamine	Sigma-Aldrich	Cat#: D125806
TSTU	Sigma-Aldrich	Cat#: 8512060025
Casein from bovine milk	Sigma-Aldrich	Cat#: 7078
1-(2-Aminoethyl)maleimide hydrochloride	Sigma-Aldrich	Cat#: 809322
Yttrium(III) acetate hydrate	Sigma-Aldrich	Cat#: 326064

(*Continued on next page*)

Continued

REAGENT or RESOURCE	SOURCE	IDENTIFIER
Ytterbium(III) acetate hydrate	Sigma-Aldrich	Cat#: 326046
Thullium(III) acetate hydrate	Sigma-Aldrich	Cat#: 367702
Erbium(III) acetate hydrate	Sigma-Aldrich	Cat#: 325570
Gadolinium(III) acetate hydrate	Sigma-Aldrich	Cat#: 325678
DMSO	Sigma-Aldrich	Cat#: D8418
DMF	Sigma-Aldrich	Cat#: 227056
Sodium Fluoride	Sigma-Aldrich	Cat#: S6776
Chloroform	Sigma-Aldrich	Cat#: 319988
Fetal Bovine Serum (FBS)	Sigma-Aldrich	Cat#: F2442
Sodium Trifluoroacetate	Sigma-Aldrich	Cat#: 132101
Oleic Acid	Sigma-Aldrich	Cat#: 364525
Octadecene	Sigma-Aldrich	Cat#: O806
Oleylamine	Sigma-Aldrich	Cat#: O7805
Ammonium Fluoride	Sigma-Aldrich	Cat#: 338869
Gelatin	Sigma-Aldrich	Cat#: G6650
Sodium Oleate	TCI America	Cat#: O0057
EveryBlot Blocking Buffer	Bio-Rad	Cat#: 12010020
HaloTag® Ligand Building Blocks Amine (O4)	Promega	Cat#: P6741
Gefitinib	MedChemExpress	Cat#: HY-50895
CLIP-tag ligand -COOH	Gift from Kai Johnsson Lab	N/A
Halotag7-mOrange	This work	N/A
Experimental models: Cell lines		
U2OS	ATCC	Cat#: HTB-96
HEK-293T	ATCC	Cat#: CRL-3216
A431	ATCC	Cat#: CRL-1555
PC9	Broad Institute Cancer Program	N/A
Critical commercial assays		
GeneJET Gel Extraction and DNA Cleanup Micro Kit	Life Technologies	Cat#: K0832
Gibson Assembly Master Mix	New England BioLabs	Cat#: E2611L
ECL Western Blotting Substrate	Life Technologies	Cat#: 32109
DNA Clean & Concentrator-5 (Capped) 200prep	ZYMO	Cat#: D4014
E.Z.N.A.® Endo-free Plasmid DNA Mini Kit	Thomas	Cat#: CHM02C984
QIAprep Spin Miniprep Kit	Qiagen	Cat#: 27104
Pierce™ BCA Protein Assay Kit	Thermo Scientific	Cat#: 23227
CellTiter 96® AQ_{ueous} One Solution Cell Proliferation Assay (MTS)	Promega	Cat#: G3582
Software and algorithms		
SnapGene	GSL Biotech LLC	https://www.snapgene.com/
Image J	National Institutes of Health	https://imagej.nih.gov/ij/
MATLAB	MathWorks	N/A
PRISM	GraphPad	N/A

METHOD DETAILS

Nanoparticle synthesis and functionalization

Core-shell nanoparticles were synthesized according to a previous method from the lab.[57] For the synthesis of the core, we mixed 2 mmol of Ln^{3+} acetate (Ln = Yb^{3+}/Er^{3+}/Tm^{3+}/Y^{3+}), 18.25 mL of oleic acid, and 20 mL of octadecene in a 250 mL three-neck round-bottom flask. The amount of Ln^{3+} acetate were weighed based on doping percentage. The mixture was heated under vacuum and at 100°C for 1 h. Then, 6.25 mmol sodium oleate, 10 mmol NH_4F, 6.25 mL oleylamine, and 8.75 mL octadecene were added and the mixture was stirred under vacuum at 25°C for 1 h. The mixture was then heated to 310°C for 50 min under N_2 flow, followed by rapid

cooling of the reaction. The core nanoparticles were precipitated and washed twice using ethanol with centrifuge at 3000× rcf for 5 min. Core nanoparticles were resuspended in 50 mL hexane with 100 μL oleic acid. For the shelling process, 2.7 mL of core nanoparticles were mixed with 4 mL oleic acid, 6 mL octadecene and vacuum was pulled to remove hexane at 70°C for 30 min. Then the mixture was heated to 290°C and held for 5 min under N_2 flow. Subsequently, five rounds of injection of shelling precursor were conducted with a 15 min interval between each round. The amount of precursor for each round was: 1. 0.54 mL of Y/Gd shelling precursor; 2. 0.27 mL of sodium trifluoroacetate (NaTFA) solution and 0.68 mL of Y/Gd shelling precursor; 3. 0.34 mL of NaTFA solution and 0.82 mL of Y/Gd shelling precursor; 4. 0.41 mL of NaTFA solution and 0.96 mL of Y/Gd shelling; 5. 0.48 mL of NaTFA solution. After the final injection, the reaction was kept at 290°C for 17 min, followed by rapid cooling and purification with the same process as purification of core nanoparticles. Specifically, for core nanoparticle of $NaTm_{0.1}Yb_{0.8}Y_{0.1}F_4$, only first three rounds of injection were conducted. The final core-shell nanoparticle was resuspended in 5 mL of hexane supplemented with 10 μL of oleic acid.

To prepare Y/Gd shelling precursor, 2 mmol of yttrium acetate, 0.5 mmol gadolinium acetate,10 mL of oleic acid and 15 mL of octadecene were first reacted under vacuum for at 110°C for 15 min. Then the reaction mixture was heated to 160°C and kept for 30 min under N_2 flow. Then the mixture was cooled to 110°C and vacuum was pulled once more, followed by cooling to room temperature.

To prepare NaTFA solution, 6 mmol of sodium trifluoroacetate was mixed with 15 mL oleic acid under vacuum. The mixture was heated to and kept at 50°C until sodium trifluoroacetate was fully dissolved.

To functionalize the nanoparticles, 1 mL of as-prepared core-shell nanoparticles was dried under vacuum at room temperature followed by addition of 150 mg Poly(maleic anhydride-alt-1-octadecene (PMAO) dissolved in 7 mL chloroform. The mixed solution was stirred at room temperature for 1.5 h and then chloroform was evaporated under vacuum at room temperature. The residue was sonicated and re-dispersed in 10 mL of 100 mM NaF solution containing 150 mg DMAP. The whole solution was centrifuged at 32,000x rcf for 2 hours and washed once with 100 mM NaF solution to remove excessive PMAO and DMAP. The PMAO-coated nanoparticles were dispersed in 3 mL 1xPBS supplemented with 100 mM NaF. For ligand conjugation, 1.5 mL of PMAO-coated nanoparticles was mixed with 6 μl of 350 mM MA(PEG)24 Methyl-PEG-amine Compound and 8 μl of 8 mM X-PEG-Amine (X = HaloTag ligand, SNAP tag ligand or CLIP tag ligand) under magnetic stirring. Then 30 mg EDC dissolved in 100 μl 1xPBS was added and the mixture was stirred for 2 h. 30 mg EDC and 6 μl of 350 mM Methyl-PEG-Amine were added again and reacted for another 2 h. The solution was centrifuged at 20,000x rcf for 2 h. The supernatant containing mono-disperse ligand-conjugated nanoparticles was concentrated and washed with am Amicon 100kDa centrifugal filter.

The HTL-PEG-Amine was obtained by a two-step reaction. First, 150 μl of 10 mM HaloTag® Ligand Building Blocks Amine (O4) dissolved in anhydrous DMF was mixed with 15 μl of 100 mM SMCC dissolved in anhydrous DMF and 1 μl triethylamine. The mixture was reacted overnight at 37 °C followed by addition of 10 μl of 150 mM SH-PEG-NH_2 dissolved in anhydrous DMF. The mixture was kept at room temperature for 10 h and stored at -20 °C. The STL-PEG-Amine was obtained by mixing 150 μl 10 mM BG-maleimide and 10 μl of 150 mM SH-PEG-NH_2 dissolved in anhydrous DMF, supplemented with 1 μl triethylamine. The CTL-PEG-Amine was obtained by a two-step reaction as well. First, the 100 μl of 20 mM of CTL-COOH in anhydrous DMSO was activated with 3.5 μl DIPEA and 10 μl of 200 mM TSTU dissolved in anhydrous DMSO for 30 min. Then 10 μl of 200 mM 1-(2-aminoethyl)maleimide hydrochloride in anhydrous DMSO was added and reacted for 3 h. 10 μl of 200 mM SH-PEG-NH_2 in anhydrous DMF was added and the mixture was kept at room temperature for 10 h and stored at -20 °C. Finally, the concentration of X-PEG-Amine was adjusted to 8 mM using anhydrous DMF.

Nanoparticle Size Analysis

All the synthesized nanoparticles were imaged with FEI Tecnai (G2 Spirit TWIN) Transmission Electron Microscope (TEM) operated at 120 kV. The size distribution of each sample was analyzed by a customized MATLAB code that measures the diameter of nanoparticles with a minimum number of 500 nanoparticles. The mean value and standard deviation were then calculated by fitting the data to a gaussian distribution.

Dynamic light scattering measurement

Dynamic light scattering (DLS) measurement was performed with Wyatt DynaPro™ NanoStar™. Functionalized UCNPs were diluted 10 times, with a final concentration of ∼5 nM, in 10× PBS for the measurement.

Zeta potential measurement

Zeta potential measurement was performed with Malvern Zetasizer Advanced Pro using DTS1070 folded capillary cuvettes. Functionalized UCNPs were diluted 10 times, with a final concentration of ∼5nM, in water for the measurement.

Microscope Setup

The microscope carried two diode lasers, a Thorlabs 976 nm fiber coupled laser (P.N. BL976-PAG900) and a Cobolt 638 nm free-space laser (P.N. 06-MLD). The 976 nm laser was reflected by a 950 nm dichroic into an upright Nikon 60× oil objective (N.A. 1.49) atop which the sample was mounted. There was a motorized mirror which could displace the irradiation beam such that it hit the back optical port of the objective offset from the central axis. This allowed for reversible switching between epifluorescence and Total-internal-reflection fluorescence (TIRF) illumination modes. The TIRF penetration depth was calculated to about 150 nm and allowed for a reduced background from off-focal plane emission. Samples were able to be irradiated with power densities between 1

and 30 kW/cm^2. The emission was captured by the objective and passed through the 950 nm dichroic into the emission pathway. The image was focused by a 400 mm tube lens, through a 950 nm shortpass filter. The emission passed through an iris and then into a dark box where it was successively split into four channels by three dichroics at 510 nm, at 610 nm and at 705 nm. The individual channel emissions were steered by independent mirrors toward another symmetric trio of dichroics which re-joined them. In each individual channel was a 255 mm collimating lens. Before hitting the camera, the emission was focused by a 300 mm lens for an overall image with each pixel corresponding to 100 nm. Each emission was steered to occupy one corner of the camera detector, and the iris was sized to ensure no bleed over between quadrants.

The 638 nm laser was steered into a micromirror assembly below the backport of the objective which did not significantly occlude the emission image. It was angled such that it totally internally reflected on the sample and was collected by the objective. The outgoing beam was focused onto a quadrant photodetector and allowed for the correction of stage z-drift. This allowed for focus to be maintained at the same level during long imaging sessions. The illumination of the microscope can be changed between epi-illumination and TIRF illumination.

The sample mount was surrounded by an incubating enclosure which allowed control of the local atmosphere. Unless otherwise noted, conditions were kept at 37.0°C and 5% CO_2 for all cell experiments. No significant heating effects from the excitation laser were found. If the sample was heating up from the laser, the temperature gain was corrected by the incubating chamber's temperature feedback loop.

Single-UCNP brightness measurement

Procedures for measuring UCNP brightness have been described previously.[57] Approximately 400 ng/mL UCNPs in hexane were drop cast onto a clean and dry no. 1.5 cover glass pre-coated with 1% (w/v) poly-L-lysine. Hexane was used to rinse off excess nanoparticles. For rigid support, the cover glass was attached to a standard microscope slide using double-sided tape after particles were left to dry for 5 min. Single particle optical characterization was performed using the home-built microscope described with epi-illumination. Custom Python-based code was used to identify single point-spread functions for each particle and perform a 2D gaussian fit to determine the particle emission in units of photons per second (pps). Only point-spread functions located in the center 128 pixel × 128 pixel region of the camera field-of-view were registered and analyzed to account for the gaussian falloff of the beam near the edges of the field-of-view.

Measurement of number of ligands on UCNP-HTL

The coding sequence of Halotag7 was fused N-terminally to mOrange (HaloTag-mOrange) and cloned into pET expression vector with a N-terminal 6xHistag and a TEV cleavage site. The plasmid was transformed into *E. coli* BL21(DE3) cells (NEB C2527) and the bacteria were grown in 1 L of LB medium with 100 μg/mL ampicillin. 500 μM IPTG was added when optical density (OD600) reached 0.6 and bacteria were incubated overnight at 25°C. Bacteria were harvested by centrifugation at 5,000× rcf for 20 min and resuspended in lysis buffer. Lysis buffer was composed of 50 mM Tris-HCl pH = 8, 500 mM NaCl, 5% glycerol and 20 mM imidazole, supplemented with 1 μL Bezonase, 1 mM $MgCl_2$ and protease inhibitor per 10 mL. Cells were lysed by ultrasonication, and supernatant was collected by centrifugation at 20,000× rcf for 20 min. Proteins were collected by NEBExpress® Ni Spin Columns (NEB #S1427) and were aliquoted and stored at -80°C.

5 nM of Er10Yb90-HTL and Tm06Yb94-HTL were mixed with 1 μM of HaloTag-mOrange and incubated overnight. UCNP-HTL conjugated with HaloTag-mOrange was washed by centrifugation at 21,000x rcf, 2h for four times to remove free HaloTag-mOrange. The product was diluted and dropped onto a coverslip for imaging. Snapshots of Er10Yb90-HTL and Tm06Yb94-HTL were captured with 976 nm laser excitation. Videos of the bleaching of mOrange were captured with 532 nm laser excitation. The maximum intensity projection of the time lapse videos was used to assess the colocation with UCNP signal.

Confirmation of lack of interactions between the three ligand-conjugated UCNPs

Er10Yb90-HTL, Tm10Yb80-STL and Tm02Yb30-CTL were mixed at equal concentration (~100 nM) and incubated overnight. The mixture was then diluted for single-particle imaging with 976 nm laser excitation.

Experimental Model and Study Participant Details

U2OS and HEK293T were cultured in Dulbecco's Modified Eagle Medium (DMEM) (Life Technologies) supplemented with 10% fetal bovine serum (FBS, Sigma F2442) and 1× penicillin/streptomycin (Life Technologies). PC9 and A431 cells were maintained in RPMI 1640 medium (Corning) supplemented with 10% FBS and 1× penicillin/streptomycin. A431 cells (CRL-1555) were also purchased from ATCC. All cells were cultured at 37 °C with 5% CO_2. Cells were dissociated using 0.05% Trypsin-EDTA (Life Technologies) at a split ratio of 1:3 to 1:6 every 3–6 days. Mycoplasma contamination was routinely monitored to ensure cell culture quality. There were no animal or human participants for any study or experiment in this work.

Plasmid construction and lentivirus preparation

Primers were ordered from IDT. CLIP-tag2's sequence was obtained from Kai Johnsson's group who kindly provided us the plasmid with the coding sequence. For transient expression plasmids, HaloTag7, SNAP-tag2, or CLIP-tag2 fragments, along with the targeted genes, were cloned into the pcDNA3.1 vector, separated by a 13-amino acid linker. For lentiviral plasmids, HaloTag7 and

EGFR fragments were cloned into pSin vectors. All constructs were verified by nanopore sequencing from Plasmidsaurus Inc. The detailed sequences of all the fusion proteins were listed in Table S1. In this study, all the tags are located at the N-terminus of the receptor.

To prepare lentiviruses, plasmids were transfected into HEK293T cells using Lipo3000 (Life Technologies) in Opti-MEM medium (Life Technologies). After 6 hours, the medium was replaced with regular cell culture medium. Lentiviruses were harvested and filtered at 48 and 72 hours post-transfection. For lentiviral infection, U2OS cells at 60%–70% confluency were incubated with the viruses for 4 hours, followed by selection with 1 μg/mL puromycin (Life Technologies) for 3–5 days.

Validation of non-perturbing effect of HaloTag7 fusion on EGFR

PC9 cells expressing Halo-EGFR-L858R/T790M were generated by lentiviral infection. After selection, 2,000 cells were plated in each well of a 96-well plate. After 24 hours, cells were treated with increasing amounts of gefitinib at half log increase. 96-hours post treatment, cell viability was determined using an MTS assay (Promega- CellTiter 96® AQueous One Solution Cell Proliferation Assay, G3580) according to manufacturer instructions.

Western blotting

Total protein was extracted from cells by incubating them on ice for 30 minutes with RIPA lysis buffer (Life Technologies) supplemented with 1× protease and Phosphatase Inhibitor (Life Technologies). Cell lysates were centrifuged at 14,000 × g for 15 minutes, and the supernatants were collected. Protein concentration was quantified with BCA assay using Pierce™ BCA Protein Assay Kit. Proteins were resolved on 4%–20% Mini-PROTEAN® TGX™ Precast Protein Gels (Bio-Rad) and transferred onto 0.2 μm nitrocellulose membranes using nitrocellulose Transfer Packs (Bio-Rad). Membranes were blocked with 5% non-fat milk (Bio-Rad) in Tris-buffered saline containing 0.1% Tween 20 (TBST) for 1 hour (Figures S3C and S3D) or with EveryBlot Blocking buffer for 5 min at room temperature (Figure S3E). After blocking, membranes were incubated with primary and secondary antibodies as specified in the Key Resources, followed by detection using the ECL Western blotting Substrate (Life Technologies).

Live-cell imaging

For the transient expression system, plasmids were transfected into U2OS cells using Lipo3000 (Life Technologies) in Opti-MEM medium (Life Technologies). After 6–8 hours, the cells were re-seeded on the ibidi μ-slide 18-well with glass bottom (Cat.81817). Prior to seeding the cells, the surface was coated with 0.2%(w/v) gelatin solution for 30 min under room temperature. To perform dye labeling, Halotag-TMR, SNAP-Cell 647-SiR or CLIP-Cell TMR-Star were added at 1 μM in DMEM for 5 min. Excessive dyes were wash by DMEM. To perform UCNP binding to live cells, cells were blocked in 1% casein (Sigma, C5890) in DMEM for 5 minutes. Subsequently, ∼ 1 nM of UCNPs (diluted in DMEM containing 1% casein) were added, and cells were incubated at 37 °C with 5% CO_2 for 5 minutes. Before imaging, unbound UCNPs were removed by washing with DMEM containing 1% casein. Two-color live-cell imaging was performed under TIRF illumination, for 2–16 minutes at a time resolution of 100 ms at 37 °C and a power density of 21 kW/cm^2. Three-color live-cell imaging was performed under a power density of 4.2 kW/cm^2 to ensure robust signal differentiation between Tm10Yb90-STL and Tm02Yb30-CTL. The focal plane was set to the bottom of the cell membrane and maintained throughout the experiment. Each well of cells was imaged no longer than 40 minutes after staining.

Single-particle tracking analysis

Point-spread function (PSF) localization and tracking were performed using the a customed MATLAB scripts, SLIMfast2, performing 2D Gaussian fitting with the multiple-targeting tracing method.[121] Localization parameters were kept constant between videos and conditions and can be found in Data S1; page 2, except the *Intensity Threshold* parameter which was changed on a case-by case basis to account for varying background levels so that the algorithm picked all the PSFs. We calculated the localization precision σ_{loc}, in live-cell videos using the number of collected photons:

$$\sigma_{loc} = \frac{\sigma_{psf}}{\sqrt{N_{photons}}}$$

where σ_{psf} is the standard deviation of a gaussian fit to the point-spread-function. This value agreed with the theoretical standard deviation, $\sigma_{psf} = \frac{0.61 \cdot \lambda}{2NA}$. The localization precision was found to be 6.7 nm and 6.9 nm for Er10Yb90 and Tm06Yb94 UCNPs, respectively.

Trajectory generation parameters were kept the same between videos, notably, the maximum diffusion coefficient SLIMfast2 considered was set at 1 $\mu m^2/s$. This minimized any nearby trajectories switching IDs when they came close together. Although accurate, SLIMfast2 sometimes lost trajectories of particles due to PSF merging or off-focus movement.

In addition to SLIMfast2, we developed a novel single-particle tracking (SPT) method by combining Piscis,[117] a deep learning algorithm for spot detection and localization, and ByteTrack,[122] a Kalman filter-based algorithm for multi-object tracking. While the pretrained Piscis model performed well at detecting and localizing our UCNPs, we further enhanced model performance by training a custom model using NimbusImage,[123] a cloud-computing platform for image analysis that supports human-in-the-loop finetuning. Specifically, we ran the pretrained Piscis model on experimental UCNP images, manually corrected the resulting annotations by

adding missed particles and removing false positives, and then finetuned Piscis using these curated labels. A comparison between these two methods showed that Piscis generated less trajectory interruptions in crowded areas. We also manually inspected and corrected the trajectories.

Using both SLIMfast2 and Piscis, we obtained a list of particle IDs and their trajectories for further analysis. Output from SLIMfast2 was used for the diffusion coefficient analysis, while output from Piscis was used for the dimerization analysis.

Diffusion modes and coefficients analysis

We modeled each receptor movement as a hidden Markov model (HMM) and used a Bayesian inference algorithm[75] to identify its parameters. This method is particularly suited for analyzing long trajectories to extract dynamic information.

We assumed the receptors imaged through UCNPs were moving on the membrane of the cell with 2D diffusion. A diffusion mode is characterized by the diffusion coefficient (D), and a transport coefficient (μ). The steps for each time interval (Δt) in each dimension (x, y) are distributed based on a Gaussian distribution:

$$\Delta x \propto \frac{1}{(4\pi D\Delta t)^{3/2}} e^{-\frac{(x-\mu)^2}{4D\Delta t}}$$

Many trajectories exhibit more than one diffusional mode (i.e. modes with different parameters). Therefore, we find both the parameters (D, μ) for the modes and the transition probabilities (P_{ij}) between modes. Every timestep in the trajectory was assigned a particular mode. Figures S4A–S4D show the analysis scheme and an example trajectory.

We implemented the algorithm described in Ref. [75] and adapted it for parallel GPU HPC to accommodate the high number and long length of trajectories our single particle tracking method yields. Computations were run locally on a Nvidia RTX 4070 GPU, and in Lincoln Lab's Supercloud cluster using a Nvidia Volta V100 GPU.

The Bayesian HMM algorithm evaluates multiple models for each trajectory and assigns probabilities to each. In this study, we limited the analysis to combinations of up to three diffusional (D) and with or without transport (V) modes, resulting in nine possible models:

- **D**; Trajectories found to have only one diffusion mode, with one diffusion coefficient.
- **DV**; Trajectories found to have one diffusion mode with one diffusion coefficient and a transport velocity vector.
- **D, D**; Trajectories found to have two diffusion modes, with the receptor switching between two modes during the trajectory length.
- **D, DV**; Trajectories found to have two diffusion modes, with the receptor switching between two modes during the trajectory length. One of the modes also has a transport velocity vector.
- **DV, DV**; Trajectories found to have two diffusion modes, with the receptor switching between two modes during the trajectory length. Both of the modes also have a transport velocity vector.
- **D, D, D**; Trajectories found to have three diffusion modes, with the receptor switching between the three modes during the trajectory length.
- **D, D, DV**; Trajectories found to have three diffusion modes, with the receptor switching between the three modes during the trajectory length. One of the modes also has a transport velocity vector.
- **D, DV, DV**; Trajectories found to have three diffusion modes, with the receptor switching between the three modes during the trajectory length. Two of the modes also have a transport velocity vector.
- **DV, DV, DV**: Trajectories found to have three diffusion modes, with the receptor switching between the three modes during the trajectory length. All of the modes also have a transport velocity vector.

We include transport modes because we occasionally observe motions that do not conform to pure diffusion and are directional in nature. We believe some of those are endocytosed receptors transported close to the basal membrane (hence their PSFs stay in focus). Allowing some modes to have a transport velocity vector in addition to the diffusion behavior is a refinement to the underlying model assumption that ensured the diffusion coefficients found by the Bayesian algorithm are accurate.[75]

While some longer trajectories may contain more than three dynamic states, expanding the model space would increase computational cost and risk overfitting. Given our large dataset, comprising hundreds of thousands of trajectories across experimental conditions, we analyzed only the first 500 frames of each trajectory to ensure timely completion of the analysis. Further optimization of the computational pipeline will allow for the incorporation of additional dynamic states and full-length trajectory analysis. To determine how truncation of a trajectory affects the resulting distribution of modes and diffusion coefficients, we created 500 subsets of the trajectory shown in Figure 3 composed of 500 frames each (50 seconds). Each trajectory was shifted from the previous by one frame, and all included the midpoint (Figures S4E–S4G). HMM analysis on all 500 truncated trajectories showed that only one of them did not yield a 2-mode distribution like that of the original entire trajectory. The final distribution of diffusion coefficients is consistent with the one found from analyzing the entire trajectory. Furthermore, the assigned diffusion coefficient or the midpoint was always found to be similar ($\sim$0.006 $\mu m^2/s$), within the error of the coefficient distribution. Also, it was always the slower of the two coefficients found, as in the original trajectory.

The Bayesian HMM algorithm yields the most likely hidden Markov model for every trajectory that would describe that trajectory, as well as the mode at each step. For each experimental condition, we pooled the most likely model for each trajectory across all the cells. To illustrate the full scope of the data we obtain from this analysis, we plotted all outputs of the EGFR WT condition in Data S1; page 4. It shows distribution of different models, distribution of diffusion coefficients from the top two or three models (such as 1-diffusion mode and two-diffusion mode), and the total distribution of diffusion coefficients by aggregating diffusion coefficients from the best model of each trajectory.

We also analyzed dimer trajectories individually to test if there was any correlation between diffusion coefficient or mode, and dimerization state. We found both monomer and dimer receptors exhibited heterogeneous behaviors, and that the diffusion coefficient is not a reliable metric to assign the oligomeric state (Figures S5A–S5F).

We performed single-particle tracking of WT-EGFR using dyes and put the resulting trajectories through the same analysis pipeline to compare our results to literature methods. The resulting diffusion coefficient distribution (Figure S4K) is consistent with the distribution obtained using UCNPs. Data S1; page 1 summarizes the dataset used to generate the diffusion coefficient histograms for all conditions.

The different modes obtained from the HMM analysis represent distinct physical states of EGFR mobility on the plasma membrane, which could reflect interactions with the cellular environment. For instance, free diffusion (D mode) likely corresponds to unbound or minimally interacting receptors, while directed motion (DV mode) may arise from cytoskeletal transport or clustering. Such mapping could reveal key aspects of EGFR signaling. However, precise determination of the corresponding biological states requires systematic investigation, including co-staining of multiple other proteins and subcellular organelles, which is beyond the scope of this paper. We therefore refrain from making direct biological claims from the diffusion model distribution generated by the HMM analysis and instead focus more on the pooled diffusion coefficient histograms. Nevertheless, we believe the cellular environment has a substantial impact on receptor diffusion modes and coefficients, and a detailed study of receptor movement in conjunction with the diffusion heatmaps shown in Figure S4M represents one of our future research directions.

MSD analysis

Mean-square displacement (MSD) has been extensively used in single-particle tracking to extract the diffusion coefficient of trajectories.[76,124–126] We performed MSD analysis of our data to illustrate how diffusion of membrane receptors is not accurately captured by such analysis. MSD diffusion coefficients were obtained by utilizing a window of 6 frames and fitting the first 5 frames of the resulting MSD plot to obtain the final diffusion coefficient. An increase in window frames only increased the spread of the resulting distribution, as well as poorer fit qualities. Likewise for an increase in the fitting frame number. Only fits better than a threshold R-squared (> 0.85) were accepted.

Calculating diffusion from an MSD plot assumes that the movement of a receptor is characterized by one single diffusional parameter. While this often true for small trajectories ($t < 1s$), we found from the HMM analysis that the average lifetime of a diffusional mode for EGFR is (0.70 ± 0.02) seconds, and so an MSD analysis of trajectories longer than this will likely violate the 1-mode assumption. Furthermore, this model does not account for transport, only random diffusion, any trajectories, which contain transport behavior will result in incorrect diffusion coefficients using the MSD analysis.

We have also simulated perfectly ideal diffusion trajectories with two modes and parameters drawn from our experimental distribution to ascertain the systematic error of the HMM analysis and the MSD analysis. Figures S4H and S4I shows the simulated distributions and the results of both analysis methods. The separate mode peaks for the MSD results get averaged out, whereas the HMM results show the peaks independently, with a σ/μ of 10%.

We utilized custom Python code to obtain MSD histograms of the same data on which we performed the HMM analysis. Figure S4J shows that while the slow-down phenotype between WT-EGFR with and without 100 nM EGF is similar, the magnitude and numerical mean are different, highlighting the inaccuracy of MSD analysis over longer trajectories.

Motion blur error analysis

To estimate localization error due to the motion blur of particles, we used $D = 0.01\ \mu m^2/s$ as the diffusion coefficient, and found the motion blur based on the following formula:

$$\sigma_{MB} = \sqrt{\frac{D \cdot \Delta t}{3}} = 18.3\ nm$$

where $\Delta t = 0.1\ s$ is the exposure time. This yields a σ_{MB} of 18.3 nm. The chosen diffusion coefficient is conservative being on the higher end of the distributions found through the HMM analysis.

Image registration and error analysis

Image registration between the four different channels was done using UCNPs with emission in all four channels, imaged at long exposure as in ref. [57] with custom python code. Separate channels were coarsely aligned on the camera with independent steering mirrors. Fine registration was done by selecting and resolving point-spread functions present in all four channels to produce transformation matrices between channels. The transformation matrix was then applied to every image and video. Registration error for

mapping the NIR channel (for imaging Tm06Yb94) to the Red channel (for imaging Er10Yb90) was found to be σ_{Reg} = 16 nm (Figure S4O).

Dimer lifetime analysis

Dimers formed between receptors labeled with different colors of UCNPs were identified by custom code based on the proximity of their reconstructed trajectories from Piscis. We set a proximity threshold of 125 nm for at least 5 frames (0.5 s) to determine colocalization. This distance threshold was determined based on: (1) Localization precision, $\sigma_{loc} \sim 6.8\ nm$; (2) Motion blur, $\sigma_{MB} \sim 18.3\ nm$; (3) Registration error, σ_{Reg} = 16 nm; and (4) Physical separation of the two UCNPs on two receptors.

We then estimated the theoretical center-to-center distance between two UCNPs labeling an EGFR dimer. Based on PDB crystal structure of EGFR dimer activated by EGF (PDB: 1IVO),[16] the distance between the two EGFR N-termini is ~4.7 nm. On each monomer, this is extended by a ~5 nm glycine linker, the ~5 nm HaloTag protein (33 kDa), and a ~5 nm PEG linker connecting to the UCNP (~8.5 nm radius). Summing up these for the full dimer complex (illustrated in Figure S4Q):

$$\mu_{EGFR} = 4.7\ \text{nm} + 2 \times (5\ \text{nm linker} + 5\ \text{nm HaloTag} + 5\ \text{nm PEG} + 8.5\ \text{nm UCNP Radius}) = 51.7\ nm$$

We then accounted for experimental uncertainties (localization for each channel, motion blur, registration), which combine in quadrature to be

$$\sigma_{Total} = \sqrt{\sigma_{loc\ 1}^2 + \sigma_{loc\ 2}^2 + 2\sigma_{MB}^2 + \sigma_{reg}^2} =$$

$$= \sqrt{(6.7\ nm)^2 + (6.9\ nm)^2 + 2(18.3\ nm)^2 + (16.2\ nm)^2} = 32\ nm.$$

Considering ~3 standard deviations from the mean, this yields a maximal statistical threshold of ~148 nm [51.7 nm + 3 × 32 nm]. To minimize false positives, we lowered the threshold to 125 nm.

For these selected dimers, we account for stochastic variations by tolerating frames where the inter-receptor distance goes above the threshold for up to 8 frames but remains below a maximum of 200 nm. Likewise, we do not assign a dimer when the distance between two molecules occasionally dips below the threshold for shorter than 8 frames. Furthermore, we excluded any dimers that form within the first 5 frames or dissociate within the last 5 frames of each video. This additional filtering step ensures that the measured dimer lifetimes reflect their complete duration, preventing any underestimation due to video-length constraints. The minimum dimer lifetime resolution was set by the exposure time, 100 ms. We obtained a list of dimer lifetimes aggregated from several cells for each experimental condition. Data S2; **page 1** shows the histograms of dimer lifetime for each condition.

We use the data to calculate the Probability Distribution Function for each condition. Let $\{b_i\}$ denote the histogram bin edges with bin width equal to dt = 0.1 s (the exposure time of all data taken). The number of occurrences in each bin is H_i, and the total number of counts is $\sum H_i$. The probability-mass-function (PMF) is given by:

$$X_t = \frac{H_i}{\sum H_i}$$

representing the proportion of data points in each bin. The bin center is defined as:

$$t_i = \frac{b_i + b_{i+1}}{2}$$

To obtain a smooth and reliable estimate of the probability distribution while minimizing artifacts arising from the finite time duration of the recorded video, we calculate the probability density function (PDF) by weighting each time point in the probability mass function histogram by the average interval between its adjacent events.[127]

To obtain a comparable metric between conditions for dimerization, we fit the dimer lifetime PDF distribution to a Power Law distribution:

$$PDF(\tau) = (\alpha - 1) \cdot {t_{min}}^{\alpha - 1} \tau^{-\alpha}$$

where t_{min} is set to 1.5 s. We found this to be a reasonable starting point since it is highly unlikely a random overlap of non-dimerizing receptors will last longer than this threshold. To test this assumption, we simulated pure diffusional behavior based on the distribution of diffusion coefficients for EGFR+EGF found through the hidden Markov model analysis. The simulated video had no hard-coded dimerization, and the transient colocalization events existed only stochastically. Figure S5G–S5I show the results of the cell experiments versus the diffusion simulation. Only 1% of colocalizations in the simulation were longer than 1.5 seconds. Fitting the data to a power law allows us to calculate a power law factor α to quantify the phenotypes between WT and mutant or stimulated receptor proteins. Table 1 shows the α parameter found for each condition. Since a multiplying factor does not change the slope of the power laws, we normalize the PDF to its first datapoint before fitting. We do not use the scaling parameter obtained from the fit, as that does change with normalization. Calculation of the error on the fit parameters is done through the covariance matrix. The fitting strategy relied on minimization of log-residuals since the absolute value of the PDF at large lifetimes was much smaller than that at low life-

times, and so did the residuals. Minimizing the log-residuals ensured accurate power law behavior at the tail, which contained many fewer datapoints than the start of the curve due to the behavior of the power law. We also constrained the fit to the first point, such that all fit curves emerged from the normalized value of 1 at t = t_{min}.

We use α to calculate the time at which 99% of all dimers will have dissociated, denoted $\tau_{99\%}$:

$$\tau_{99\%} = t_{min} \cdot (1 - 0.99)^{\frac{1}{1-\alpha}}$$

Figure S5J shows a scheme for the data analysis pipeline for dimerization parameters. Table 1 contains the power law factor α, its standard error calculated from the fit, the $\tau_{99\%}$ derived from it, its standard error from the full dataset fit, and the R^2 values for each of the fits. To calculate significance between the $\tau_{99\%}$ of different conditions, we evaluate the error on the fit parameter using bootstrapping. For each condition with n datapoints after t = 1.5 s, we sample n points with replacement and perform the power-law fit to obtain α, and $\tau_{99\%}$. We do this for N = 10000 bootstraps and obtain the error on the estimate of $\tau_{99\%}$. The bootstrapping means and errors can be found in Table 1. The $\tau_{99\%}$ comparison violin plots equivalent to those shown in Figure 4, Figure 5 and Figure 6 for the bootstrapping results can be found in Figure S5K, with the estimated significance between the fit parameters of different conditions annotated. Significance was calculated using z-scores between bootstrapping parameters.

We further investigated whether the total percentage of dimerized receptors changed between mutants. We defined ρ (rho) as the average percentage of labeled receptors that are dimerizing at any given time:

$$\rho = \sum \frac{2 \cdot d_i}{F \cdot N_i}$$

where the summation is over all measured frames of the video {i}, F is the total number of frames, N_i is the number of receptors in each frame and d_i is the number of dimers in each frame. The factor of 2 means we recognize there are 2 receptors per dimer. We calculated ρ for each cell and obtained an average over all cells for each condition (as well as the standard error). The values for ρ and its standard error for each condition can be found in Table 1; in Figure S5L, plotted against the $\tau_{99\%}$.

QUANTIFICATION AND STATISTICAL ANALYSIS

All fit parameters have been provided with their standard errors and are reported as mean ± SEM unless described otherwise in the text or figure caption. Statistics, error estimates and control simulations for each analysis are described in their respective sections. All analysis was performed using python and MATLAB. The notation for statistical significance is as follows: * represents $p < 0.05$, ** represents $p < 0.01$ and *** represents $p < 0.001$.

Supplemental figures

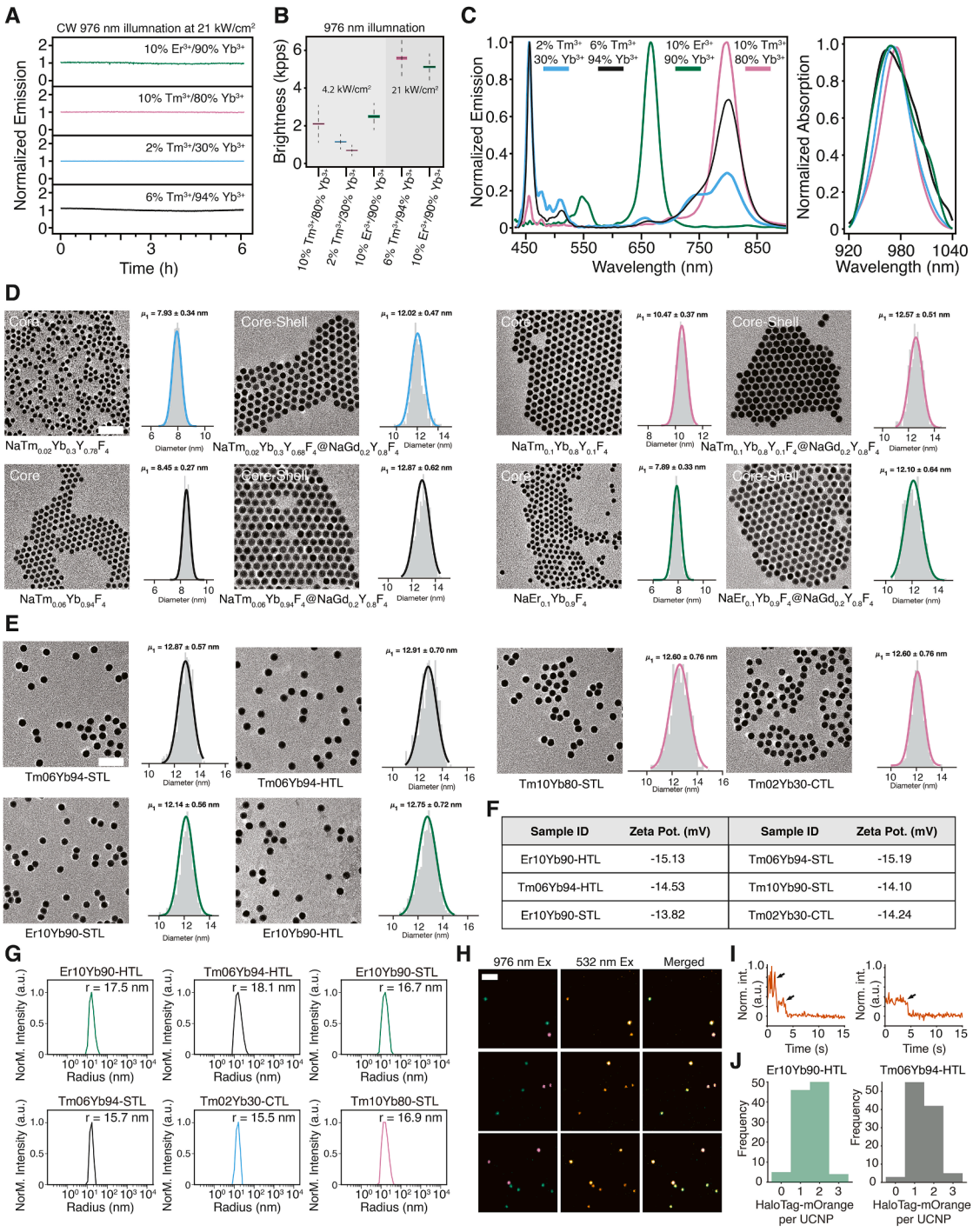

Sample ID	Zeta Pot. (mV)	Sample ID	Zeta Pot. (mV)
Er10Yb90-HTL	-15.13	Tm06Yb94-STL	-15.19
Tm06Yb94-HTL	-14.53	Tm10Yb90-STL	-14.10
Er10Yb90-STL	-13.82	Tm02Yb30-CTL	-14.24

Figure S1. UCNP characterization, related to Figures 1 and 2

(A) Stability measurement of normalized probe brightness over the time scales of hours.

(B) Brightness under imaging conditions for the three probes for 3-color tracking and the probes for 2-color tracking. Magenta indicates emission between 705 and 850 nm, blue indicates emission below 510 nm, and green indicates emission between 610 nm and 705 nm. Dashed lines indicate ±1 standard deviation from the mean.

(legend continued on next page)

(C) Emission (left) and absorption (right) spectra of the four UCNPs used in this work, with emission normalized to the highest peak. The absorption spectra matched well with previously reported results on UCNP that used Yb^{3+} as a sensitizer.[128,129]
(D) TEM images of core and core-shell UCNPs. Scale bars, 50 nm.
(E) TEM images of ligand-conjugated UCNPs. Scale bars, 50 nm.
(F) Zeta potential of ligand-conjugated UCNPs. Measurement was conducted in DI water.
(G) DLS of ligand-conjugated UCNPs. Measurement was conducted in 1× PBS.
(H) Measurement of the number of HTL on HTL-conjugated UCNP through colocalization of Er10Yb90-HTL (green), Tm06Yb94-HTL (magenta), and HaloTag7-mOrange (orange). Scale bars, 2 μm.
(I) Two-step and one-step bleaching traces of HaloTag-mOrange on HTL-conjugated UCNP.
(J) Quantification of the number of HaloTag-mOrange per UCNP. We mixed HTL-conjugated UCNPs with an excessive concentration of purified HaloTag-mOrange protein, ensuring a close to 100% labeling efficiency. Therefore, the number of HaloTag-mOrange is approximately the number of HTL per UCNP.

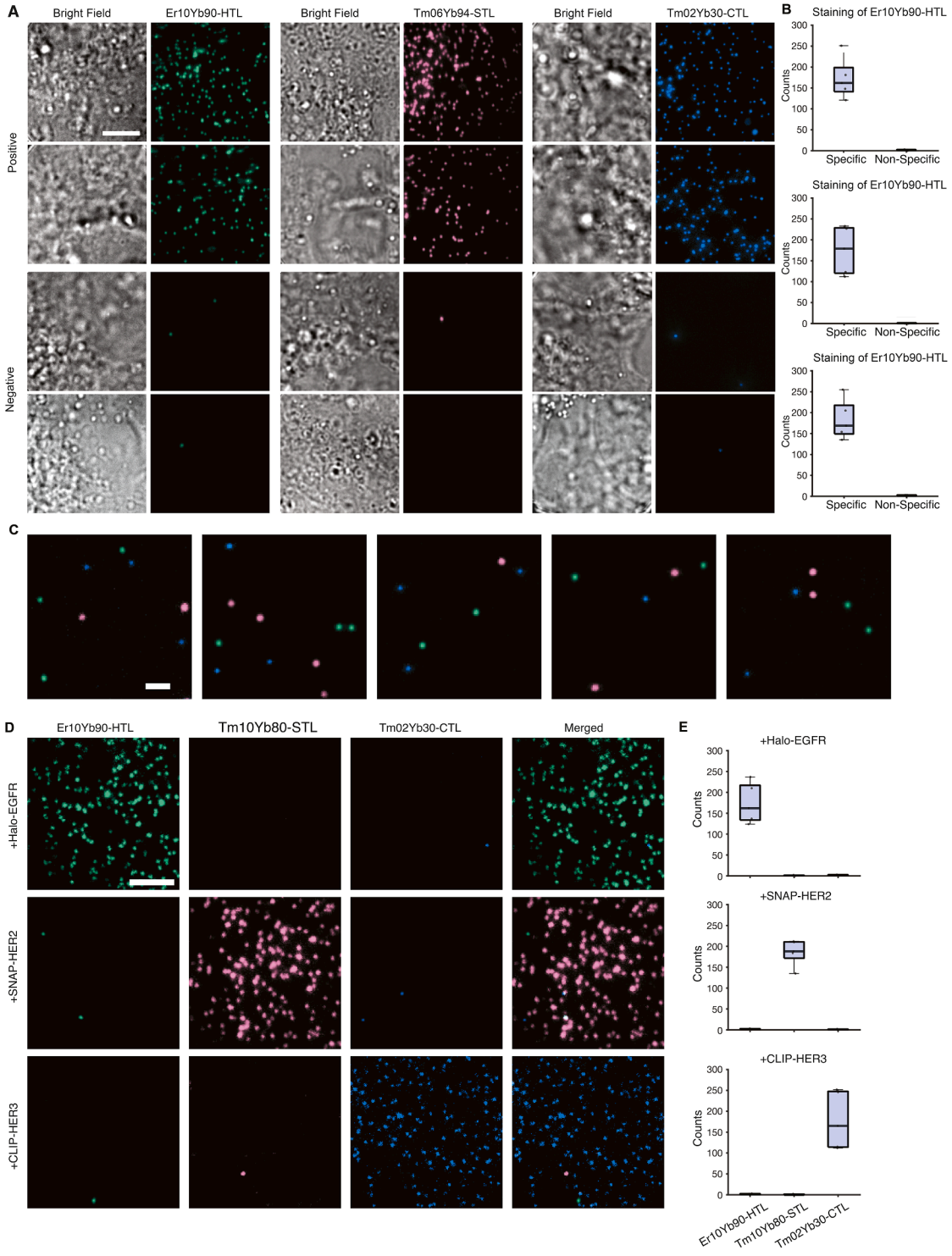

Figure S2. UCNP labeling efficiency and orthogonality, related to Figure 2

(A) Demonstration of specific versus nonspecific binding of ligand-conjugated UCNP on live cells. Representative bright-field images of the cell and corresponding UCNP images were taken at the bottom membrane. In the positive panels, wild-type U2OS cells were transfected with Halo-EGFR-WT for testing Er10Yb90-HTL, SNAP-HER2-WT for testing Tm06Yb94-STL, and CLIP-HER3-WT for testing Tm02Yb30-CTL. In the negative panels, wild-type U2OS cells were used for all three functionalized UCNPs. Scale bars, 5 μm.

(B) Quantification of specific staining versus non-specific staining of all three functionalized UCNPs.

(legend continued on next page)

(C) Three probes (Er10Yb90-HTL, Tm10Yb80-STL, and Tm02Yb30-CTL) were mixed at equal concentration (~100 nM), diluted, and imaged on a coverslip to show orthogonality of the three ligand-conjugated UCNPs in the mixture and in the live-cell labeling. Five different representative fields of view showed no overlap of probes. Scale bars, 2 μm.

(D) Halo-EGFR, SNAP-HER2, or CLIP-HER3 expressing U2OS cells were labeled by three-probe mixture (Er10Yb90-HTL, Tm10Yb80-STL, and Tm02Yb30-CTL, each at 1 nM). Scale bars, 5 μm.

(E) Quantification of specific staining versus nonspecific staining.

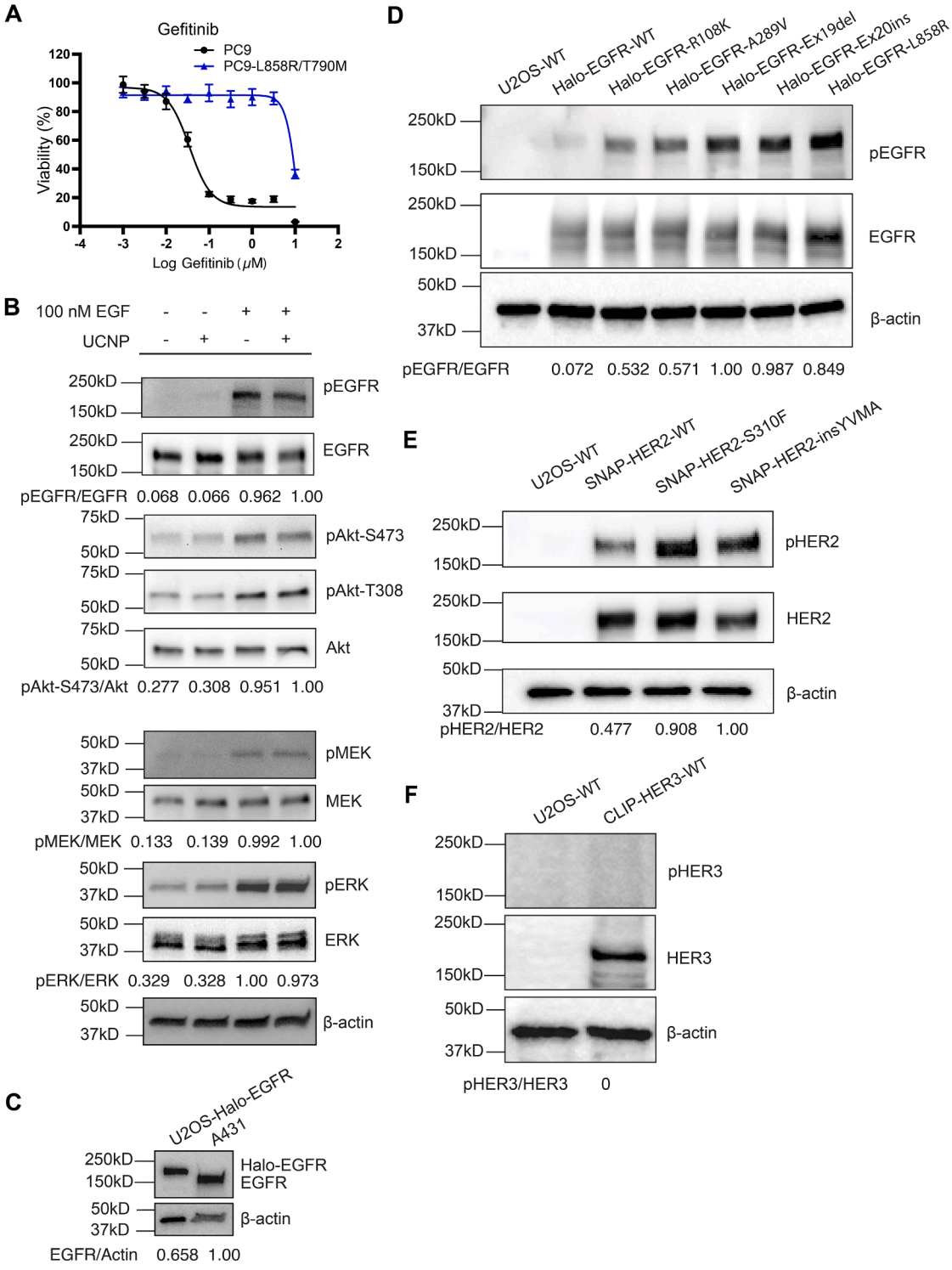

Figure S3. Validation of expression and function of receptors N-terminally fused with SLPs, related to Figures 2, 3, 4, and 5

(A) Validation of the resistance of PC9 cells expressing EGFR-L858R/T790M to gefitinib.

(B) The phosphorylation of EGFR, Akt-S473, Akt-T308, MEK, and ERK was assessed by western blot (WB) with U2OS-Halo-EGFR stable cells labeled or unlabeled with UCNP-HTL for 10 min. 100 nM EGF was added for 10 min for the EGF stimulation condition. The results indicate that UCNP-HTL did not exhibit agonistic or antagonistic effects on EGFR activation. Images are representative of three independent replicates.

(legend continued on next page)

(C) The expression of Halo-EGFR in the U2OS stable cell line and EGFR in the A431 cell line was probed by WB. The images shown are representative of three independent experiments.
(D) Western blot analysis revealed that the ligand-independent phosphorylation of EGFR-R108K, A289V, Ex19del, Ex20ins, and L858R was higher than that of WT EGFR in the transiently transfected U2OS cells. ACTIN was used as a loading control. The images shown are representative of three independent experiments.
(E) Ligand-independent phosphorylation and total expression level of transiently transfected SNAP-HER2-WT and mutants in U2OS cells. ACTIN was used as a loading control. The images shown are representative of three independent experiments.
(F) Phosphorylation and total expression level of transiently transfected CLIP-HER3-WT in U2OS cells. ACTIN was used as a loading control. The images shown are representative of three independent experiments.

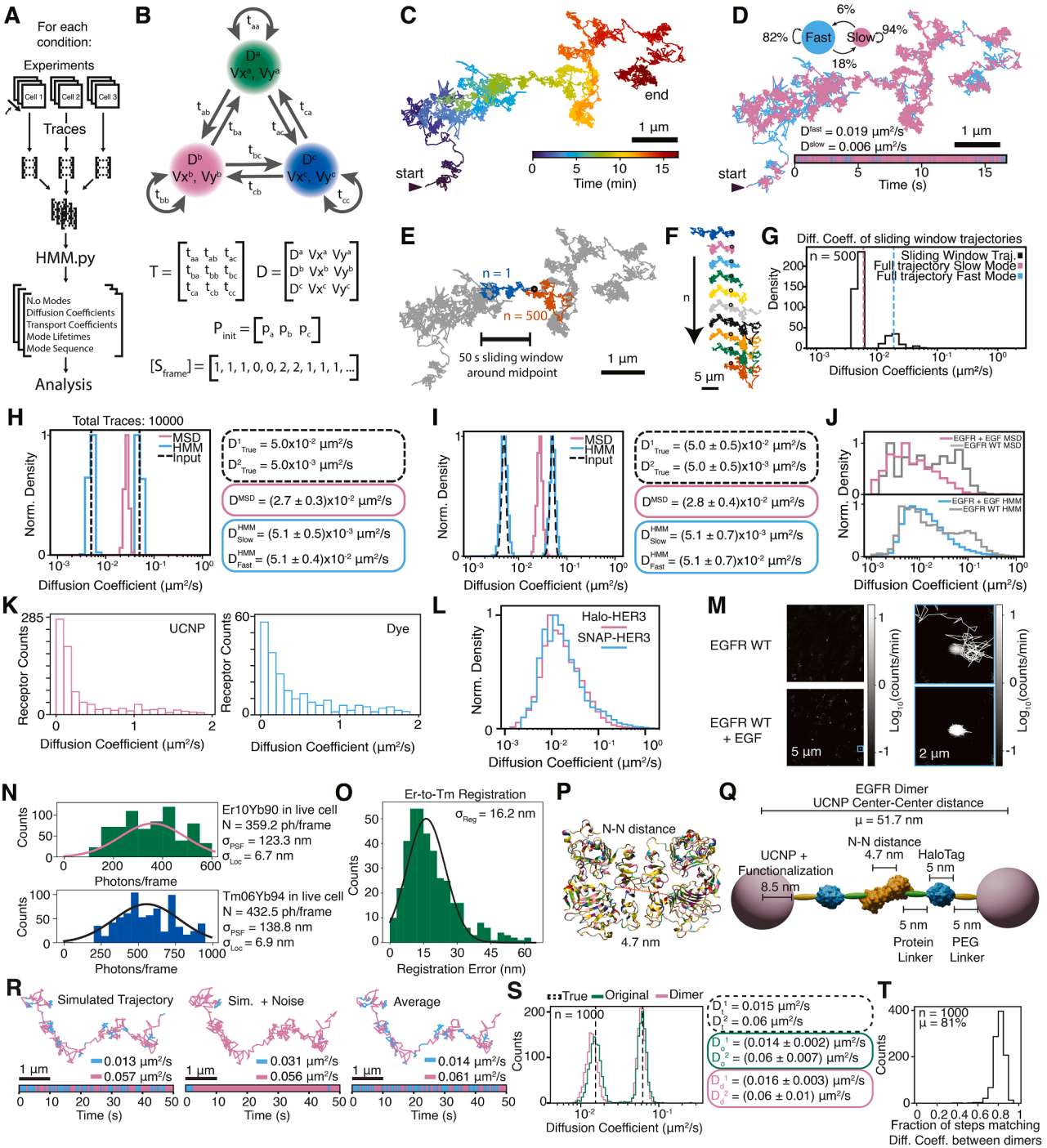

Figure S4. UCNP-SPT reveals rich dynamic information of receptor movement and diffusion, related to Figures 3, 4, and 5

(A) HMM analysis pipeline for obtaining diffusion coefficients for each condition. For each video of a given experimental condition (e.g., EGFR WT), we obtain the trajectories using SLIMfast2, a custom MATLAB script that performs 2D Gaussian fitting with the multiple-targeting tracing method.[121] The trajectories are bundled together into one array, and that is submitted to the custom Python code HMM.py. The HMM algorithm has been modified from Monnier et al.[75] to be able to run efficiently in a parallelized GPU architecture. It was necessary to do so, given the unprecedented length of the trajectories, in addition to the large volume of trajectories per condition. Each run lasted for 4–6 days on a V100 Nvidia GPU at Lincoln Lab's HPC Supercloud computer. The HMM results yield many parameters for each trajectory, which were then used for statistical analysis: the number of diffusion modes, the diffusion coefficients of each mode, the transport velocities of each mode (if any), the lifetimes for each mode in the form of mode transition probabilities, and the most likely sequence of modes for the trace.

(B) Scheme of the assumed hidden Markov model, exemplified by 3 diffusional modes. At each time point (100 ms, the exposure time of each video), the receptor is assumed to be in mode A, B, or C. The next step in the trace is determined by the mode parameters. The next mode is also determined stochastically based on

(legend continued on next page)

the transition probabilities between modes. We limit our analysis to three modes to avoid overfitting through excess of parameters. Our results show that most traces remain in one or two diffusional modes.
(C) One example trajectory of EGFR WT analyzed using the HMM algorithm.
(D) Trajectory of (C) colored by diffusion state. The trajectory contains 2 diffusional modes, one with a slower diffusion coefficient ($6 \times 10^{-3}\ \mu m^2/s$) and one with a faster diffusion coefficient ($1.9 \times 10^{-2}\ \mu m^2/s$). The lifetime of the fast mode is about 0.6 s (on average, the trajectory stays in the fast mode for 6 frames), and the lifetime for the slow mode is about 1.7 s (on average, the trajectory stays in the fast mode for 17 frames). The horizontal bar shows the state at every time point over the 15+ min of the recording.
(E) Diagram illustrating the sliding window centered around the midpoint of the trajectory shown in (C). To calculate how truncation of a trajectory affected the underlying diffusion coefficient, we created 500 subsets of the trajectory in (C), each composed of 500 frames (50 s). Each trajectory was shifted from the previous by one frame, and all included the midpoint. The first trajectory (blue) and the last (orange) are shown overlaid with the total trajectory (gray). The first and the last trajectories only share the midpoint in common (black circle).
(F) Diagram showing how the sliding window captures different parts of the total trajectory as the frame shift "n" increases. The midpoint is shown by the black circle.
(G) Diffusion coefficient distribution of the frame-shifted sub-trajectories. Only one of the trajectories did not rescue a 2-mode distribution like that of the total trajectory. The final distribution of diffusion coefficients agrees with the coefficients found from analyzing the entire trajectory (dashed vertical lines). Furthermore, the assigned diffusion coefficient or the midpoint was always found to be similar, within the error of the distribution. It was also always the slower of the two coefficients Found.
(H) Histogram of the comparison between calculated diffusion coefficients obtained from mean-square displacement (MSD) analysis and from hidden Markov model (HMM) analysis. The ground truth was a two-state model with diffusion coefficients set to 0.05 and 0.005 $\mu m^2/s$, with lifetimes of 0.3 s. 10,000 trajectories of 500 frames (50 s) were simulated. While the MSD obtained only one intermediate value, HMM correctly yielded the two diffusion coefficients. In all cases, the standard deviation over the mean was about 10%. However, MSD produced a nonsensical value between the ground truth coefficients, while HMM accurately predicted the correct coefficients. MSD diffusion coefficients were obtained by utilizing a window of 6 frames and fitting the first 5 frames of the resulting MSD plot to obtain the final diffusion coefficient. An increase in window frames only increased the spread of the resulting distribution, as well as poorer fit qualities. Likewise, for an increase in the fitting frame number.
(I) Histogram of results for 10,000 trajectories, simulated with a spread of diffusion coefficients around 0.05 and 0.005 $\mu m^2/s$ with a standard deviation of 10%. While the MSD still obtained only one intermediate value, HMM correctly yielded the two diffusion coefficient distributions. The standard deviation of the recovered diffusion coefficient distribution is exactly what is obtained if we add in quadrature the standard deviation recovered by the HMM analysis from the simulation in (H) and the ground truth 10% standard deviation from the simulation in (I).
(J) Comparison of HMM and MSD results for the EGFR WT (+/−) EGF condition. HMM analysis gives more accurate coefficients without bias: the MSD analysis does not pick up on the faster-moving tail of EGFR and shows overall slower values. MSD also does not pick out the two coefficient peaks that show up in the HMM result for EGFR, although the slowdown trend is still captured.
(K) Diffusion coefficients of Halo-EGFR labeled with UCNP-HTL or Halo-JF646.
(L) Comparison of diffusion coefficients for Halo-HER3 and SNAP-HER3.
(M) Heatmaps of trajectory localizations, in units of trajectory counts normalized by recording time. The hotspots in white indicate areas with many localizations, either due to large visitation rates by different receptors or due to slow diffusion by one or more receptors. The study of the diffusivity hotspots has been shown before to be a powerful tool for the inference of cellular structures,[130,131] and thus our future research directions include correlating dimerization frequency and the membrane structure inferred by the existence of the diffusivity hotspots. Top left: Diffusion heatmap of EGFR WT trajectories. Bottom left: Diffusion heatmap of EGFR WT after stimulation with 100 nM EGF. Right: Insets in blue from the condition with EGF stimulation overlaid with individual trajectories. The top example trajectory diffuses around one central hotspot, while the bottom one is confined to it.
(N) Brightness distribution per frame for the Er- and Tm-doped UCNPs used in 2-color labeling and dimer identification. To calculate localization precision, we divide the point-spread-function by the square root of the number of photons per frame. We calculate the average localization error of each particle to be ~6.8 nm.
(O) Registration error distribution for the NIR channel (for imaging Tm06Yb94) to the red channel (for imaging Er10Yb90). The mean registration error is 16.2 nm.
(P) PDB structure (PDB: 1IVO) of the EGFR dimer,[16] colored by residue. The red dashed line connects the two N-termini and measures 4.7 nm.
(Q) Scheme showing an EGFR dimer labeled by two UCNPs. At the center, we have the PDB structure of the EGFR dimer. At their N-termini, we show the peptide linker to the HaloTag protein. Then, we show the PEG linker, at the end of which is connected the HaloTag Ligand. At the other end, we have the functionalized UCNP. Overall, the UCNP center-center distance is estimated to be 51.7 nm.
(R) To understand how to best apply our Bayesian HMM diffusion analysis on dimers, we simulated 1000 trajectories with 2 diffusion states. We then added Gaussian noise centered on the calculated separation between UCNPs in an EGFR dimer (51.7 nm), with a standard deviation equal to our final error (32 nm). HMM analysis on these two trajectories (original input and the noisy trajectory) yielded different diffusion coefficients and state sequences. However, when we averaged the two trajectories, we were able to recover both the coefficients and the correct mode assignment for each step. This result shows that for accurate recovery of dimer behavior, we should average the trajectories of each receptor while it is dimerized. Representing dimers found through single-particle tracking as the average trajectory of their components is commonly done in SPT literature,[44] and thus all dimer trajectories are shown as the average of the two monomers. (Left) Simulated trajectory and its diffusion mode as a function of time. (Middle) Simulated trajectory with Gaussian noise added, and the HMM-assigned diffusion modes as a function of time. (Right) Averaged trajectory of the original and noisy trajectories and the HMM-assigned diffusion modes as a function of time.
(S) Histograms showing the simulated diffusion coefficients (dashed lines), recovered coefficients from the simulated trajectory (green), and recovered coefficients from the average of the noisy and simulated trajectory (magenta).
(T) Histogram of the fraction of steps per trajectory that were assigned the same mode between the simulated trajectory and the averaged trajectory. In total, averaging the trajectory recovers the original diffusion modes over the trajectory with 81% fidelity.

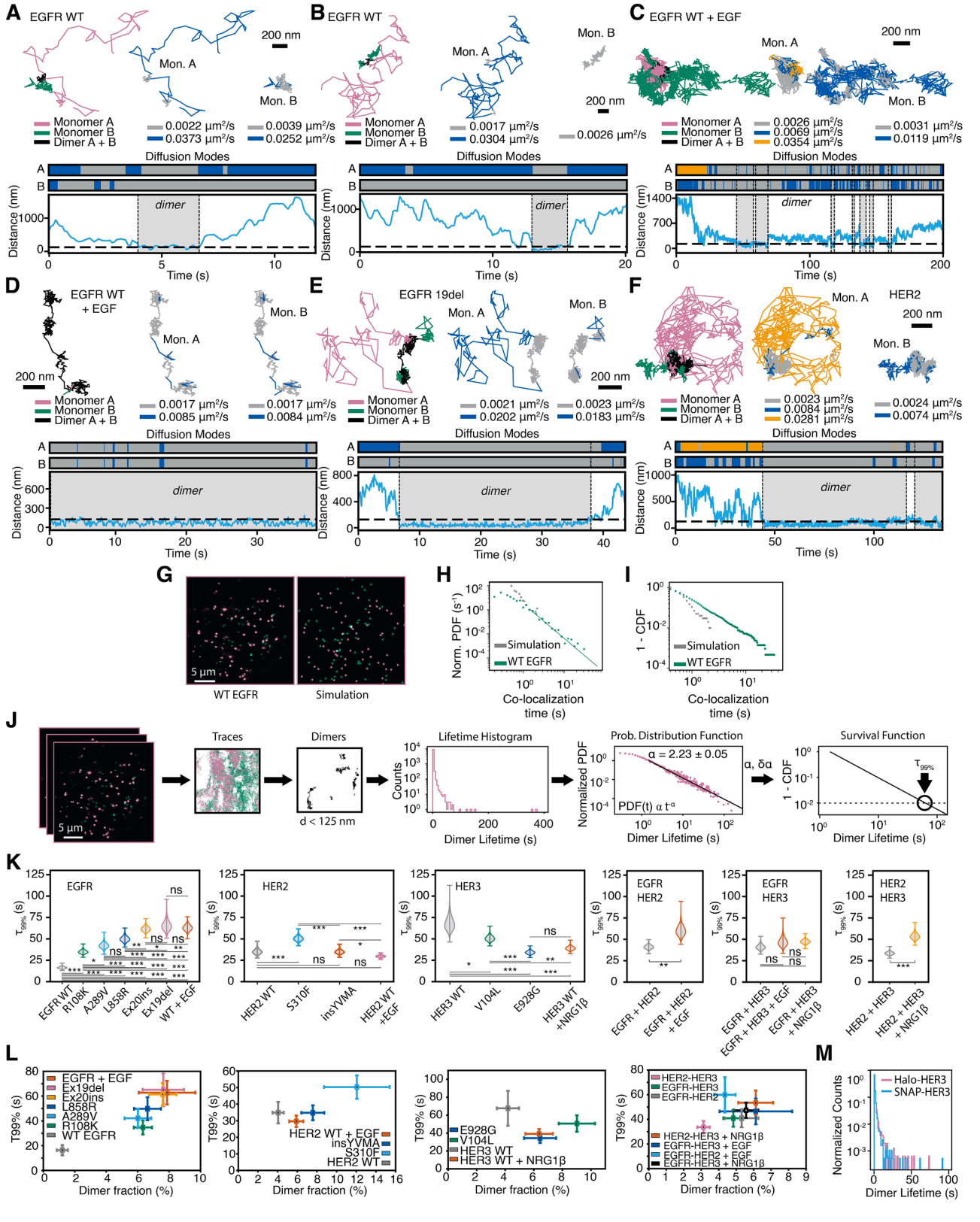

(legend on next page)

Figure S5. UCNP-SPT enables unprecedented details on receptor dimerization, revealing dimer lifetimes as a novel quantification of cellular signaling, related to Figures 3, 4, 5, and 6

(A–F) Diffusion mode analysis correlated with dimerization. They show dimers found through the dimer analysis code, and then subsequently run through the Bayesian HMM analysis for diffusion mode identification. The leftmost trajectory shows the dimer state for each monomer (A and B), with the black trajectory indicating the steps both are within the dimerization threshold of 125 nm of the other. For those steps, following the logic of (A), we average the measured positions of the two monomers within the dimer. The two rightmost trajectories show each monomer separately, with monomer A in the center and monomer B on the right, colored by diffusion mode. The bottom graph shows the diffusion mode (color-coded bars) and the distance between the two monomers as a function of time (distance plot). The horizontal dashed black line indicates the dimer threshold of 125 nm, and the times assigned to a dimer are highlighted in gray. Trajectories rarely skipped a few frames (<5 frames, or 0.5 s), and those gaps were interpolated linearly. Except for only a few frames, the diffusion coefficients of each receptor agree with one another when they are in the dimer state. Notably, we detect a 10-fold change in diffusion coefficient for one of the receptors when it becomes a dimer, shown in (F). (A) and (B) are dimers from the EGFR TW condition. (C) and (D) are dimers from the EGFR WT + 100 nM EGF condition. (E) Homodimer from the EGFR 19del condition. (F) Homodimer from the HER2 condition.

(G) Left: snapshot of experimental SPT video of WT EGFR. Right: a snapshot of simulated SPT video for 100 point-spread functions. Both colors label EGFR. Scale bars, 5 μm. To assess whether random encounters between diffusing receptors could bias the dimerization histograms, we generated simulated datasets resembling the experimental conditions (three videos, 1000 frames each, ~100 particles per video). The movements of the PSFs were simulated using diffusion coefficients sampled from the distribution of WT EGFR, and without any interactions between the PSFs. PSFs in two different color channels were simulated. These simulated videos were then processed through the same analysis pipeline used for the experimental data, and colocalization events were identified using the same distance thresholds. For this analysis, we relaxed the distance threshold for dimerization to 200 nm to get an upper bound on the maximum random "dimerization lifetime."

(H) PDF histograms of WT EGFR and the simulated random encounter. There were 101 colocalization events in the simulation, and all were shorter than 2 s. Only one of 101 events was longer than 1.4 s. The simulation data was not fit since the fitting method used for the WT EGFR and other conditions fits only datapoints above 1.5 s and would fail with the simulated data.

(I) Survival function (1−CDF) curve of the data in (T). This result ensures that the selected minimum time for the power law fit is an accurate selection of the cutoff differentiating random encountering from biological dimerization.

(J) Scheme illustrating the steps taken to quantify dimerization lifetimes. From the multicolor SPT videos, we obtain trajectories of individual receptors. Then, custom Python code is used to identify trajectories that remain within a set threshold distance (in all cases considered in this work, 175 nm). These are classified as dimers. Receptors dimerized before the recording is started are disregarded, likewise with dimers that do not dissociate until the end of the recording. The lifetimes can be plotted as a histogram; however, given the sparse nature of long dimer events, calculating the probability distribution function gives a better idea of the distribution behavior. We found that the dimer lifetime distributions for all receptors follow a power law, indicated by a straight line in a log-log plot. We fit the PDF data to the power law and obtain the power parameter α (with error quantification). For distributions where $\alpha$is larger than 2, the time at which 99% of dimers have dissociated is well defined analytically. We define this time as $\tau_{99\%}$, and we use it as a measure of dimer stability. The error on this quantity is also well defined as a function of the error on α.

(K) $\tau_{99\%}$ violin plots from n = 10,000 bootstrap fits on the full datasets, annotated with significance between $\tau_{99\%}$ of each condition in a series. Significance (p) was calculated through Z score evaluation. "ns": $p > 0.05$; "*": $p < 0.05$; "**": $p < 0.01$; "****": $p < 0.001$.

(L) $\tau_{99\%}$ versus apparent dimer fraction of each experimental condition. The apparent dimer fraction was calculated per cell video and then averaged among the recordings to yield the average dimer fraction, as well as the standard error. This is the apparent dimer fraction because it is calculated from the observed receptors, but not all receptors on the cell membrane are labeled. For EGFR and mutants, the dimer fraction increases with the dimer lifetime. For HER2 and mutants, the S310F mutant shows a larger dimer fraction and higher dimer lifetimes when compared with insYVMA. For HER3 and mutants, all mutants show more dimers, but they also show smaller dimerization lifetimes. This implies the mechanisms of oncogenic activities are different for HER3 mutants versus EGFR and HER2. EGFR-HER2 heterodimers show an increase in dimer lifetimes alongside a reduction in the number of dimers upon EGF stimulation. On the other hand, EGFR-HER3 heterodimers show an increase in both dimer lifetimes and fraction with the same stimulation. HER2-HER3 dimerization parameters show the largest increase of all heterodimer data upon stimulation of NRG1.

(M) Comparison of dimer lifetime for Halo-HER3 and SNAP-HER3.